NACA RM A57A02

NACA

RESEARCH MEMORANDUM

AN INVESTIGATION OF WING-BODY JUNCTURE INTERFERENCE EFFECTS AT TRANSONIC SPEEDS FOR SEVERAL SWEPT-WING AND BODY COMBINATIONS

By John B. McDevitt and Robert A. Taylor

Ames Aeronautical Laboratory
Moffett Field, Calif.

NATIONAL ADVISORY COMMITTEE
FOR AERONAUTICS

WASHINGTON
May 16, 1957
Declassified May 29, 1959

NATIONAL ADVISORY COMMITTEE FOR AERONAUTICS

RESEARCH MEMORANDUM

AN INVESTIGATION OF WING-BODY JUNCTURE INTERFERENCE EFFECTS AT TRANSONIC SPEEDS FOR SEVERAL SWEPT-WING AND BODY COMBINATIONS

By John B. McDevitt and Robert A. Taylor

SUMMARY

This report presents the results of an investigation of wing-body juncture interference effects at high subsonic and transonic speeds. Force characteristics and pressure measurements for various bodies in combination with sweptback wings of aspect ratios 3 and 6 were obtained through a Mach number range from 0.8 to 1.2. The bodies used consisted of basic Sears-Haack bodies of revolution, the basic bodies indented by area-rule concepts at design Mach numbers of 1.0 and 1.2, and the latter area-rule bodies reshaped without change in cross-sectional areas (by the superposition of slender-body multipoles) so that the flow along the wing-body juncture chords at high subsonic speeds more closely resembled that for the infinite oblique wing.

The various area-rule applications resulted in large reductions in the transonic wave drag. The reshaping of the $M = 1$ area-rule bodies by application of multipole theory did not result in further drag reductions. This result is believed to be due to the fact (as indicated by both theoretical and measured pressures) that the $M = 1$ area-rule applications for these particular wing-body combinations result in juncture pressure distributions at transonic speeds which are quite similar to the pressure distribution of the oblique wing in subcritical flow. However, the $M = 1.2$ supersonic area-rule application was found to give unfavorable juncture-chord pressure distributions. The desired corrections to the flow were large and could not be fully achieved by a realistic application of multipole theory. A partial adjustment of pressures was attempted which resulted in a slight reduction of wave drag near $M = 1$.

INTRODUCTION

The possibility of employing sweepback for reducing transonic effects followed from the early investigations by Gothert and R. T. Jones (refs. 1 to 3) of the linearized flow about swept wings (see also the work of Neumark, ref. 4). However, the full benefit indicated by simple-sweep theory at high subsonic speeds could not be obtained in practice, principally because the streamwise pressure distribution near the root of the swept wing differs from that for the infinite oblique wing in subsonic flow. (The full benefit of sweep is achieved if the wing isobars are everywhere parallel to the local sweep of the wing.)

The unfavorable pressure distribution near the root of the sweptback wing can be corrected either by altering the wing geometry near the root or by contouring the body in the vicinity of the wing-body junction. The possibility of obtaining favorable junction pressure distributions by shaping the sides of the body to conform to the general shape of a streamline on the yawed, infinite wing has been reported on in references 5 to 7. The design of wing-body junctions by the use of a quasi-cylindrical theory involving ring vortices in linearized subsonic flow was developed by Küchemann, references 8 and 9. (In the Küchemann method the pressure distribution at the wing-body juncture is assumed to be equal to that for the center line of the sweptback wing.) A more exact theory for determining the linearized, subsonic flow about wing-body combinations has been developed recently (ref. 10).

Although most of the early investigations of the swept-wing problem (refs. 5 to 9 and 11 to 14) suffered from the limited Mach number range made available by the conventional wind tunnel, significant reductions in drag were obtained at high subsonic speeds by the use of body contouring. Using rocket-powered models, Pepper (ref. 7) was able to conduct an investigation throughout the transonic speed range and found that large drag reductions could be obtained by indenting the body so as to approximate the streamline flow over the yawed, infinite wing.

Soon after the completion of the first transonic wind tunnel at the Langley Aeronautical Laboratory, the transonic area-rule concept for slender-wing-body combinations was discovered and verified by the experiments of Whitcomb (ref. 15). The extension of this concept to include supersonic design Mach numbers was made by R. T. Jones, reference 16 (see also ref. 17). Following the discovery of the area rule a re-examination of the swept-wing problem appeared desirable. An experimental investigation (ref. 18) indicated that both the area-rule concept and Küchemann's design method result in large drag reductions at transonic speeds for swept-wing and body combinations. Furthermore, it was found that the area-rule indentation for this particular swept wing resulted in junction pressures similar to those for the oblique wing in subsonic flow. Actually the body shapes were quite similar, the major difference being in the body

contouring downstream of the junction chord. Thus it appears that for swept wings, somewhat similar body contours result from applications of the area rule and from the method of Küchemann.

The possibility of combining Küchemann's concept of adjusting juncture pressure distributions and area-rule concepts motivated the investigation of the present report. The two concepts can be considered simultaneously by first prescribing the axial distribution of cross-sectional areas according to the area rule and then using slender-body multipoles (which alter the body shape without change in cross-sectional area) to adjust the pressure distribution at the wing-body juncture to conform to those for an infinite yawed wing. Several investigations somewhat similar to the investigation of the present report have been conducted recently. In references 19 to 21 the possibility of shaping the body of sweptback wing and body combinations so as to combine the curvature of the streamline over the oblique wing with the longitudinal area distribution obtained by area-rule concepts has been investigated for both nonlifting and lifting cases.

NOTATION

The primary symbols used in this report are defined as follows:

A wing aspect ratio

$A_o(x)$ strength of axial sources

$a_n(x), b_n(x)$ strength of axial multipole distributions according to slender-body theory

b wing span

C_D drag coefficient, $\frac{\text{drag}}{qS}$

C_L lift coefficient, $\frac{\text{lift}}{qS}$

C_m pitching-moment coefficient, $\frac{\text{pitching moment about } \bar{c}/4}{qS\bar{c}}$

C_P pressure coefficient, local pressure minus free-stream static pressure divided by q

c local wing chord

$\left.\begin{matrix}\bar{c},\\ \text{M.A.C.}\end{matrix}\right\}$ mean aerodynamic chord, $\dfrac{\int_0^{b/2} c^2\,dy}{\int_0^{b/2} c\,dy}$

c_j reference chord near wing-body junction (chord through the point of intersection of basic or area-rule bodies and wing leading edge)

c_R chord at wing center line

c_T chord at wing tip

l body length (distance from nose to theoretical point of closure)

M free-stream Mach number

M_{cr} critical Mach number

M_{des} design Mach number

q free-stream dynamic pressure, $\frac{1}{2}\rho U_\infty^2$

R body radius

r polar coordinate in y,z plane

S area of wing plan form

$\frac{t}{c}$ wing thickness-to-chord ratio

U_∞ free-stream velocity

u,v,w perturbation velocities normalized by division by the free-stream velocity

$v_{(r)}$ radial component of perturbation velocity in yz plane normalized by division by the free-stream velocity

x,y,z Cartesian coordinates

ξ,η,ζ Cartesian coordinates normalized by division by the juncture chord c_j

ξ_j Cartesian coordinate with origin at the leading edge of the reference chord c_j

α	angle of attack
β	$\sqrt{\lvert M^2-1 \rvert}$
θ	polar angle in y,z plane
λ	wing plan form taper ratio, $\frac{c_T}{c_R}$
ρ	free-stream density
φ	perturbation velocity potential
Λ	angle of sweep, positive when swept back
$(\bar{\ })$	variable of integration
$(\ )'$	first derivative with respect to the free-stream direction
$(\ )''$	second derivative with respect to the free-stream direction

Subscripts

a	reference or starting point
j	condition along wing-body junction
LE	wing leading edge
n	order of multipole
w	wing
2	axial quadripole

APPARATUS AND MODELS

Apparatus

The tests were conducted in the Ames 14-foot transonic wind tunnel which is equipped with a perforated test section permitting continuous operation from subsonic to low supersonic speeds.

The models were mounted on a sting support as shown in figures 1 and 2. The normal and chord forces and the pitching moment were measured by a strain-gage balance enclosed within the model. Multiple-tube mercury manometers, connected to pressure orifices in the model by flexible tubing, were photographed to provide records of the pressure distributions on the models.

Models

Plan-form details of the various models are presented in figure 3. For all the wing-body combinations the center lines of the bodies were located in the chord plane of the wing and all bodies were truncated to permit mounting on the sting. The body contour details in the vicinity of the wing are presented in figures 4 to 6.

The wing used for model series I (fig. 3(a)) had an aspect ratio of 6, a taper ratio of 0.4, and NACA 64A008 sections in the streamwise direction with the 40-percent-chord line swept back 40°. The wing used for model series II and III had an aspect ratio of 3, a taper ratio of 0.4, and NACA 64A006 sections perpendicular to the 25-percent-chord line. The wing leading edge was swept back 45°.

Models I-A and II-A.- The bodies used for models I-A and II-A were bodies of revolution shaped in accordance with the Sears-Haack formula

$$\frac{r}{r_{max}} = \left[1-\left(1-\frac{x}{l/2}\right)^2\right]^{3/4}$$

The fineness ratio (based on the theoretical length of the body to closure and the maximum body diameter) was 11 for body I-A and 12.5 for body II-A.

Models I-B, II-B, and III-B.- The bodies of revolution used for models I-B and II-B were indented according to the $M = 1.0$ area rule such that the wing-body combinations had axial distributions of cross-sectional areas equivalent to the basic Sears-Haack bodies of models I-A and II-A, respectively. (A convenient method for calculating the indented body radii is presented in Appendix A of this report.)

The body of revolution used for model III-B was indented according to the supersonic slender-body area rule for a design Mach number of 1.2 with the area distribution of the Sears-Haack body of model II-A used as the desired optimum. (See ref. 16 or 22 for a discussion of the supersonic slender-body area rule.)

Models I-C, II-C, and III-C.- The body shapes for models I-C, II-C, and III-C were obtained by altering, without change in cross-sectional areas, the shapes of bodies I-B, II-B, and III-B, respectively, by applications of slender-body quadripole theory so as to adjust the flow along the junction chords to agree more closely with that for the oblique wings in subsonic flow (design Mach number of 0.9). The theoretical method used for obtaining the body shapes of models I-C, II-C, and III-C is described in detail in Appendix B of this report.

The calculated pressure distributions (using the wing-body theory of ref. 10) along the junction chords of models I-B, II-B, and III-B are compared with those of the oblique wing in part (a) of figures 7 to 9. The desired adjustment of juncture pressures and the actual corrections considered in the design of bodies I-C, II-C, and III-C are presented in part (b) of figures 7 to 9. The computed radii for model II-C near $\theta = 90^\circ$ and 270° (top and bottom of fuselage) for body stations 54 to 68 (see fig. 5(b)) were arbitrarily increased a moderate amount to the values shown in figure 5(b), $\theta = 90^\circ$, so as to permit installation of the balance mechanism. Because of the large differences in pressures indicated in figure 9(a), the full correction of the junction flow by the use of quadripole theory was not possible for model III-C. However, a partial correction was arbitrarily chosen as shown in figure 9.

In the design of these bodies it was found that the starting, or reference, point for the front and rear superposition of the axial quadripoles must be chosen with care in order to keep the resulting body distortions of a realistic magnitude. The various starting points are indicated in part (b) of figures 7 to 9. Arbitrary fairings consistent with slender-body concepts were used to terminate the quadripole distortions of the body shapes fore and aft of the junction chord.

TESTS AND PROCEDURE

The models were tested through a Mach number range from 0.8 to 1.2. The Reynolds number (based on the wing mean aerodynamic chord and the average temperature of the air) was approximately 4×10^6 for model series I and approximately 7×10^6 for model series II and III (fig. 10).

Tunnel-boundary-interference corrections were not applied to the data. These effects at subsonic speeds are considered to be negligible due to the perforated test section. For models of the size employed in the present investigation, the influence of the reflected waves on model characteristics is known to be small and confined to the Mach number range from 1.00 to about 1.15.

The drag data have been corrected for an interaction in the balance mechanism of normal force on chord force and have been adjusted to represent free-stream static pressure at the model base.

FORCE STUDY RESULTS

The aerodynamic characteristics of the various wing-body combinations of model series I (swept wing of aspect ratio 6) and model series II and III (swept wing of aspect ratio 3) are, for convenience, presented separately. Some results of body-alone tests conclude the presentation of force data.

Model Series I

The drag, lift, and pitching-moment data are shown in figure 11 for the three configurations utilizing the swept wing of aspect ratio 6. (See figs. 3(a) and 4 for design details of the various models.) Cross plots, which summarize the more important force characteristics, are presented in figures 12 to 14.

Drag.- The variation of drag coefficient with Mach number at zero lift and at $C_L = 0.2$ is shown in figure 12. The transonic drag characteristics of the two models having smooth axial distributions of cross-sectional areas in accordance with the $M = 1$ area rule (models I-B and I-C) demonstrate the fundamental importance of the area-rule concept. Near $M = 1$ the area-rule applications resulted in reductions of wave drag, when compared with the basic model I-A, of approximately 70 percent. With increasing supersonic Mach numbers, however, the favorable interference effects of the area-rule indentations decrease and eventually disappear near $M = 1.2$.

The application of multipole theory in the design of model I-C (which altered the body cross-sectional shapes without change in the axial distribution of cross-sectional areas required by the area rule) to improve the flow near the wing-body juncture at high subsonic speeds did not appreciably affect the wave drag at transonic speeds. This result is believed to be due to the fact that the $M = 1$ area-rule application in this particular case results in wing-body-juncture pressures at transonic speeds which are quite similar to the pressure distribution of the oblique wing in subsonic flow.

The variation of maximum lift-drag ratio with Mach number is shown in figure 13. Considerably higher values of maximum lift-drag ratios were obtained at high subsonic and transonic speeds as a result of the application of the area-rule concept.

Lift.- The variation of lift-curve slope (evaluated at zero lift) with Mach number is shown in figure 14. The two area-rule configurations (models I-B and I-C) had, within the accuracy of the experimental data, essentially the same values of lift-curve slope throughout the Mach number

range. In general, the application of the area-rule concept resulted in higher values of lift-curve slope and in a somewhat smoother variation of lift-curve slope with Mach number at transonic speeds. This result is a direct consequence of the reduced shock losses that invariably accompany area-rule modifications for improving the axial distribution of cross-sectional areas.

Model Series II and III

The drag, lift, and pitching-moment data are shown in figures 15 and 16 for the five configurations employing the swept wing of aspect ratio 3. (See figs. 3(b), 5, and 6 for design details.) Cross plots, which summarize the more important force characteristics of these models, are presented in figures 17 to 19.

Drag.- The variation with Mach number of drag coefficient at zero lift and at $C_L = 0.2$ is shown in figure 17(a) for the basic configuration, model II-A, and for the two configurations, models II-B and II-C, having cross-sectional area distributions in accordance with the $M = 1$ area rule. The use of the area rule resulted in large reductions of drag throughout the transonic speed range.

The application of a suitable axial distribution of multipoles in conjunction with the $M = 1$ area rule so as to improve the flow along the wing-body juncture did not appreciably affect the drag of model II-C. As in the previous case for model I-C, this result is believed to be due to the fact that the application of the $M = 1$ area rule for this particular wing-body combination results in favorable juncture pressures which are difficult to improve.

In figure 17(b) measured drag characteristics of model II-A are repeated with the results for models III-B and III-C, which had area distributions according to the supersonic slender-body area rule for a design Mach number of $M = 1.2$. When compared with the previous drag results for the $M = 1$ area-rule designs of model series II, the $M = 1.2$ area rule is found to provide the expected greater wave-drag reductions near the design Mach number but is, approximately, only one half as effective near sonic Mach number. Theoretical calculations at $M = 0.9$, as well as measured juncture pressures, indicate that the $M = 1.2$ area-rule model (model III-B) has undesirable flow conditions along the junction chord at transonic speeds. The desired correction of the juncture flow was too large to be achieved by a realistic application of multipole theory. However, a partial adjustment of juncture pressures was attempted by the design of model III-C which resulted in a slight reduction of drag near $M = 1$. The variations of maximum lift-drag ratios with Mach number are shown in figure 18.

Lift.- The variations of lift-curve slope (evaluated at zero lift) with Mach number are shown in figure 19. In general, the various area-rule modifications resulted in higher values of lift-curve slope throughout the transonic speed range. By inspection of the drag and lift variations shown in figures 17 and 19, it is apparent that increases in lift-curve slope are directly connected with the relative effectiveness of the various area-rule modifications in reducing the transonic wave drag.

Body-Alone Tests

The variations of zero-lift drag coefficient with Mach number are presented in figure 20 for the various bodies used in this experimental investigation. The drag coefficients for body series I and II are based on the respective wing areas of model series I and II.

Bodies I-A and II-A are Sears-Haack bodies of revolution having fineness ratios of 11 and 12.5, respectively. Bodies I-B and I-C have identical cross-sectional areas with body I-C distorted by an application of quadripoles. Bodies II-B and II-C have identical cross-sectional areas with body II-C distorted by multipoles; bodies III-B and III-C can be described similarly. With the above description of the bodies in mind it is apparent that the drag variations shown in figure 20 indicate that the wave drag depends primarily on the axial distribution of cross-sectional areas. It can also be shown by theoretical considerations, using slender-body concepts, that the superposition of axial multipoles does not contribute to the wave drag (ref. 23), provided that the distribution function for the multipole strength, $a_n(x)$, terminates with zero first and second derivatives.

PRESSURE STUDY RESULTS

Surface pressure distributions for the various wing-body combinations were measured at zero lift. The experimental results are, for convenience, presented separately for model series I (swept wing of aspect ratio 6) and model series II and II (swept wing of aspect ratio 3).

Model Series I

The measured flow over the wing surface at various Mach numbers is illustrated by the isobar patterns presented in figure 21. The locations of the isobars were determined from the faired chordwise pressure data

obtained at nine lateral stations along the wing semispan. The measured pressure distributions along the body surfaces are presented in figure 22 for two body azmuthal locations,[1] $\theta = 0^{\circ}$ and $\theta = 90^{\circ}$.

Wing isobars.- The isobars shown in figure 21 demonstrate that the pressure field of the wing is decisively influenced at near-sonic speeds by the adjacent body shape. The unfavorable distortion of the wing pressure field near the basic body of model I-A is evident throughout the Mach number range. The $M = 1$ area-rule modification of model I-B corrected the unfavorable pressure field near the wing-body juncture in a very satisfactory manner (that is, the flow is in close agreement with that for the oblique wing). In particular, it should be noted that the streamwise location of the point of minimum pressure (indicated by the dashed lines of fig. 21) was shifted to a forward location at the root chord. The quadripole distortion used in the design of model I-C did not significantly alter the isobar patterns.

Body pressure distributions.- The importance of the body shape is again evident from the pressure distributions presented in figure 22. It is apparent that the favorable pressure distributions resulting from the area-rule modification of model I-B would be difficult to improve in order to achieve a further reduction in wave drag near $M = 1$.

Comparison of calculated and measured juncture pressures.- The theoretical and experimental pressure distributions near the wing-body junctions of model series I at zero lift are shown in figure 23 for Mach numbers of 0.85 and 0.90. The theoretical results were obtained by the use of the linearized flow theory for wing-body combinations described in reference 10.

The measured pressures at the innermost row of wing orifices ($y = 0.139\ b/2$) are also included in figure 23 since it was felt that a comparison of theory and experiment at the wing-body junction would suffer somewhat from boundary-layer effects in the corners of the wing-body juncture. In general, the theory and experiment are in reasonable agreement.

Model Series II and III

The measured pressure distributions at various Mach numbers for the models of series II and III at zero lift are presented in figures 24 to 29.

[1]At the wing-body juncture the pressure orifices along the sides of the bodies were located as close as possible to the upper surface of the wing. The designation $\theta = 0^{\circ}$ for the side row of orifices is used here for convenience, although, at the wing-body juncture, the orifice locations differed slightly from $\theta = 0^{\circ}$ because of the finite thickness of the wing.

Wing isobars for models II-A, II-B, and II-C.- The wing pressure distributions for models II-A, II-B, and II-C are indicated by the isobar patterns shown in figure 24. The unfavorable pressure field near the wing-body juncture of model II-A is evident throughout the Mach number range. The $M = 1$ area-rule modification of model II-B reduced the general level of the disturbance field over the entire wing for Mach numbers up to 1.10 and improved the flow near the juncture throughout the Mach number range.

Body pressure distributions for models II-A, II-B, and II-C.- The measured body pressure distributions for models II-A, II-B, and II-C are presented in figure 25. The $M = 1$ area-rule modification resulted in large changes in the body pressures which would be, as for the previous case of model I-B, difficult to improve upon in order to achieve further drag reductions near $M = 1$.

Comparison of calculated and measured juncture pressures for models II-A, II-B, and II-C.- The theoretical and experimental pressure distributions near the wing-body junctions of models II-A, II-B, and II-C at zero lift are presented in figure 26 for Mach numbers of 0.85 and 0.90. In general, the agreement between theory and experiment is good for models II-A and II-B.

Wing isobars for models III-B and III-C.- Wing isobars for models III-B and III-C are presented in figure 27. For the $M = 1.2$ area-rule-indented model III-B a local region of positive pressure coefficients occurs near the mid-chord of the wing-body juncture where the indented body radius is a minimum (see fig. 6(a)). As stated previously, the body used in model III-C was the result of an attempt to correct partially the junction flow at $M = 0.90$ by an application of quadripole theory.

Body pressure distributions for models III-B and III-C.- The measured body pressure distributions for models III-B and III-C at zero lift are presented in figure 28. Whereas the previous applications of the $M = 1$ area rule resulted in very satisfactory pressure distributions at the junction chords, it is evident from the pressure distributions for model III-B shown in figure 28 that the $M = 1.2$ area rule is unsatisfactory in this respect. The partial application of quadripole theory used in the design of model III-C improved considerably the pressure distribution along the junction chord. However, the flow along the top portion of the body surface was adversely affected by the quadripole distortion.

Comparison of calculated and measured junction pressures for models III-B and III-C.- The theoretical and experimental pressure distributions near the wing-body junctions of models III-B and III-C at zero lift are presented in figure 29 for Mach numbers of 0.85 and 0.90. The agreement between theory and experiment is good for model III-B but not so good for model III-C where the theoretical pressure coefficient contained large contributions from the quadripole distortions of this particular body shape.

Body-Alone Tests

The measured surface pressures for the basic bodies (Sears-Haack bodies of revolution having fineness ratios of 11 and 12.5) tested alone (wings removed) are presented in figures 30 and 31. The pressure distributions for the two bodies indented by applications of the M = 1 area rule are presented in figures 32 and 33. The pressure distributions for the body indented by the M = 1.2 slender-body area rule are presented in figure 34.

It is interesting to note that, for a given indented body shape, the streamwise pressure distribution does not change much throughout the Mach number range tested.

CONCLUDING REMARKS

The theoretical calculations at high subsonic Mach numbers as well as the experimental measurements at transonic speeds indicate that the M = 1 area-rule designs for sweptback wings result in wing-body-juncture pressures quite similar to the streamwise pressure distribution of the oblique wing in subcritical flow. As a result it can be expected that, for the particular case of the sweptback wing, the area rule will give results similar to those obtained by Küchemann's method and hence increase the critical Mach number as well as provide reductions in transonic wave drag.

In the present experimental investigation it was found that the quadripole distortions of the body shapes had comparatively little effect on the transonic wave drag when compared with the large effects resulting from changes in body cross-sectional areas (which is equivalent to specifying changes in the axial distribution of sources according to linearized or slender-body theory). It also appears from this investigation that significant improvements in M = 1 area-rule applications for transonic speeds are improbable for swept wings having at least a moderate amount of sweep but that further work is needed to improve juncture pressures for wing-body combinations designed by applications of supersonic area rules. In recent work by Lomax (ref. 24) it was shown that the supersonic extension of Whitcomb's area rule is an approximation for the correct rule of linearized theory which requires knowledge of model surface pressure distributions. Some indication of the success of a particular supersonic area-rule application at transonic speeds may be obtained by an inspection of the juncture pressure distribution at high subsonic speeds.

It is probable that a more exact understanding of the sonic and supersonic flows about wing-body combinations must be achieved before methods for obtaining optimum body shapes can be fully developed.

Attention should also be directed toward the more general problem of determining wing geometry such that the wave-drag reductions to be obtained shall be as complete as possible.

Ames Aeronautical Laboratory
National Advisory Committee for Aeronautics
Moffett Field, Calif., Jan. 2, 1957

APPENDIX A

BODY-INDENTATION FORMULAS FOR SWEPT-WING AND BODY COMBINATIONS INDENTED ACCORDING TO THE M = 1 AREA RULE

Formulas for obtaining the body shape of configurations indented according to the M = 1 area rule are easily obtained in the case of the swept wing if the wing has straight leading and trailing edges and tip chords parallel to the body axis. The area-rule concept suggests that the axial distribution of cross-sectional area for the wing-body combination be optimized, that is, made equivalent to that for a smooth body having low wave drag. The usual procedure is to remove from the smooth body volume the exposed volume of both wing panels such that the cross-sectional areas in planes normal to the body axis for the indented configuration are equal to the cross-sectional areas of the smooth body. A convenient method for determining the indented radii follows.

WINGS OF CONSTANT THICKNESS TO CHORD RATIO

Consider the wing-body combination shown in sketch (a) where, for convenience, all dimensions have been normalized by division by the junction chord c_j. If the integral representation for the wing cross-sectional area in the plane normal to the body axis is replaced by an equivalent integration performed in the streamwise direction, then the indented body radii, R_I, can be obtained by use of the following equation:

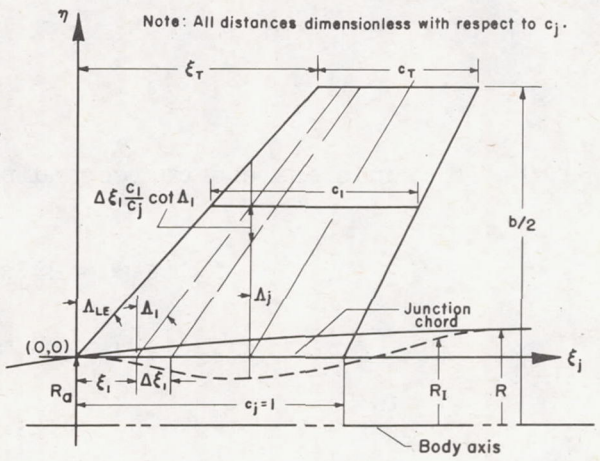

Sketch (a)

$$R_I^2(\xi_j) = R^2(\xi_j) - \frac{2}{\pi}\int_0^{\xi_j + \frac{R_a - R_I}{\cot \Lambda_1}} \cot \Lambda_1 c_1^2 2Z_1 d\xi_1 \qquad (A1)$$

where $2Z_1$ is the wing thickness measured along the junction chord and the local chord c_1 is given by

$$\left.\begin{aligned} c_1 &= 1-K(\xi_j-\xi_1)\cot\Lambda_1 \\ K &= \frac{\partial c_1}{\partial \eta} = \frac{1-c_T}{(b/2)-R_a} \end{aligned}\right\} \tag{A2}$$

For all practical cases, equation (A1) can be approximated by the following relationship

$$\frac{\pi}{2}\left(R^2-R_I^2\right) \approx F(\xi_j)+\frac{R_a-R_I}{\cot\Lambda_j}F'(\xi_j) \tag{A3}$$

where

$$F(\xi_j) = \int_0^{\xi_j} \cot\Lambda_1 c_1^2 2Z_1 d\xi_1$$

$$= f_1-2K\xi_j f_2+K^2\xi_j^2 f_3+2Kf_4-2K^2\xi_j f_5+K^2 f_6 \tag{A4}$$

$$F'(\xi_j) = f_1'(\xi_j) \tag{A5}$$

and the f functions and corresponding first derivatives are given by

$$\left.\begin{aligned} f_1'(\xi_1) &= 2Z_1\cot\Lambda_1 \\ f_2'(\xi_1) &= 2Z_1\cot^2\Lambda_1 \\ f_3'(\xi_1) &= 2Z_1\cot^3\Lambda_1 \\ f_4'(\xi_1) &= 2Z_1\xi_1\cot^2\Lambda_1 \\ f_5'(\xi_1) &= 2Z_1\xi_1\cot^3\Lambda_1 \\ f_6'(\xi_1) &= 2Z_1\xi_1^2\cot^3\Lambda_1 \end{aligned}\right\} \tag{A6}$$

$$\left.\begin{aligned} f_1(\xi_j) &= \int_0^{\xi_j} f_1' d\xi_1 \\ &\cdots\cdots\cdots \\ f_6(\xi_j) &= \int_0^{\xi_j} f_6' d\xi_1 \end{aligned}\right\} \tag{A7}$$

The evaluation of the integrals of equation (A7) usually requires numerical or graphical techniques. A convenient formula for obtaining the variation of Λ_1 with ξ_1 is

$$\tan \Lambda_1 = \tan \Lambda_{LE} - K\xi_1 \tag{A8}$$

The f_i and f'_i functions for the wing used in model series II of this report are shown in figure 35.

Solving equation (A3) for R_I gives the desired body-indentation formula

$$\left.\begin{aligned} R_I(\xi_j) = \frac{f_1'(\xi_j)}{\pi \cot \Lambda_j} + \left\{ \left[\frac{f_1'(\xi_j)}{\pi \cot \Lambda_j}\right]^2 + R^2(\xi_j) - \frac{2F(\xi_j)}{\pi} - \frac{2R_a f_1'(\xi_j)}{\pi \cot \Lambda_j} \right\}^{1/2} \\ 0 \leqq \xi_j \leqq \xi_T \end{aligned}\right\} \tag{A9}$$

The tip effect can be accounted for be defining the f functions to be

$$f_i = (f_i)_{\xi_j=\xi_T} - (f_i)_{\xi_j=\frac{\xi_j-\xi_T}{c_T}} \quad ; \quad \xi_T \leqq \xi_j \leqq 1 \tag{A10}$$

$$f_i = (f_i)_{\xi_j=1} \quad ; \quad 1 \leqq \xi_j \leqq \xi_T \tag{A11}$$

$$f_i = (f_i)_{\xi_j=1} - (f_i)_{\xi_j=\frac{\xi_j-\xi_T}{c_T}} \quad ; \quad 1 < \xi_T \leqq \xi_j \tag{A12}$$

and noting that in all cases

$$f_i' = 0 , \qquad \xi_j \geqq 1 \tag{A13}$$

WINGS OF VARYING THICKNESS TO CHORD RATIO

If the wing thickness to chord ratio varies linearly from root to tip, the preceding method for finding the indented body radii can be used by first replacing Z_1 in equation (A1) by the following

$$\left(\frac{\lambda_t-\lambda_c}{1-\lambda_c} - \frac{\lambda_t-1}{1-\lambda_c} c_1\right) Z_1$$

where λ_c is the ratio of tip chord to junction chord and λ_t is the ratio of tip thickness to chord ratio to junction thickness to chord ratio. The corresponding f' and f functions are then evaluated and used in conjunction with equations (A9) to (A13).

APPENDIX B

THE CALCULATION OF THE BODY SHAPES FOR MODELS I-C, II-C, AND III-C

The plan form and body-contouring details of models I-C, II-C, and III-C are presented in figures 3, 4(b), 5(b), and 6(b). The bodies used for these models were obtained by altering, without change in cross-sectional areas, the body shapes of models I-B, II-B, and III-B, respectively, by the application of axial multipoles so as to adjust the flow along the junction chord to agree identically with the flow over similar oblique wing sections for a design Mach number of 0.90.

A coordinate system made dimensionless with respect to the junction chord will be used, see sketch (b). The notation of reference 10 will be employed and the reader is referred to reference 10 for further details concerning the use of planar sources and axial multipoles to describe the subsonic flow about wing-body combinations.

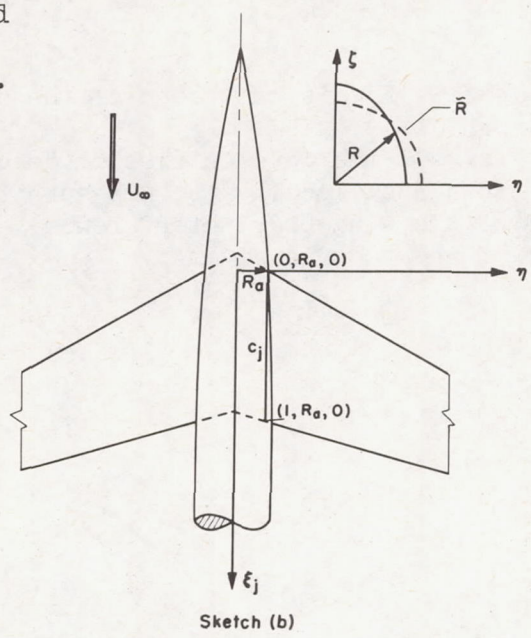

Sketch (b)

The first step toward a solution of the inverse problem described here is the calculation of the juncture pressure distribution due to the wing-alone sources and body axial sources ($\theta = 0^{\circ}$, M = 0.90),

$$\left(C_{P_j}\right)_{n=o} = -2(u_w+u_o)-\left[\breve{R}'+\Delta v_{(r)_w}\right]^2 \tag{B1}$$

where u_w is the streamwise perturbation velocity induced by the wing-alone sources, u_o is the streamwise perturbation velocity induced by the axial sources, $\tilde{R}'$ is the slope of the area-rule body, and the incremental radial velocity induced by the wing is defined as

$$\Delta v_{(r)_w} = v_{(r)_w} - \left[v_{(r)_w}\right]_{av}$$

where $v_{(r)_w}$ is the radial velocity induced by the wing and $\left[v_{(r)_w}\right]_{av}$ is the average radial-induced velocity (see ref. 10). The strengths of the axial sources to be used in the calculation of u_o are given by

$$A_o(\xi_j) = 2\pi\beta R\left\{\frac{\partial \beta R}{\partial \xi_j} - \left[v_{(r)_w}\right]_{av}\right\}$$

The next step involves the placement along the body axis of a suitable axial distribution of multipoles such that the juncture pressure distribution will be identical with that for the infinite oblique wing. The incremental adjustment of juncture pressures to be accomplished by the axial multipoles is therefore

$$\Delta C_{P_j} = C_{P_{\text{oblique wing}}} - \left(C_{P_j}\right)_{n=0} \tag{B2}$$

Since the influence on the pressure field decreases rapidly with the order of the multipole (ref. 10), it appears reasonable to consider only the multipole of order $n = 2$. The desired adjustment of the pressure coefficient is then ($\theta = 0^\circ$)

$$\Delta C_{P_j} = -2u_2 - \left[R'^2 - \left(\Delta v_{(r)_w}\right)^2\right] \tag{B3}$$

where R' is the slope of the desired body radius.

In the inverse problem described here, the axial quadripoles are used to adjust locally the pressure field but are not used to cancel any part of the wing-body interference velocities; consequently, the desired shape of the body is given by

$$R(\xi_j,\theta) = R^*(\xi_j,\theta) + \Delta R_2(\xi_j,\theta) \tag{B4}$$

where

$$R^*(\xi_j,\theta) = \tilde{R}(\xi_j) + \int_{-0.5}^{\xi_j} \Delta v_{(r)_w}\, d\bar{\xi} \tag{B5}$$

(The lower limit of the above integral is arbitrarily taken at $\bar{\xi} = -0.5$ since the influence of the wing is negligible forward of this point.) The parameter ΔR_2 in equation (B4) denotes the incremental change in body radius due to the axial multipole.

If use is made of the definitions of equations (B4) and (B5), equation (B3) can be written as ($\theta = 0^\circ$)

$$\Delta C_{P_j} = -2u_2 - (\Delta R_2')^2 - 2\Delta R_2' R^{*\prime} \tag{B6}$$

where

$$\Delta R_2' = R' - R^{*'} \tag{B7}$$

The desired body shape is to be obtained by solution of equation (B6). First, however, it is necessary to relate the streamwise perturbation u_2 to the parameter ΔR_2. This is easily achieved if the following slender-body approximation for multipole theory (ref. 25) is used:

$$\varphi_n(x,r,\theta) = \frac{a_n(x)\cos n\theta}{r^n} + \frac{b_n(x)\sin n\theta}{r^n} \tag{B8}$$

The streamwise and radial perturbation velocities for the quadripole are

$$u_2(x,r,\theta) = \frac{a_2'(x)\cos 2\theta}{r^2} \tag{B9}$$

$$v_{(r)_2}(x,r,\theta) = \frac{-2a_2(x)\cos 2\theta}{r^3} \tag{B10}$$

The axial strength distribution for the quadripole can be related to body geometry at $\theta = 0^\circ$ as follows:

$$v_{(r)_2} = \frac{-2a_2(x)}{R^3} = R' - R^{*'}$$

$$= \Delta R_2'$$

$$a_2(x) = \frac{-R^3 \Delta R_2'}{2} \tag{B11}$$

$$\frac{a_2'(x)}{R^2} = \frac{-R\Delta R_2''}{2} \frac{-3R'\Delta R_2'}{2} \tag{B12}$$

It is now possible to express equation (B6) as

$$\Delta C_{P_j} = R^*\Delta R_2'' + \Delta R_2 \Delta R_2'' + R^{*\prime}\Delta R' + 2(\Delta R_2')^2 \tag{B13}$$

which can be approximated by

$$\frac{\Delta C_{P_j}}{R^*} = \Delta R_2'' + \frac{R^{*\prime}\Delta R_2'}{R^*} \tag{B14}$$

(Eq. (B14) indicates that the pressure adjustment due to an axial distribution of quadripoles for bodies having small $\tilde{R}'$ is directly proportional to the second derivative of the radial modification.)

For the application described here (the design of models I-C, II-C, and III-C) equation (B14) was solved by an iteration procedure starting with the approximation

$$\Delta R_2' = \int_{\xi_a}^{\xi_j} \frac{\Delta C_{P_j}}{R^*}\, d\bar{\xi} \tag{B15}$$

$$\Delta R_2 = \int_{\xi_a}^{\xi_j} \Delta R_2'\, d\bar{\xi} \tag{B16}$$

where $\xi_j = \xi_a$ is the starting (or reference) point and

$$\Delta R_2(\xi_a) = \Delta R_2'(\xi_a) = 0$$

The starting points (see figs. 7 to 9) were found to be somewhat critical if the body shapes were to remain practical. Solutions of equation (B14) were obtained along the wing-body junctures and arbitrary fairings were used to terminate the body modifications fore and aft of the junction chords.

The solution for ΔR_2 at $\theta = 0$ is equivalent to finding the strength distribution for the quadripoles. At finite θ values, ΔR_2 can be obtained by an iteration of the following:

$$v_{(r)_2} = \frac{-2a_2 \cos 2\theta}{R^3} \tag{B17}$$

$$R = R^* + \int_{\xi_a}^{\xi_j} v_{(r)_2} d\bar{\xi} \tag{B18}$$

An alternate iteration procedure for obtaining the desired body shape is obtained if equation (B17) is written in the form

$$R' - R^{*'} = \frac{-2a_2 \cos 2\theta}{R^3}$$

or

$$R^3 R' = R^3 R^{*'} - 2a_2 \cos 2\theta \tag{B19}$$

and finally

$$R^4(\xi_j) = \left[R^4(\xi_a) + 4 \int_{\xi_a}^{\xi_j} R^3 R^{*'} d\bar{\xi} - 8 \cos 2\theta \int_{\xi_a}^{\xi_j} a_2(\xi_1) d\bar{\xi} \right]^{1/4} \tag{B20}$$

As a first approximation, R in the right-hand side of equation (B20) can be replaced by

$$R = R^* - 2 \cos 2\theta \int_{\xi_a}^{\xi_j} \frac{a_2}{R^{*3}} d\bar{\xi} \tag{B21}$$

REFERENCES

1. Göthert, B.: Berechnung des Geschwindigkeitsfeldes von Pfeilfuegeln bei Hohen Unterschallgeschwindigkeiten. Ministry of Supply, GDC 10/6081 L/T. (Also available as MOS (Volkenrode) Rep. & Trans. 387.)

2. Jones, Robert T.: Subsonic Flow Over Thin Oblique Airfoils at Zero Lift. NACA Rep. 902, 1948. (Supersedes NACA TN 1340)

3. Jones, Robert T.: Thin Oblique Airfoils at Supersonic Speed. NACA TN 1107, 1946.

4. Neumark, Stefan: Velocity Distribution on Straight and Sweptback Wings of Small Thickness and Infinite Aspect Ratio at Zero Incidence. R.A.E. Rep. No. Aero. 2200, British, May 1947.

5. Watkins, Charles E.: The Streamline Pattern in the Vicinity of an Oblique Airfoil. NACA TN 1231, 1947.

6. Boddy, Lee E.: Investigation at High Subsonic Speeds of Methods of Alleviating the Adverse Interference at the Root of a Swept-Back Wing. NACA RM A50E26, 1950.

7. Pepper, William B., Jr.: The Effect on Zero-Lift Drag of an Indented Fuselage or a Thickened Wing-Root Modification to a 45° Swept-Back Wing-Body Configuration as Determined by Flight Tests at Transonic Speeds. NACA RM L51F15, 1951.

8. Küchemann, D.: Design of Wing Junction, Fuselage and Nacelles to Obtain the Full Benefit of Sweptback Wings at High Mach Number. R.A.E. Rep. No. Aero. 2219, British, Oct. 1947.

9. Weber, J.: Design of Wing Junction, Fuselage and Nacelles to Obtain the Full Benefit of Sweptback Wings at High Mach Number. Addendum: Additional Tables of Coefficients. R.A.E. Rep. No. Aero. 2219a, British, May 1949.

10. McDevitt, John B.: The Linearized Subsonic Flow About Symmetrical, Nonlifting Wing-Body Combinations. NACA TN 3964, 1956.

11. Wind Tunnel Staff: Design of Body-Wing Junctions for High Subsonic M, for Swept Back Wings and Symmetrical Bodies. R.A.E. Rep. No. Aero. 2336, British, Sept. 1949.

12. McDevitt, John B., and Haire, William M.: Investigation at High Subsonic Speeds of a Body-Contouring Method for Alleviating the Adverse Interference at the Root of a Sweptback Wing. NACA RM A54A22, 1954.

13. Hartley, D. E.: Investigation at High Subsonic Speeds of Wing-Fuselage Intersection Shapes for Sweptback Wings. Part I. Force Measurements on Some Initial Designs. R.A.E. Rep. No. Aero. 2464, British, May 1952.

14. Hartley, D. E.: Investigation at High Subsonic Speeds of Wing-Fuselage Intersection Shapes for Sweptback Wings. Part II. Pressure Measurements on Some Initial Designs. R.A.E. Rep. No. Aero. 2503, British, Dec. 1953.

15. Whitcomb, Richard T.: A Study of the Zero-Lift Drag-Rise Characteristics of Wing-Body Combinations Near the Speed of Sound. NACA RM L52H08, 1952.

16. Jones, Robert T.: Theory of Wing-Body Drag at Supersonic Speeds. NACA RM A53H18a, 1953.

17. Whitcomb, Richard T., and Fischetti, Thomas L.: Development of a Supersonic Area Rule and an Application to the Design of a Wing-Body Combination Having High Lift-To-Drag Ratios. NACA RM L53H31a, 1953.

18. McDevitt, John B.: An Experimental Investigation of Two Methods for Reducing Transonic Drag of Swept-Wing and Body Combinations. NACA RM A55B21, 1955.

19. Howell, Robert R., and Braslow, Albert L.: An Experimental Study of a Method of Designing the Sweptback-Wing--Fuselage Juncture for Reducing the Drag at Transonic Speeds. NACA RM L54L31a, 1955.

20. Howell, Robert R.: Experimental Study of a Method of Designing the Sweptback-Wing--Fuselage Juncture to Reduce the Drag at Moderate Supersonic Speeds. NACA RM L55H05a, 1956.

21. Palmer, William E., Howell, Robert R., and Braslow, Albert L.: Transonic Investigation at Lifting Conditions of Streamline Contouring in the Sweptback-Wing--Fuselage Juncture in Combination With the Transonic Area Rule. NACA RM L56D11a, 1956.

22. Holdaway, George H.: Comparison of Theoretical and Experimental Zero-Lift Drag-Rise Characteristics of Wing-Body-Tail Combinations Near the Speed of Sound. NACA RM A53H17, 1953.

23. Graham, Ernest W.: The Pressure on a Slender Body of Non Uniform Cross-Sectional Shape in Axial Supersonic Flow. Jour. Aero. Sci., vol. 17, no. 3, Mar. 1950, pp. 173-175, 192.

24. Lomax, Harvard: The Wave Drag of Arbitrary Configurations in Linearized Flow as Determined by Areas and Forces in Oblique Planes. NACA RM A55A18, 1955.

25. Adams, Mac C., and Sears, W. R.: Slender-Body Theory -- Review and Extension. Jour. Aero. Sci., vol. 20, no. 2, Feb. 1953, pp. 85-98.

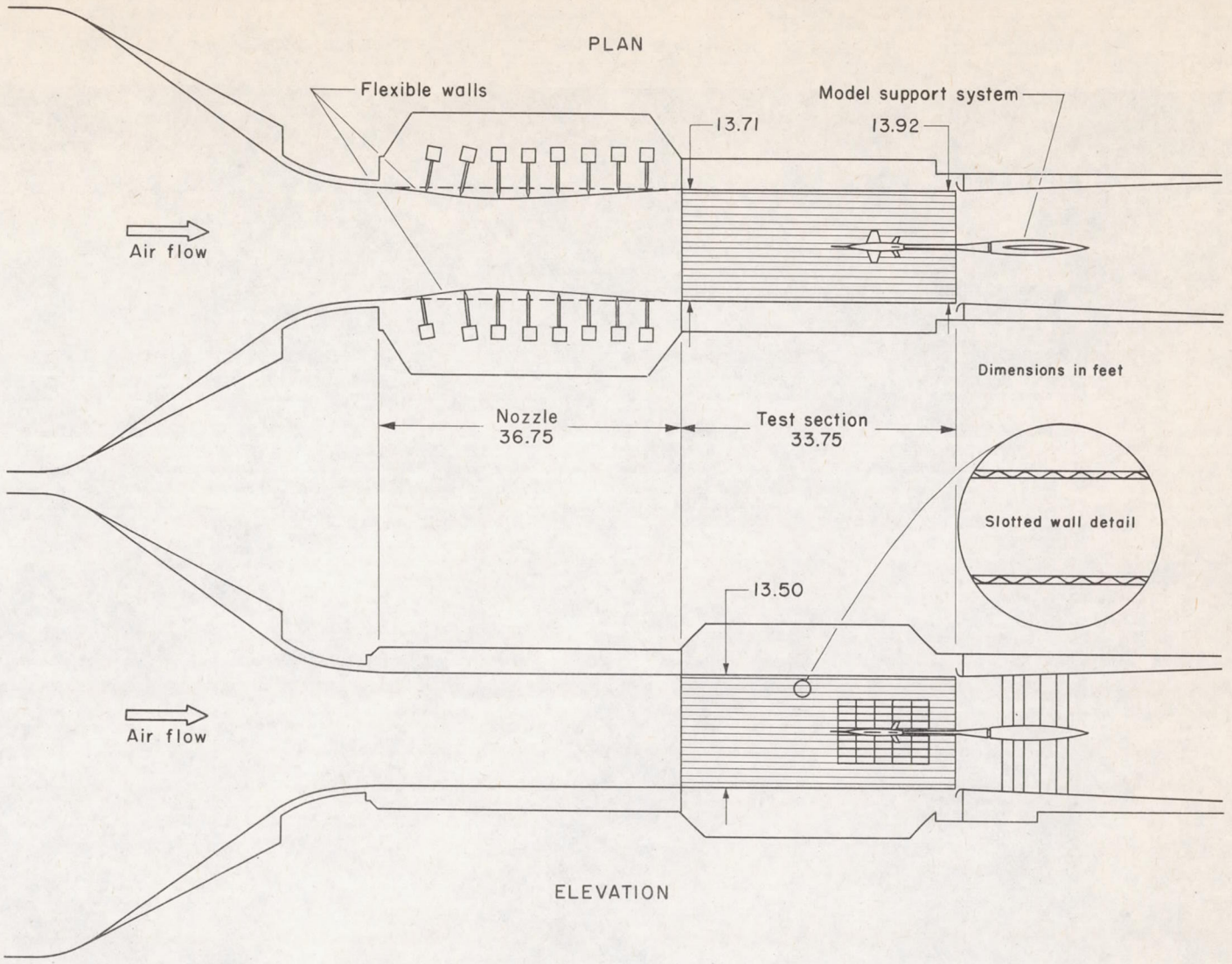

Figure 1.- General arrangement of the test section of the Ames 14-foot transonic wind tunnel.

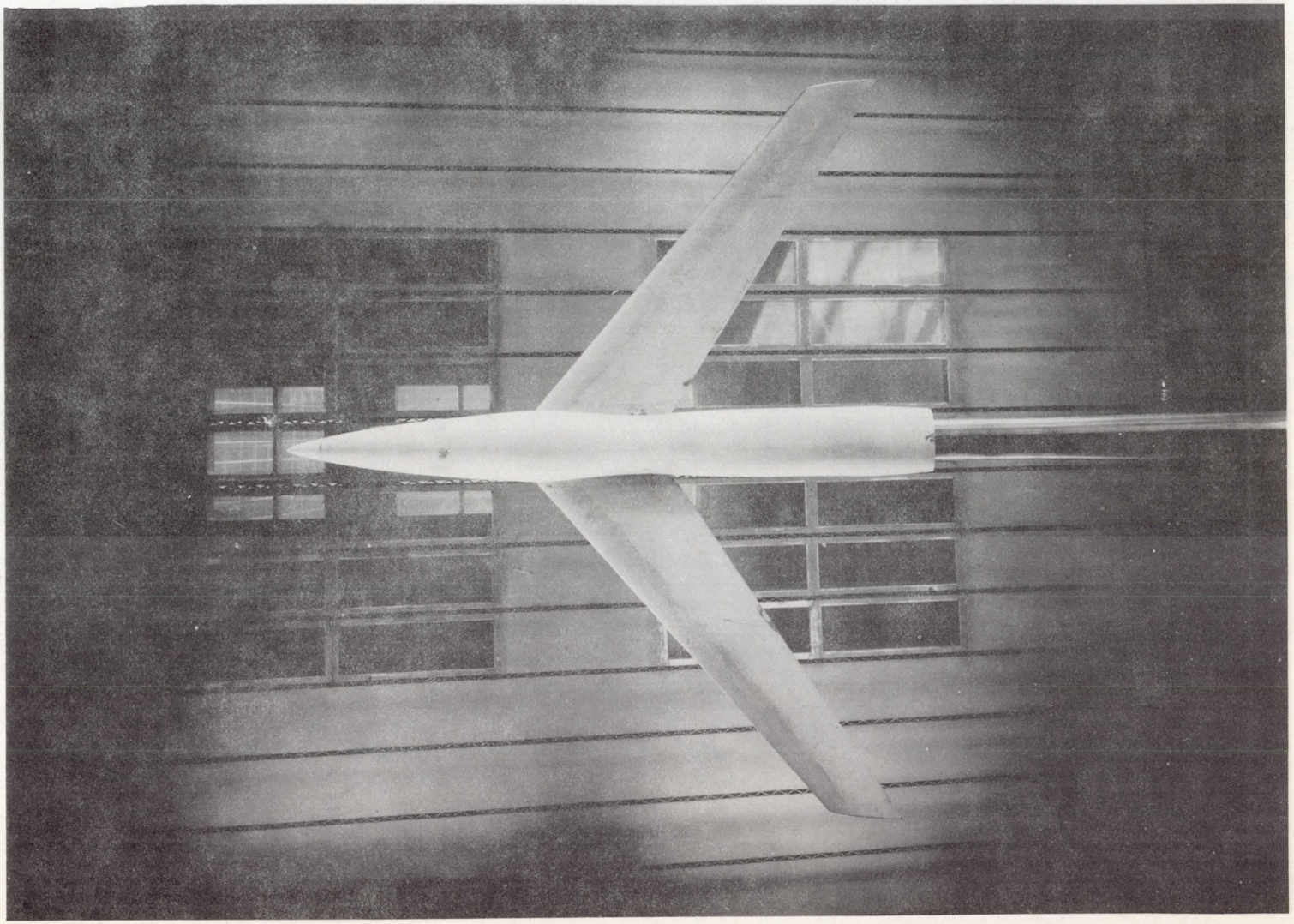

Figure 2.- A sting-mounted model in the Ames 14-foot transonic wind tunnel A-20799

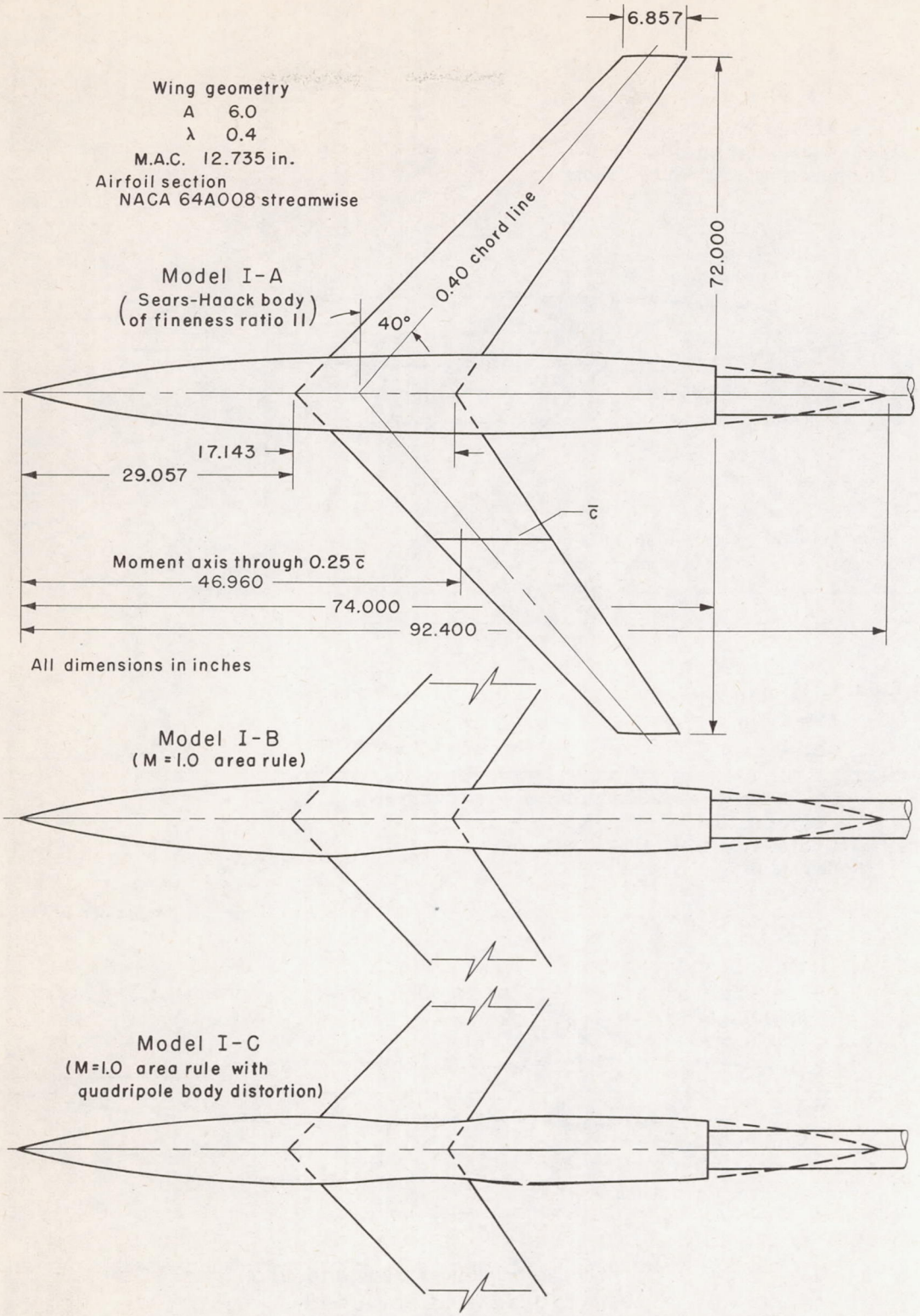

(a) Model series I.

Figure 3.- Plan-form details of the models.

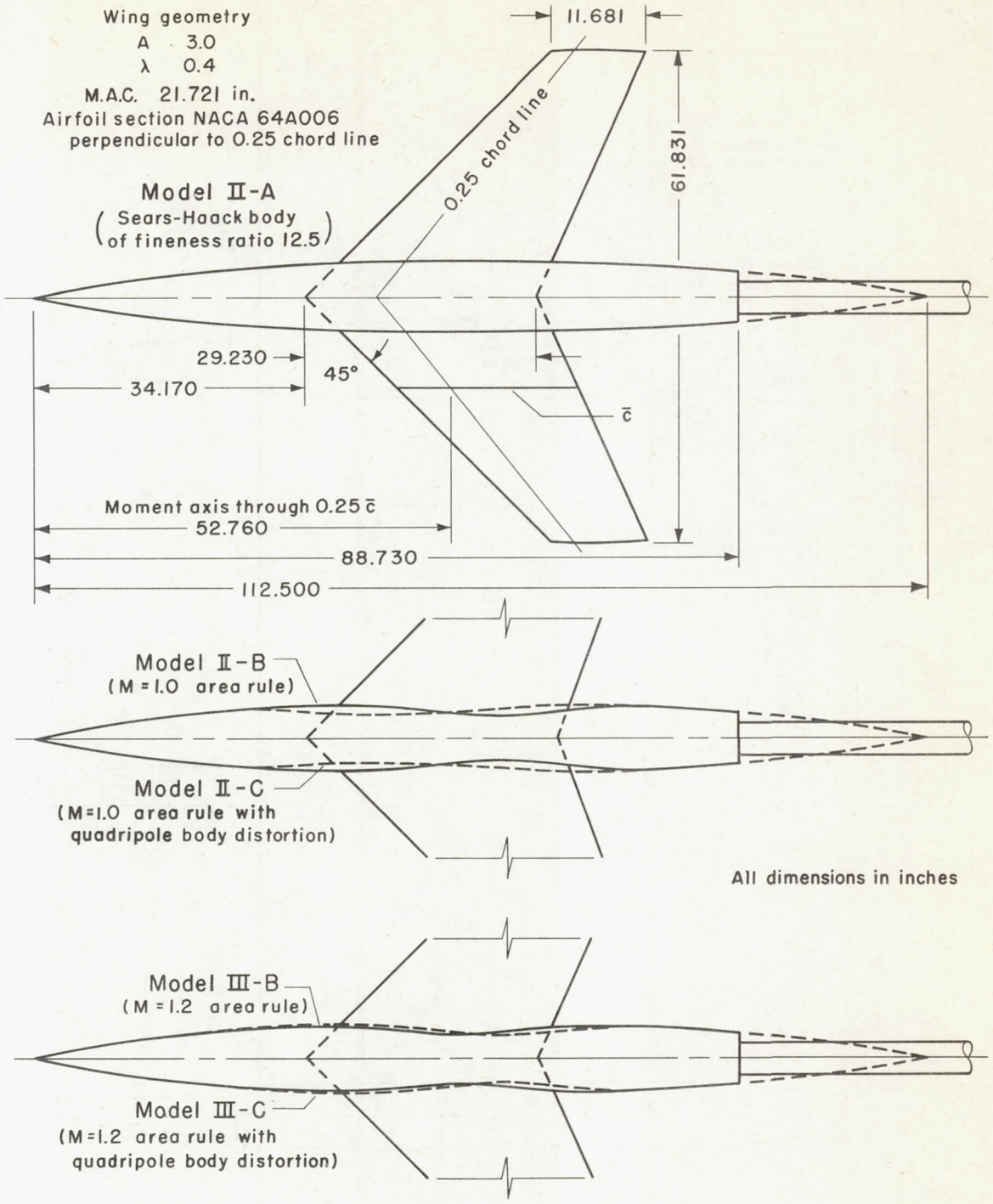

(b) Model series II and III.

Figure 3.- Concluded.

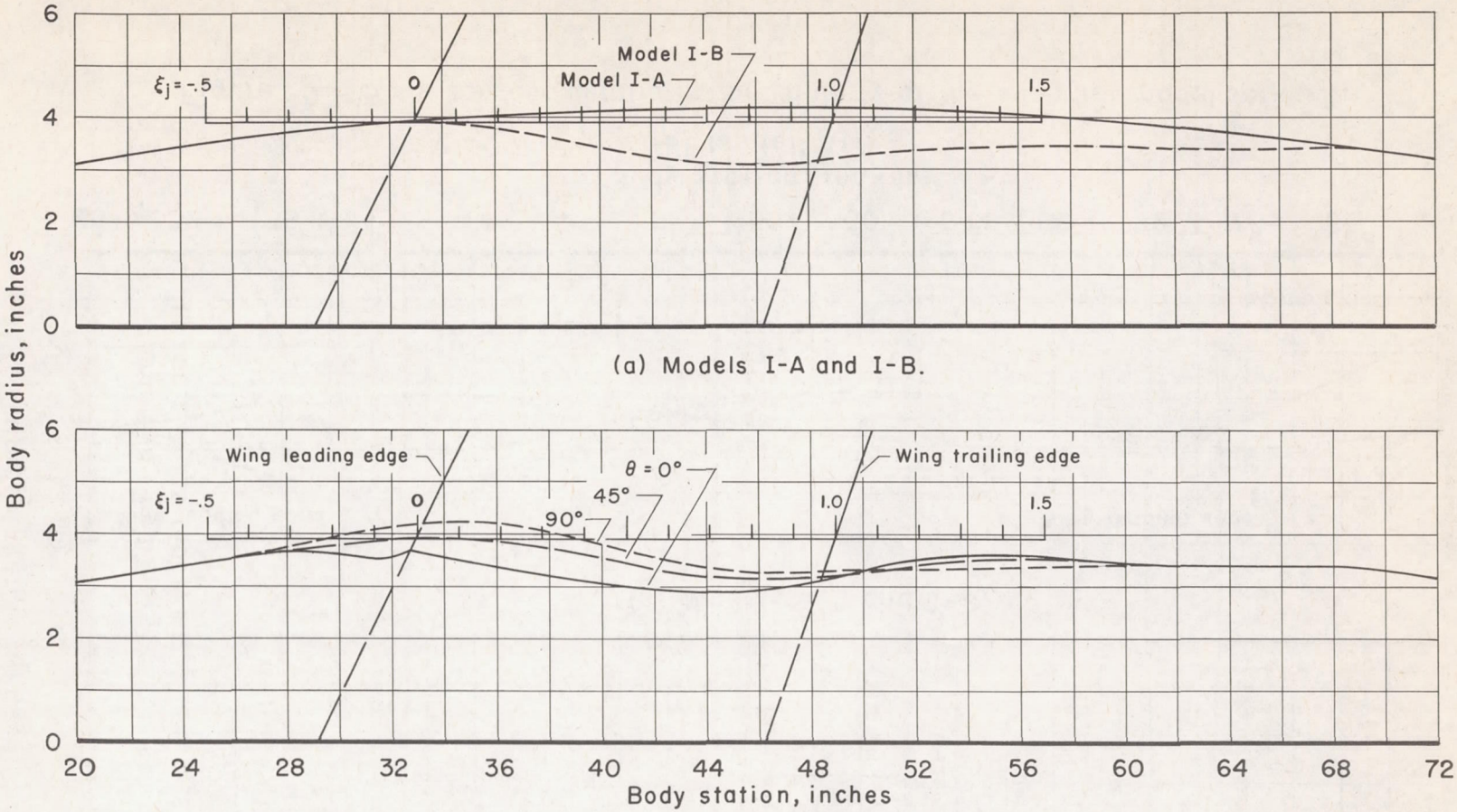

(a) Models I-A and I-B.

(b) Model I-C.

Figure 4.- Body contour details in the vicinity of the wing for model series I.

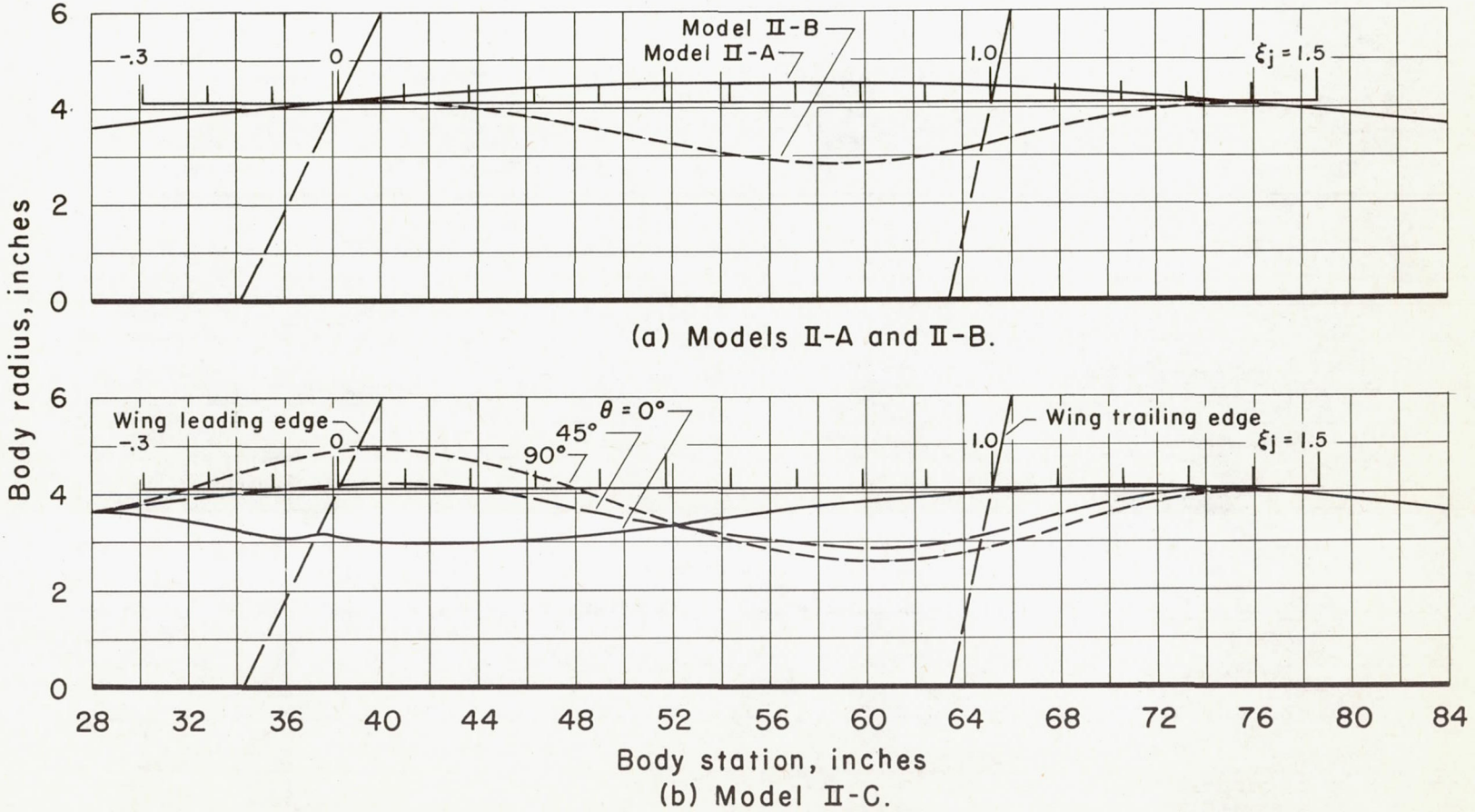

Figure 5.- Body contour details in the vicinity of the wing for model series II.

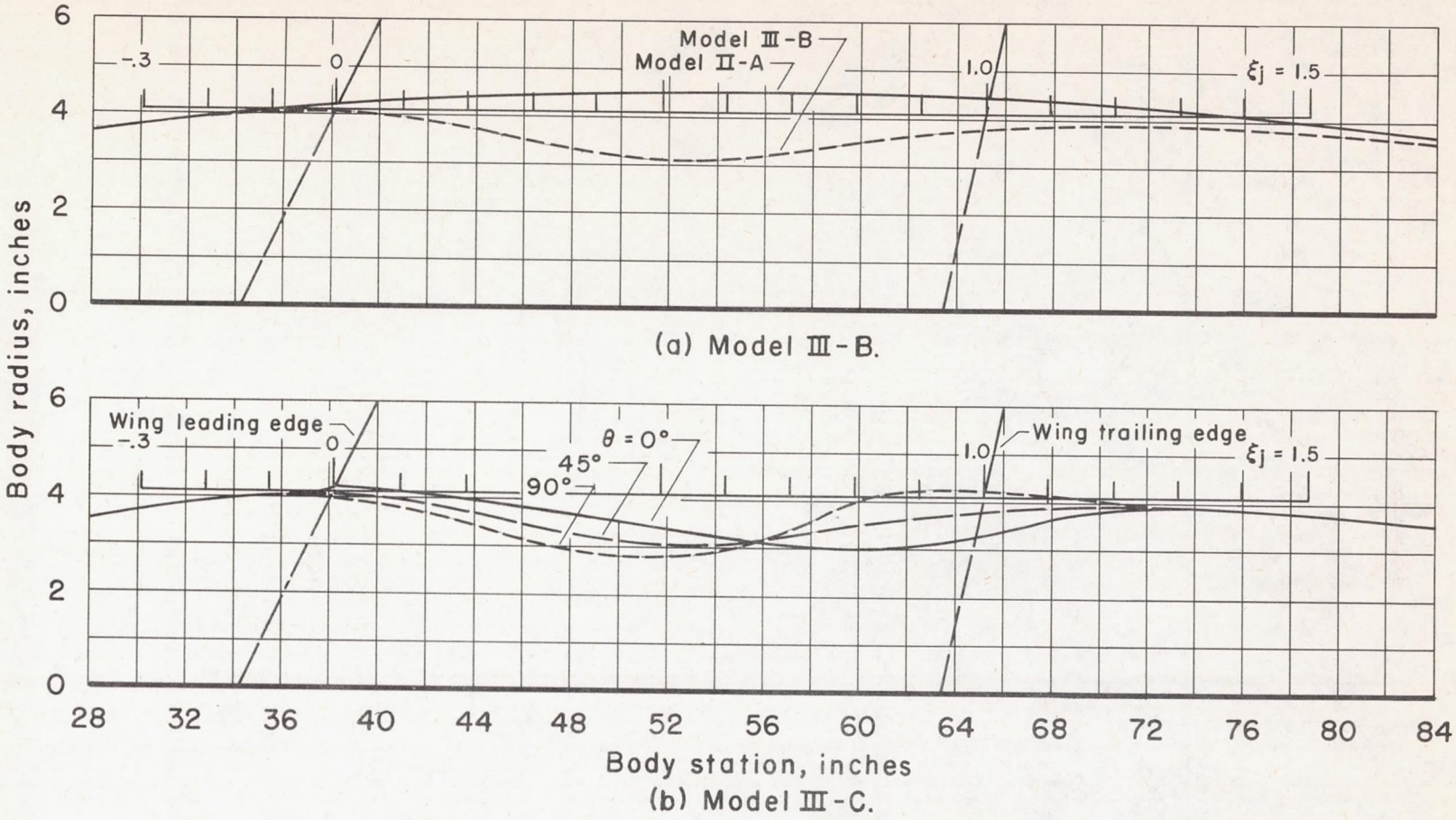

Figure 6.- Body contour details in the vicinity of the wing for model series III.

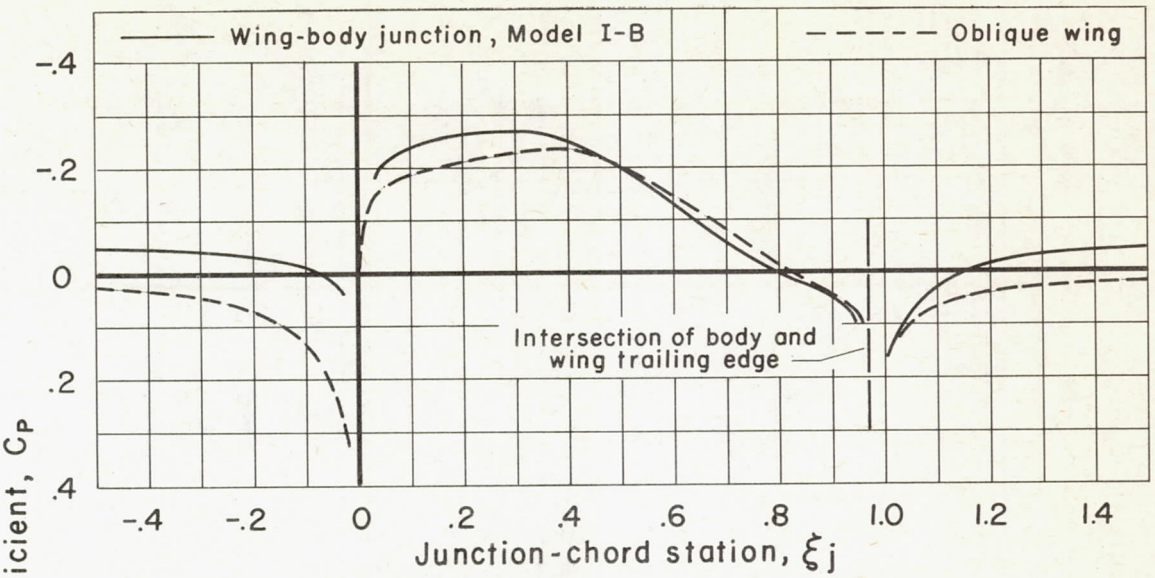

(a) Calculated pressure distributions at the wing-body juncture of model I-B and for the oblique wing.

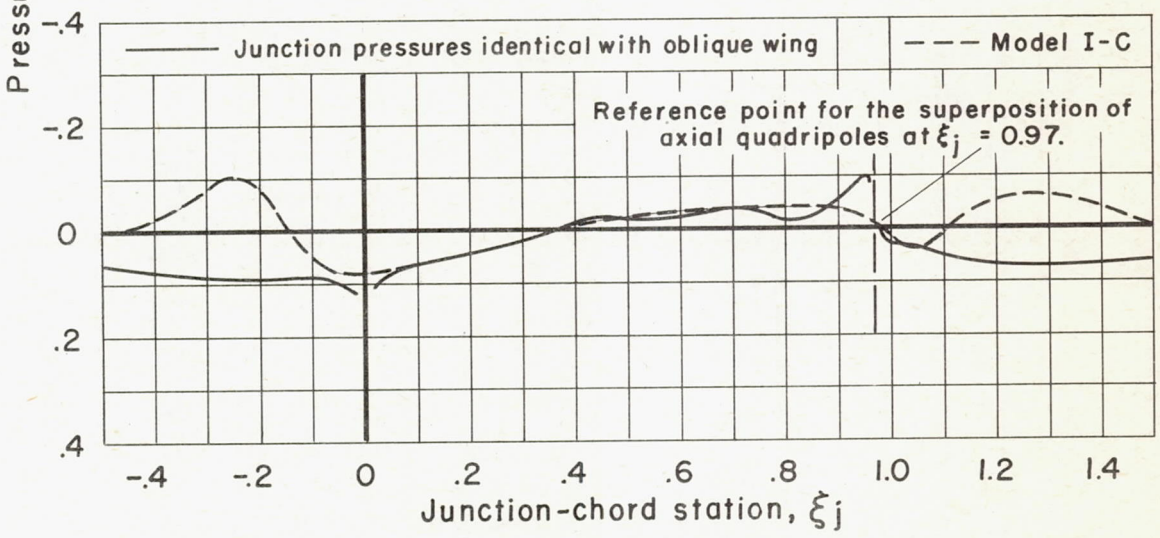

(b) Incremental adjustment of junction pressure required by the axial quadripoles of body I-C.

Figure 7.- Theoretical calculations (M_{des} = 0.90) considered in the body design of model I-C.

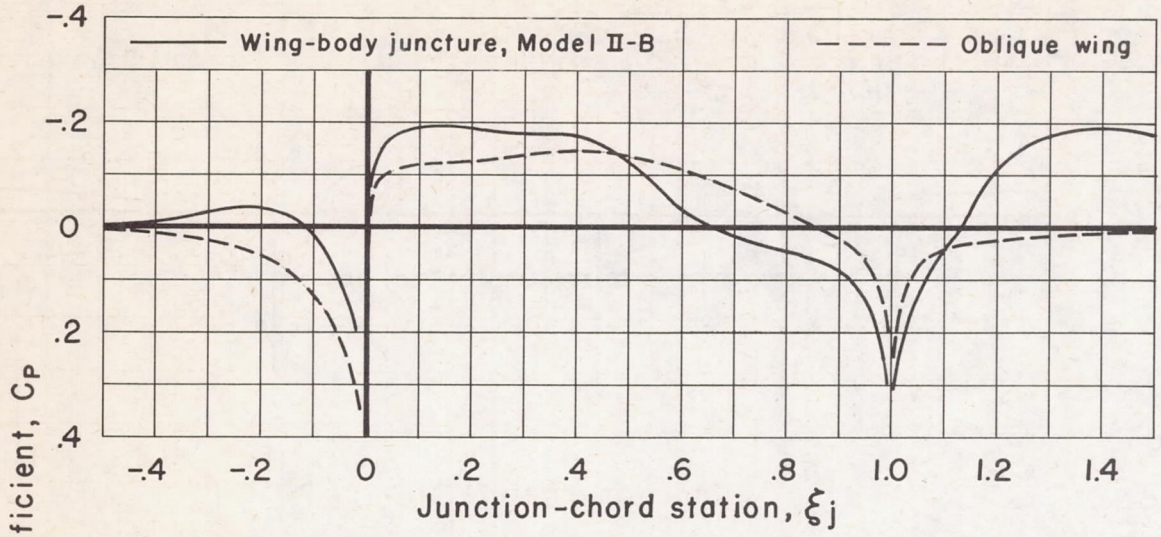

(a) Calculated pressure distributions at the wing-body juncture of model II-B and for the oblique wing.

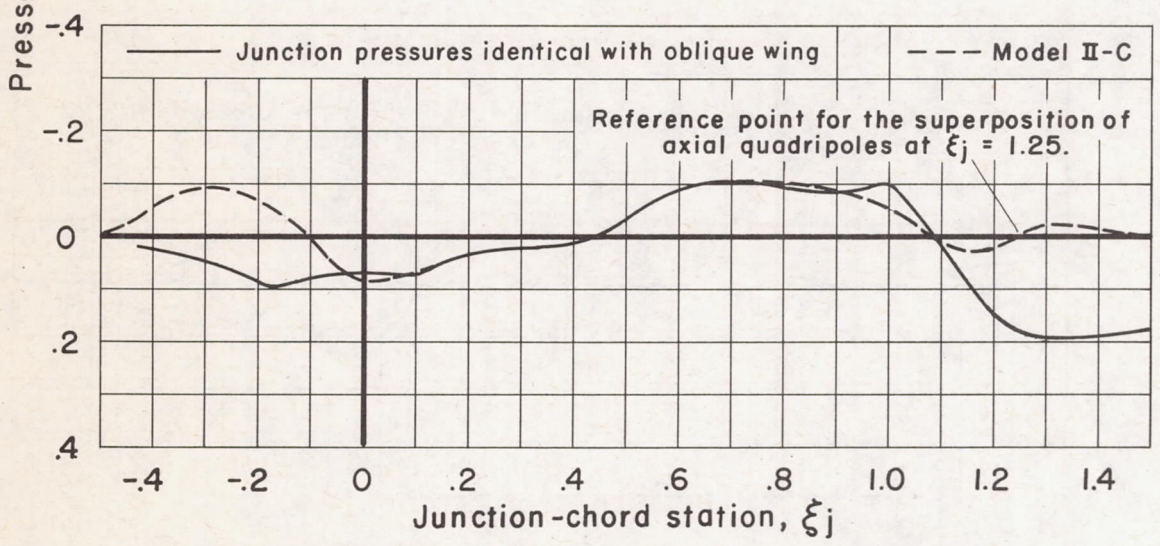

(b) Incremental adjustment of junction pressure required by the axial quadripoles of body II-C.

Figure 8.- Theoretical calculations (M_{des} = 0.90) considered in the body design of model II-C.

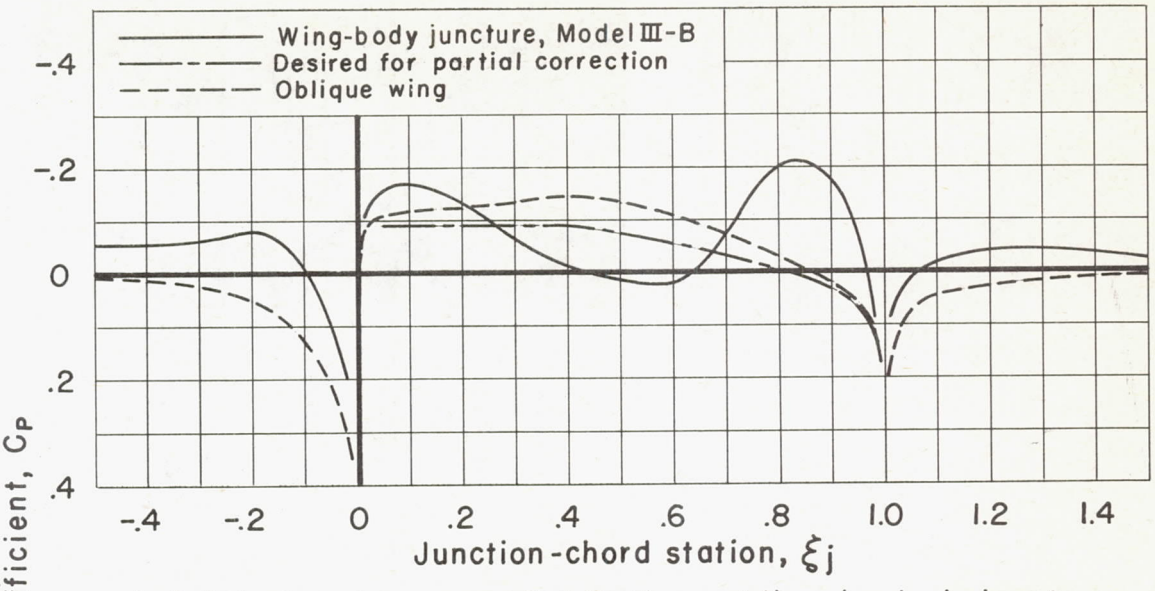

(a) Calculated pressure distributions at the wing-body juncture of model III-B and for the oblique wing.

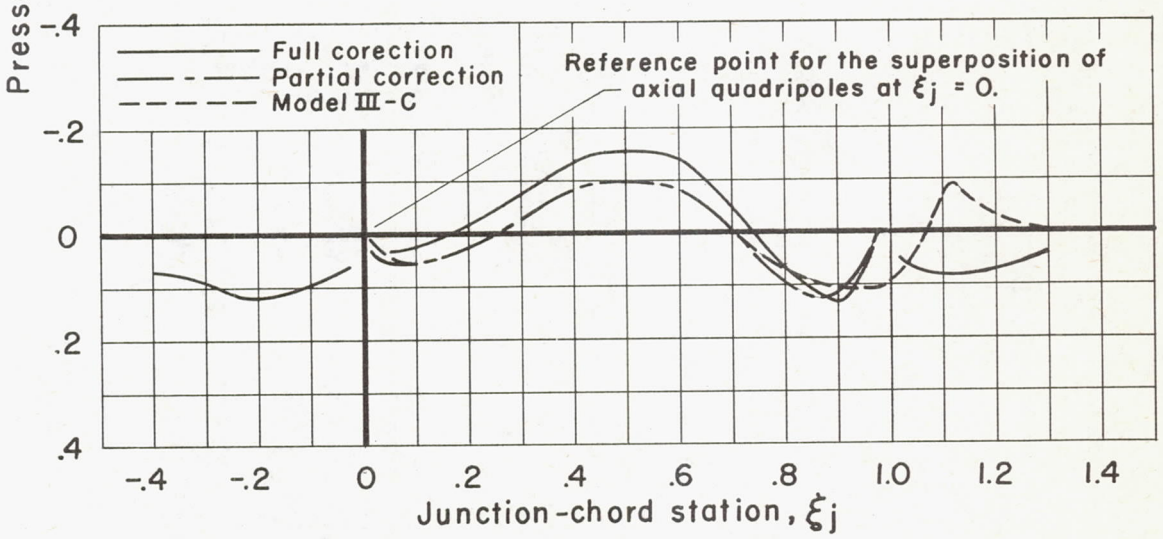

(b) Incremental adjustment of junction pressure required by the axial quadripoles of body III-C.

Figure 9.- Theoretical calculations (M_{des} = 0.90) considered in the body design of model III-C.

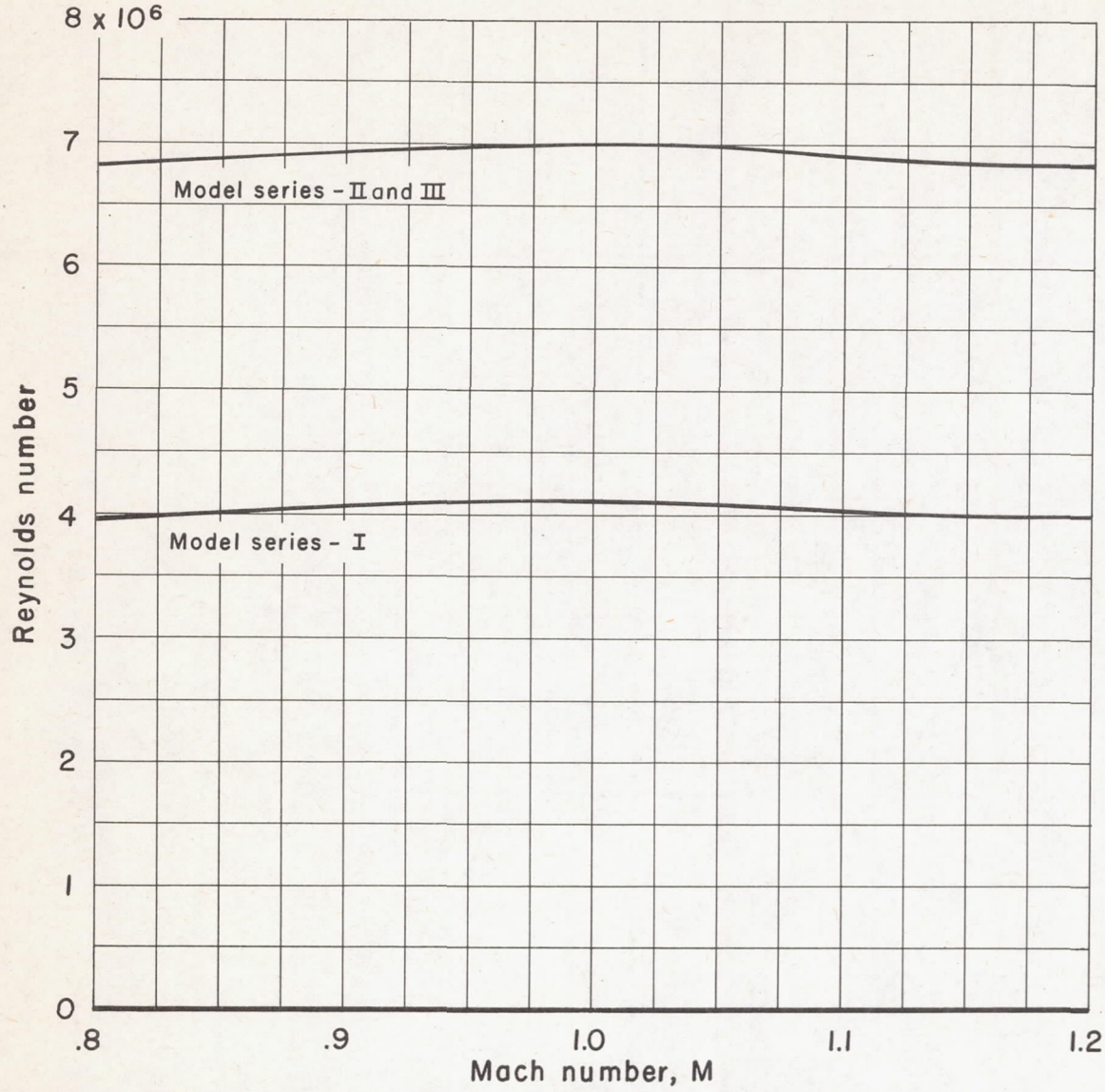

Figure 10.- The variation of average test Reynolds number with Mach number.

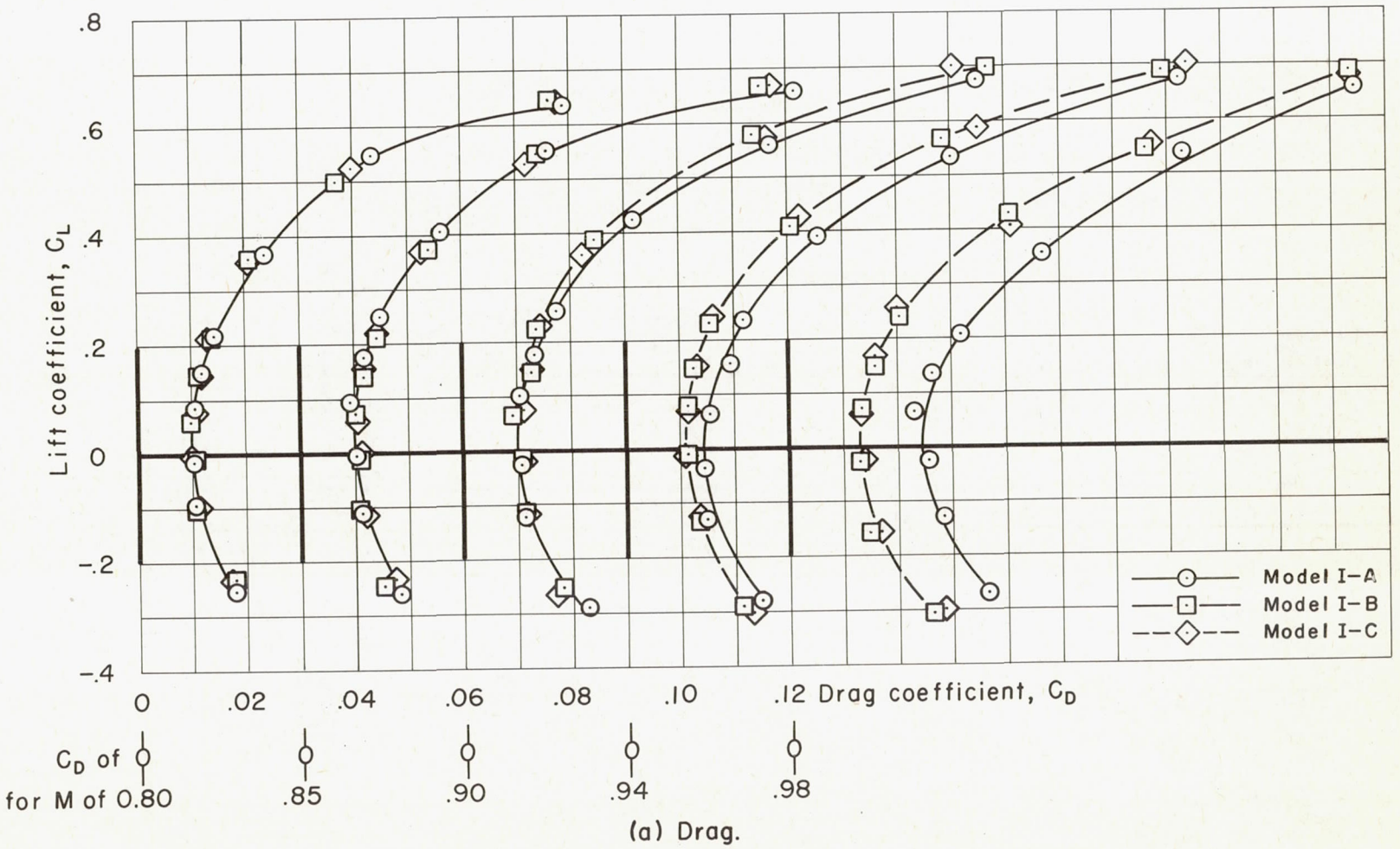

(a) Drag.

Figure 11.- Drag, lift, and pitching-moment characteristics of the models of series I.

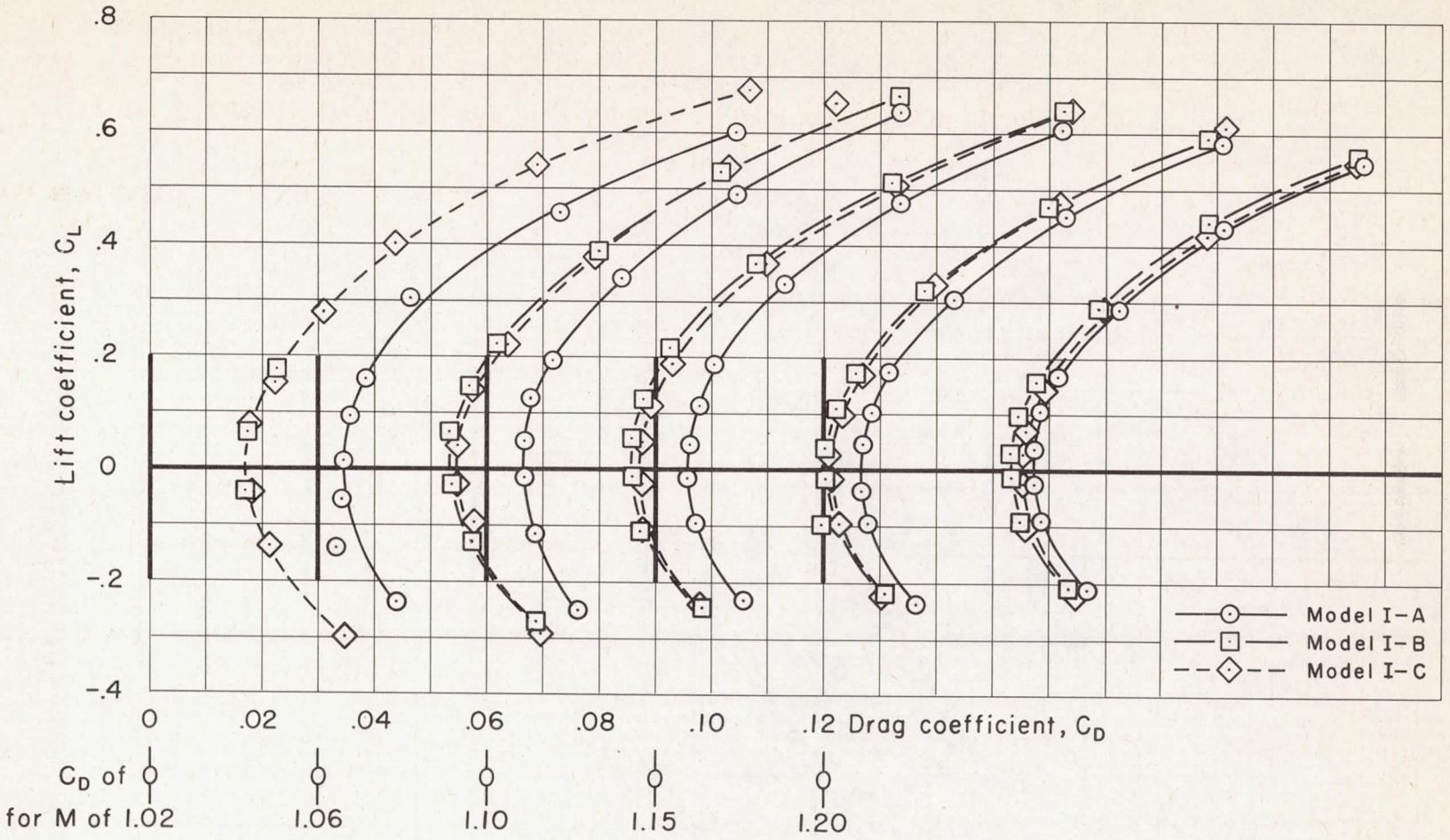

(a) Drag – Concluded.

Figure 11.- Continued.

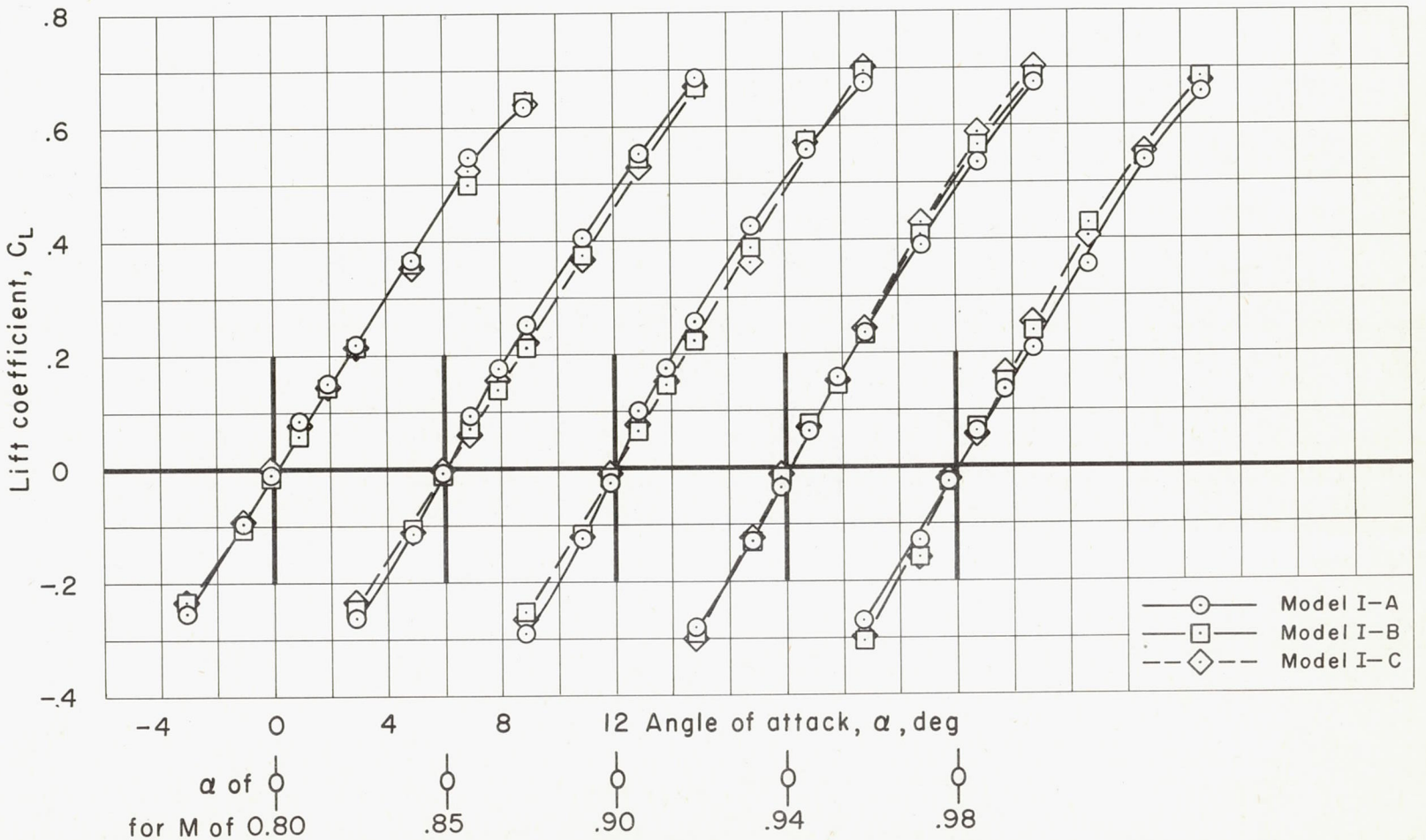

(b) Lift.

Figure 11.- Continued.

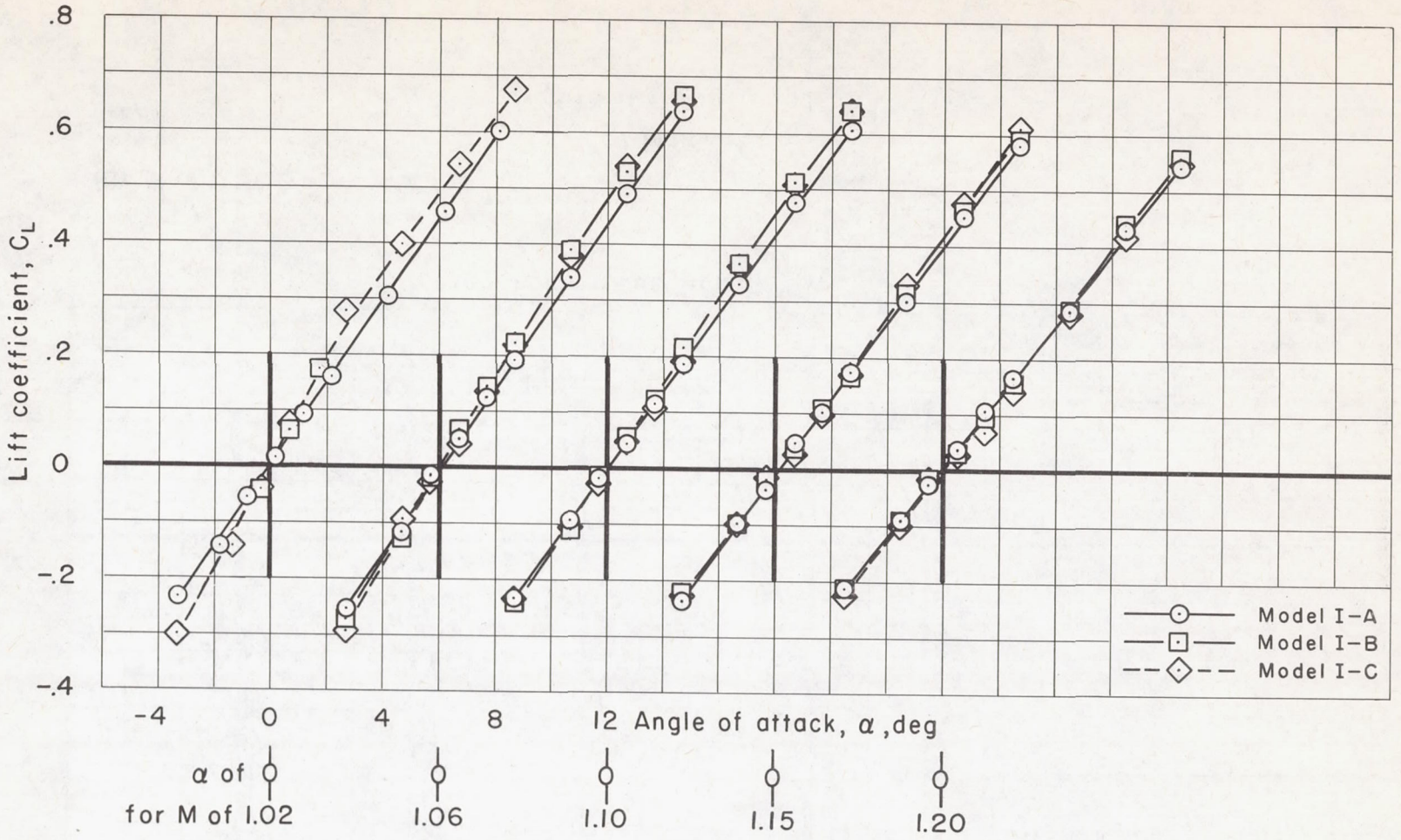

(b) Lift – Concluded.

Figure 11.- Continued.

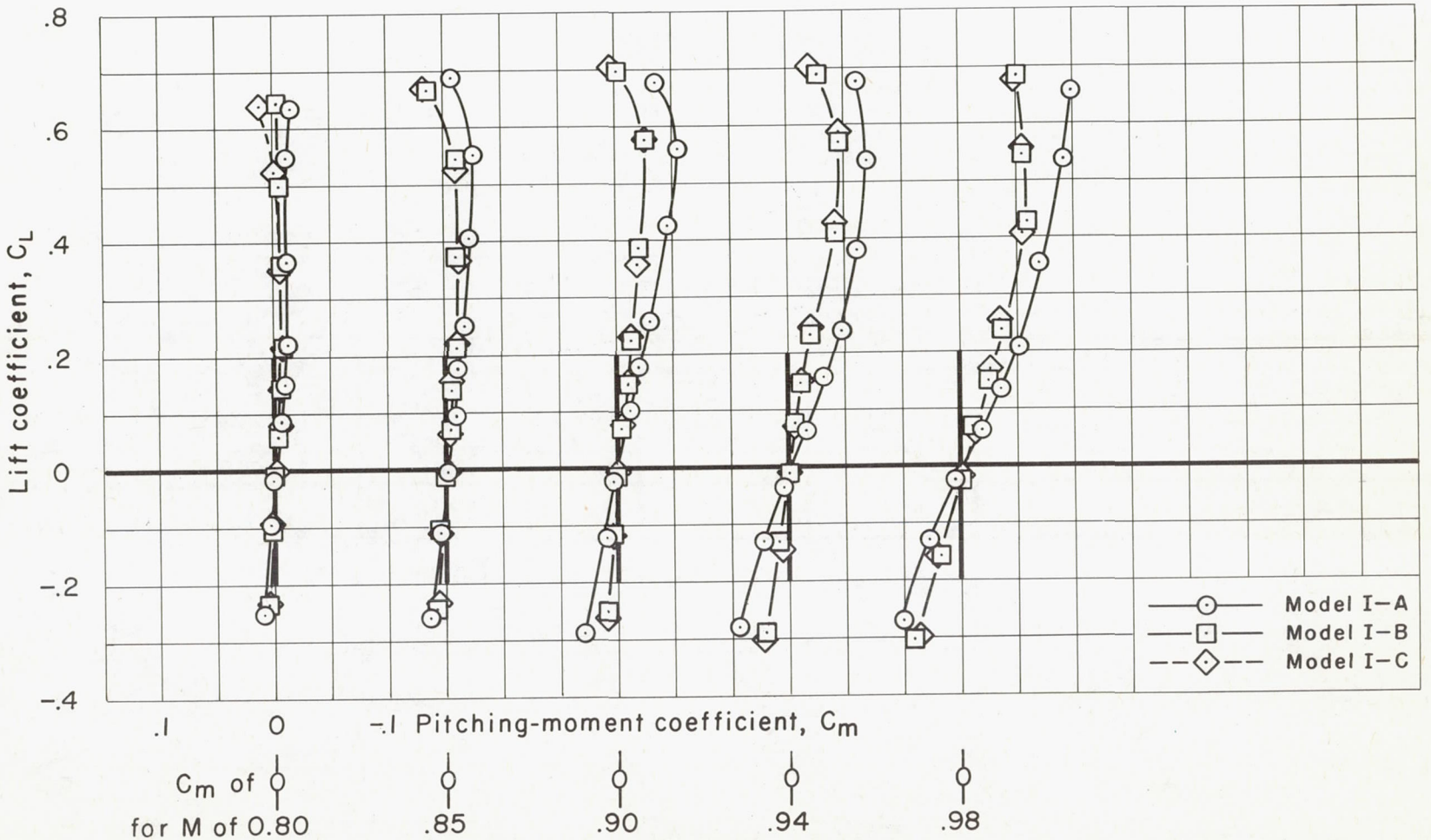

(c) Moment.

Figure 11.- Continued.

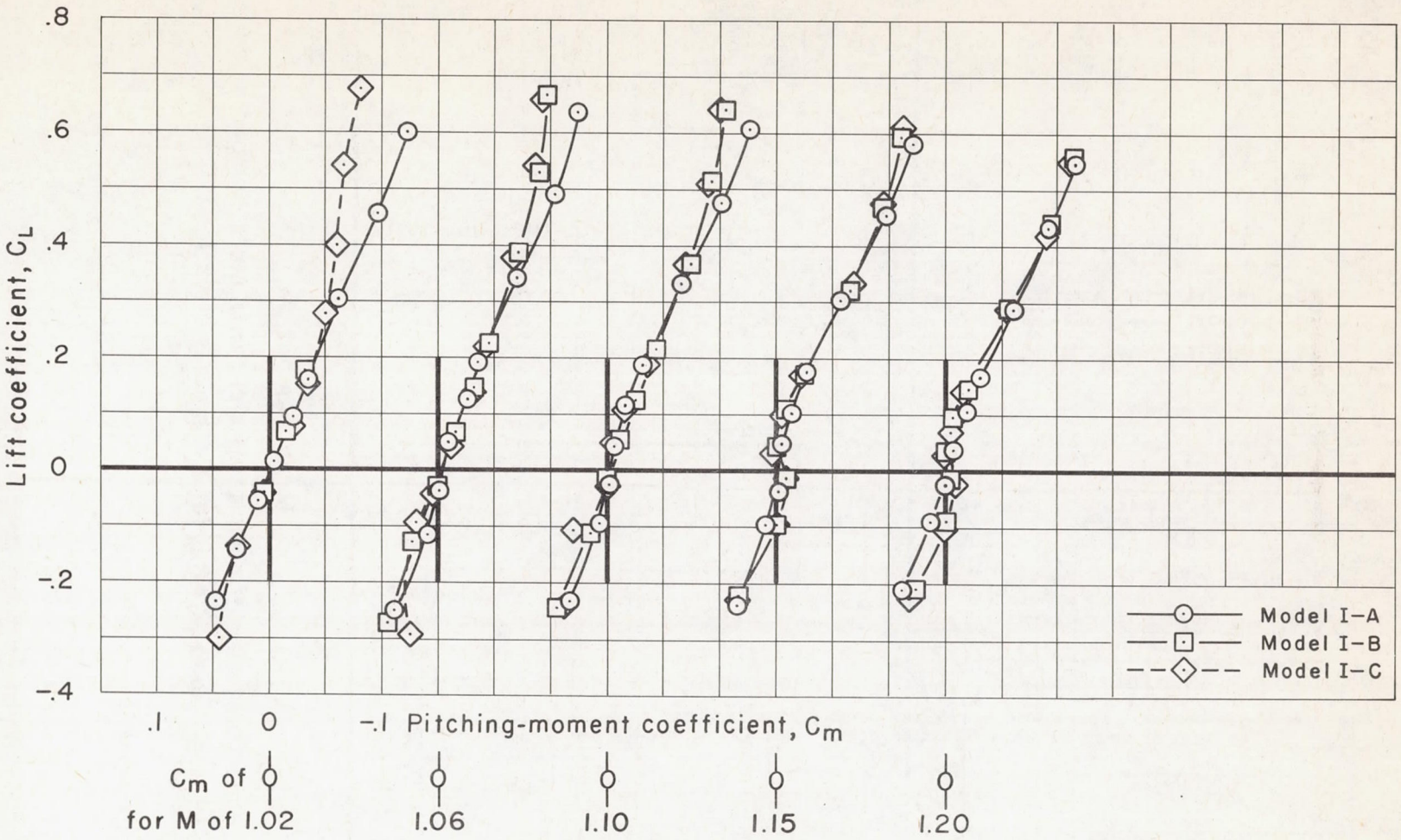

(c) Moment — Concluded.

Figure 11.- Concluded.

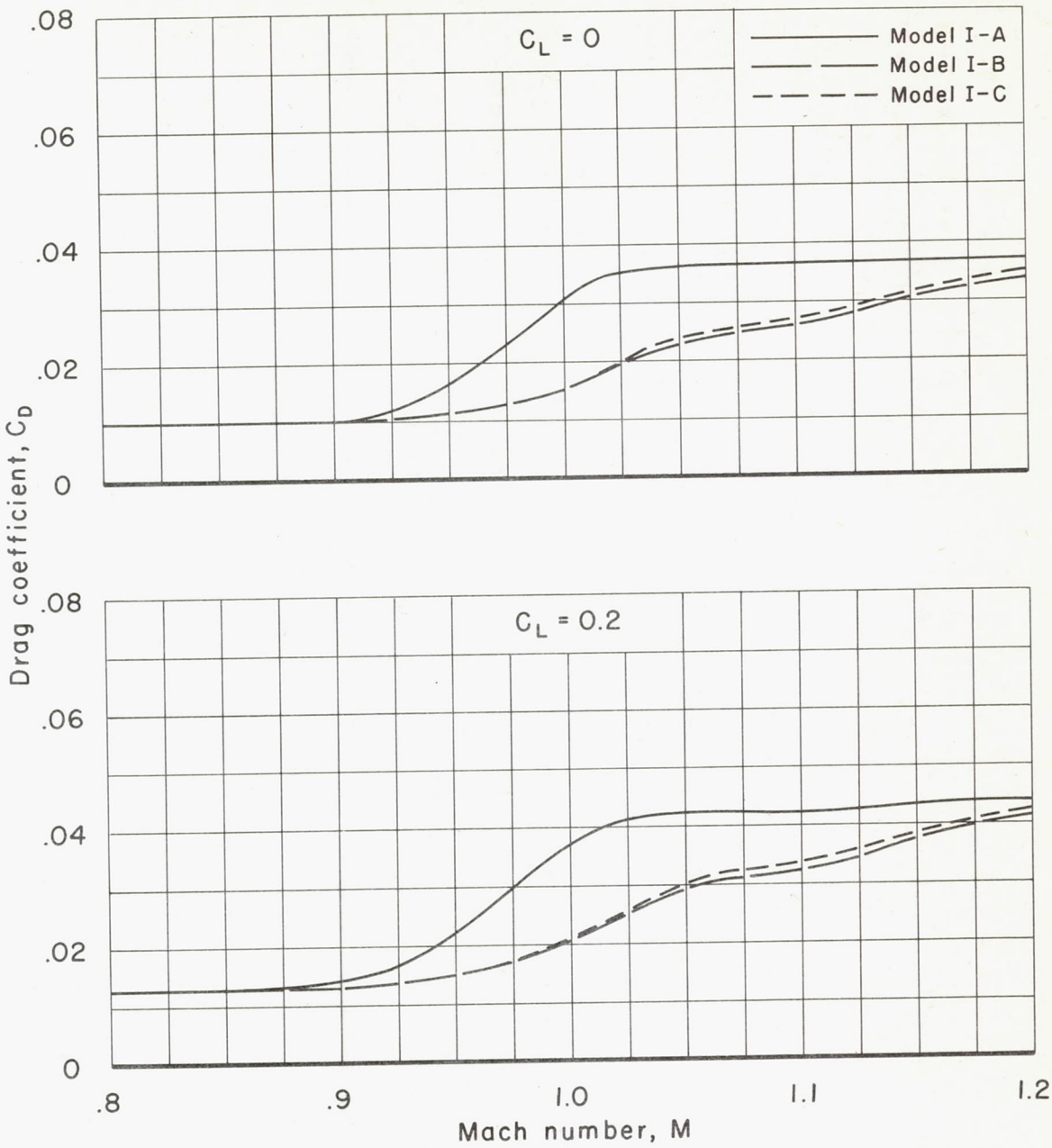

Figure 12.- The variation of drag coefficient with Mach number at zero lift and C_L=0.2 for the models of series I.

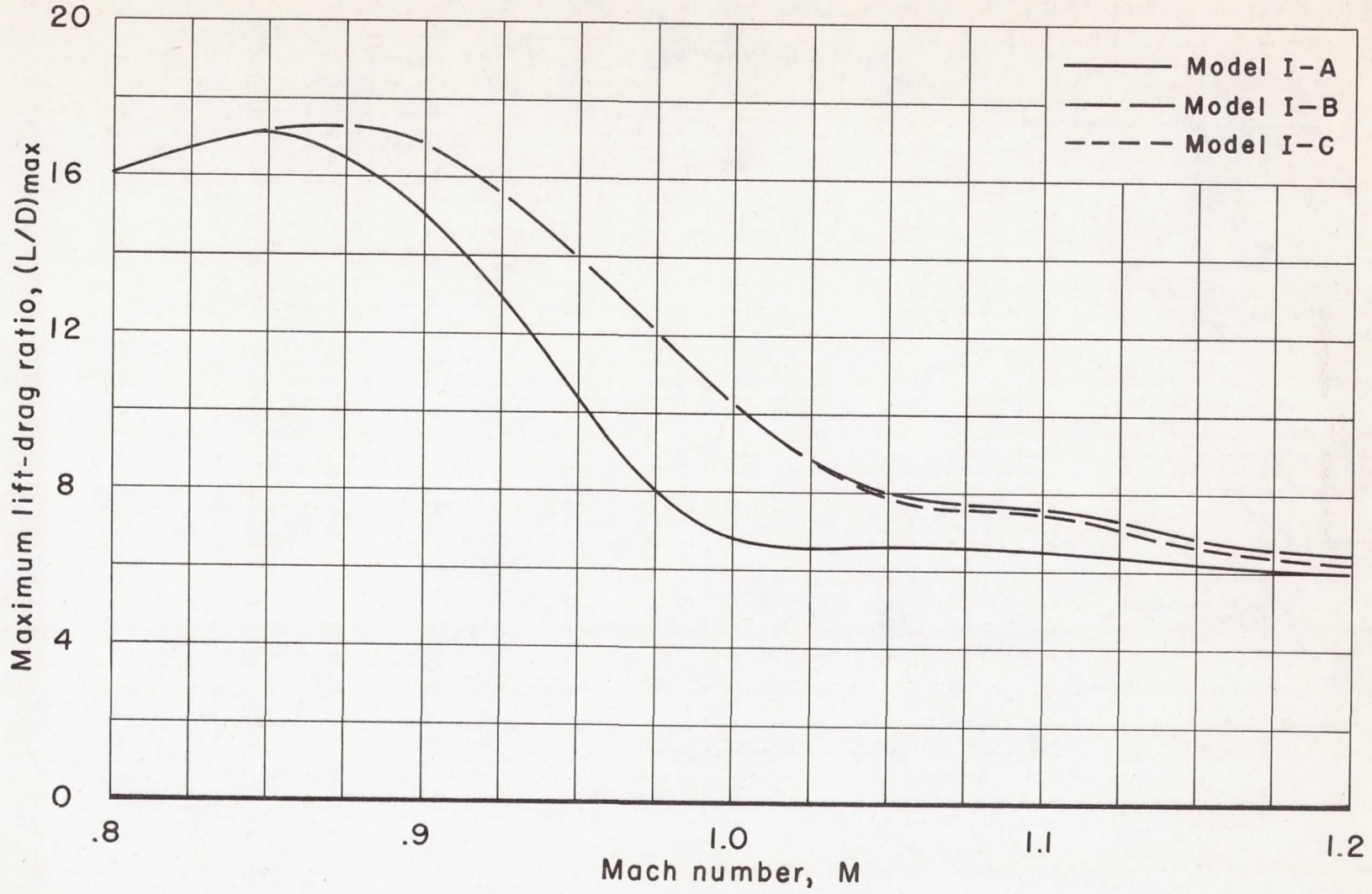

Figure 13.- The variation of maximum lift-drag ratio with Mach number for the models of series I.

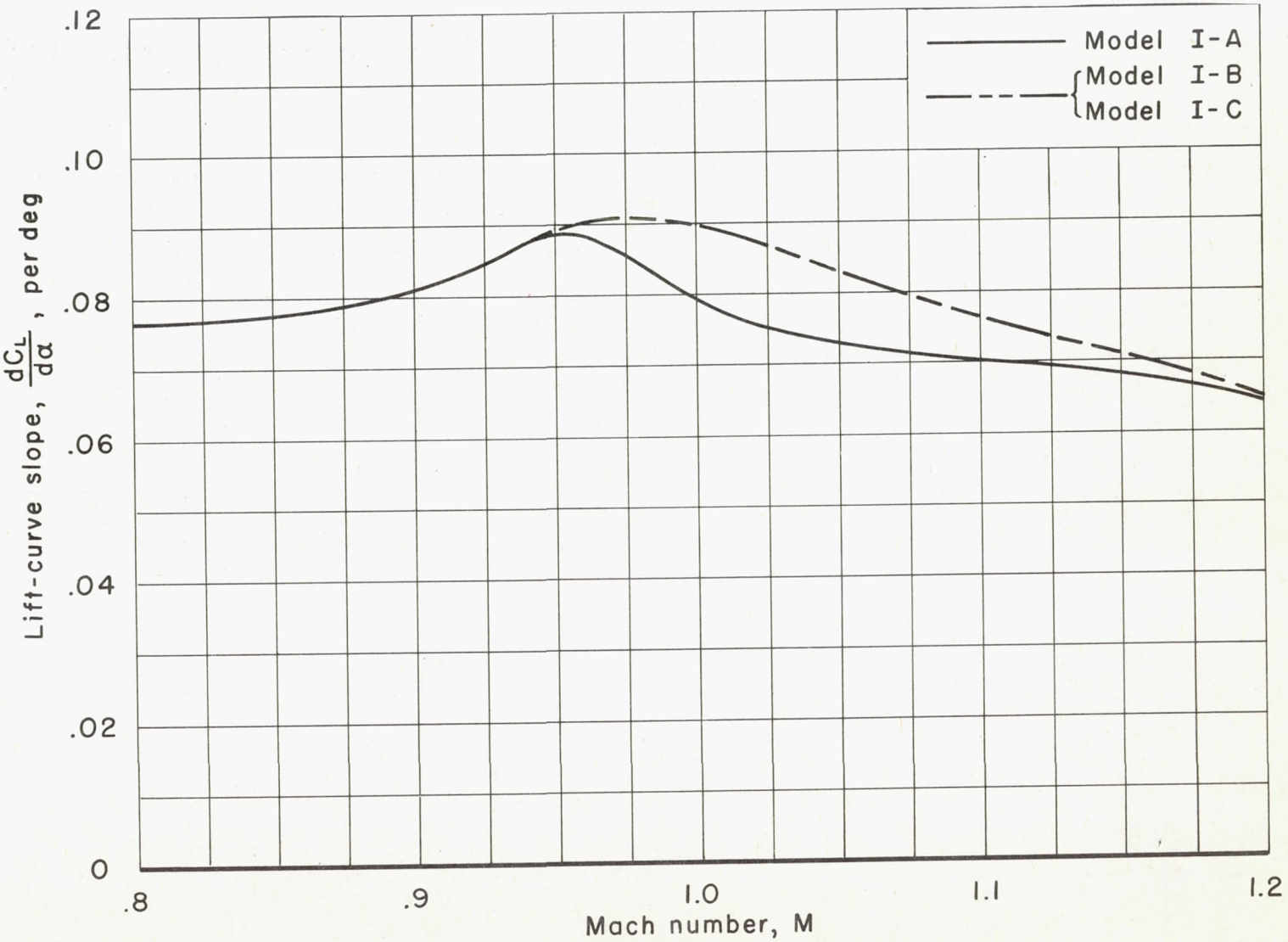

Figure 14.- The variation of lift-curve slope with Mach number for the models of series I.

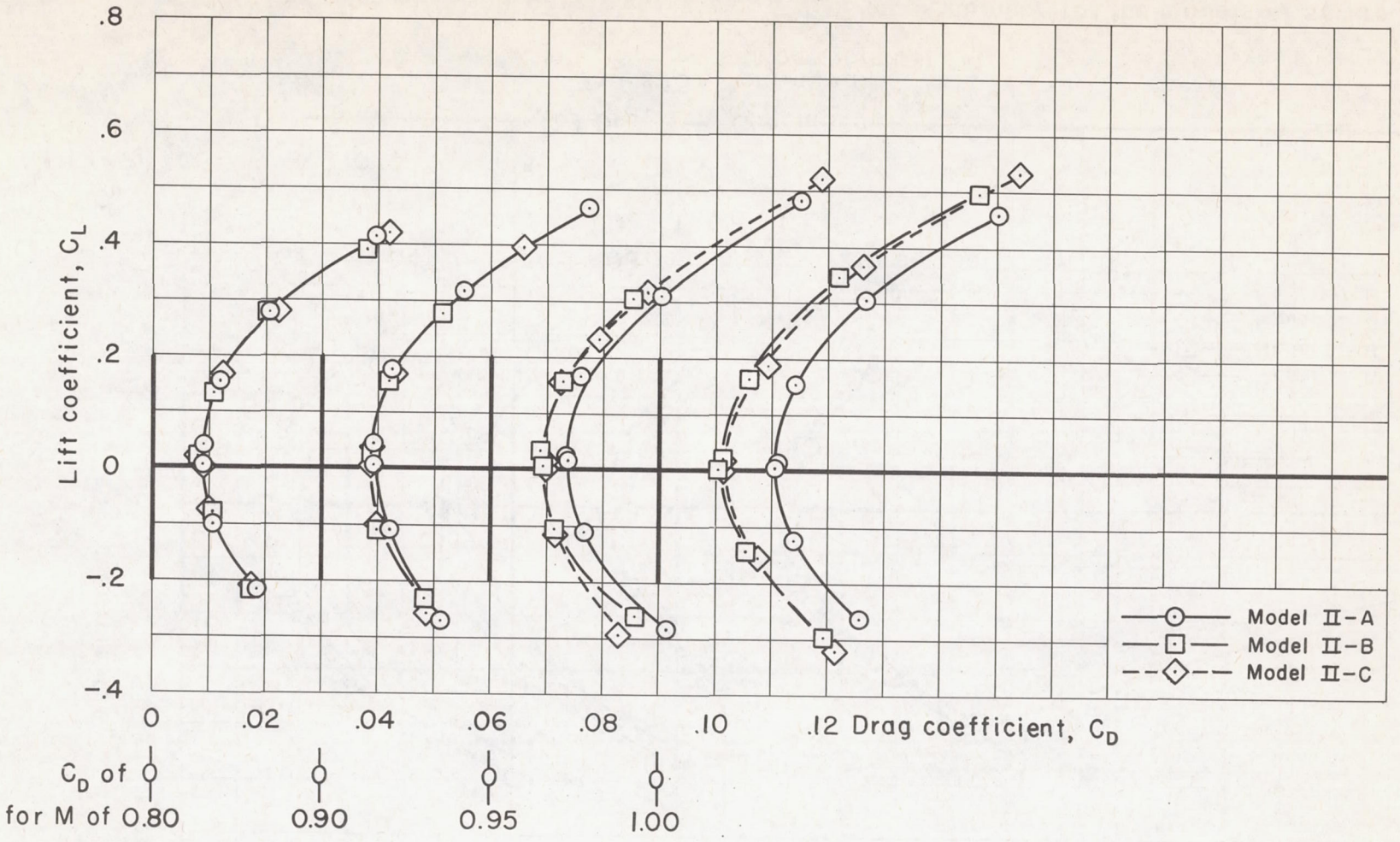

(a) Drag.

Figure 15.- Drag, lift, and pitching-moment characteristics of the models of series II.

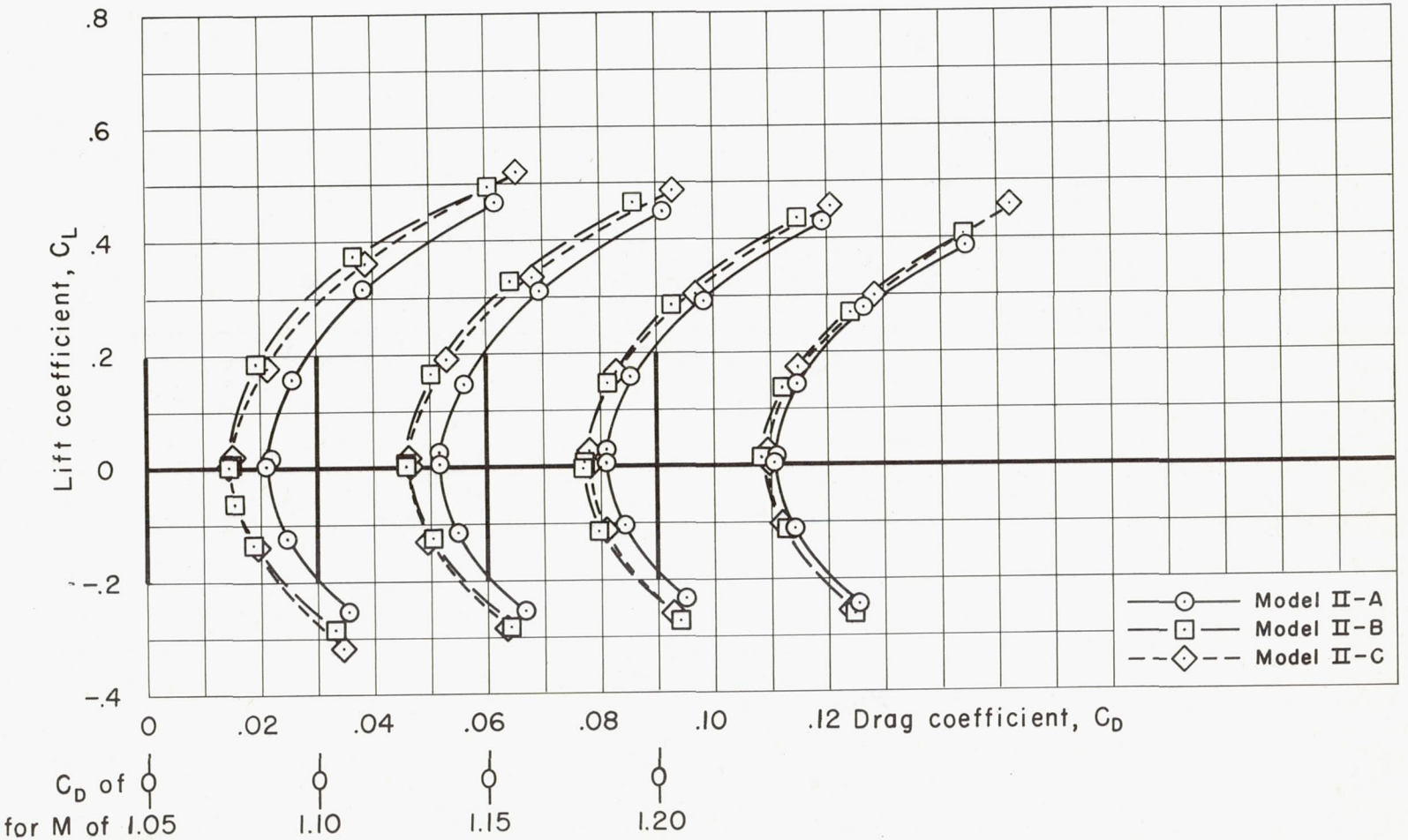

(a) Drag — Concluded.

Figure 15.- Continued.

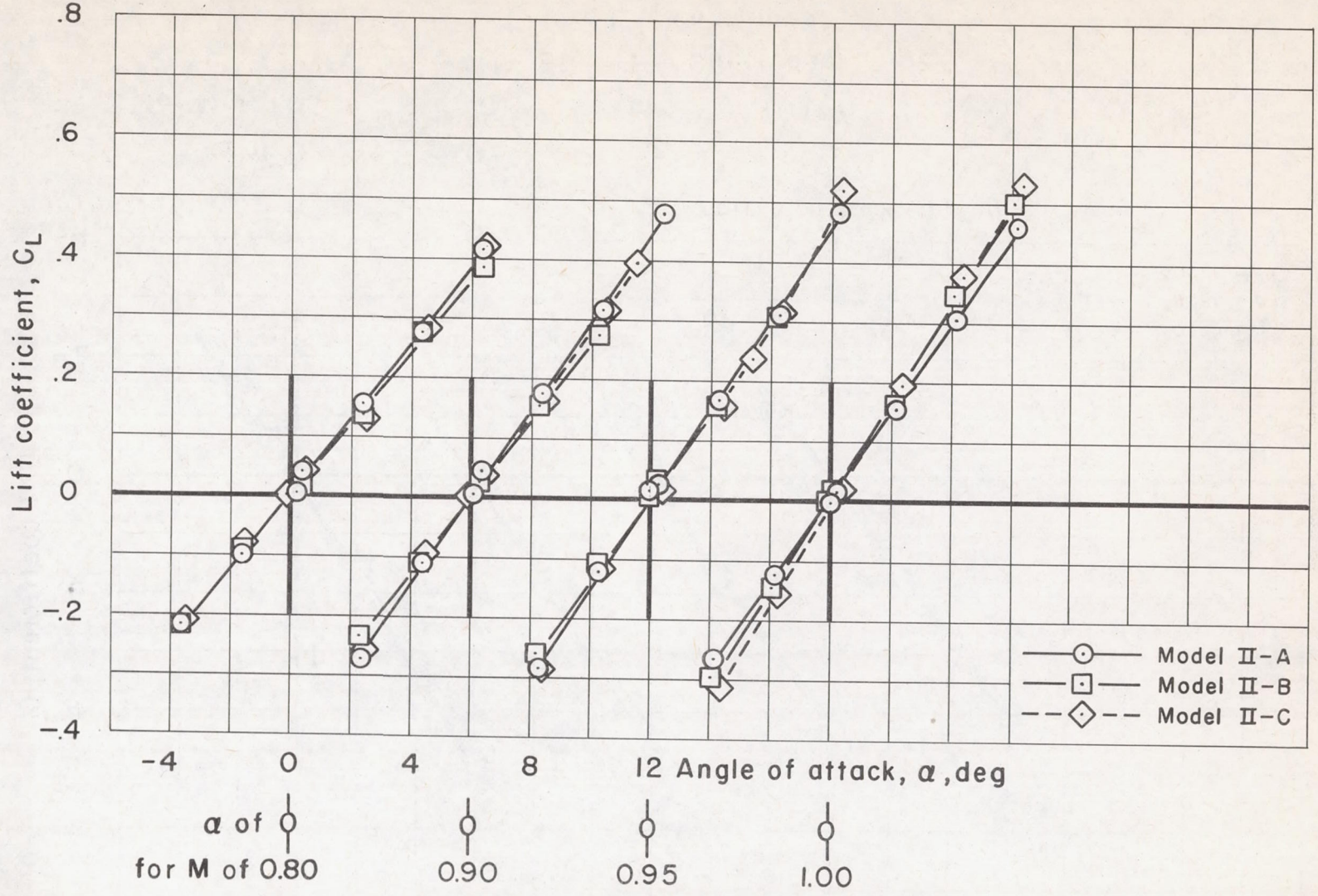

(b) Lift.

Figure 15.- Continued.

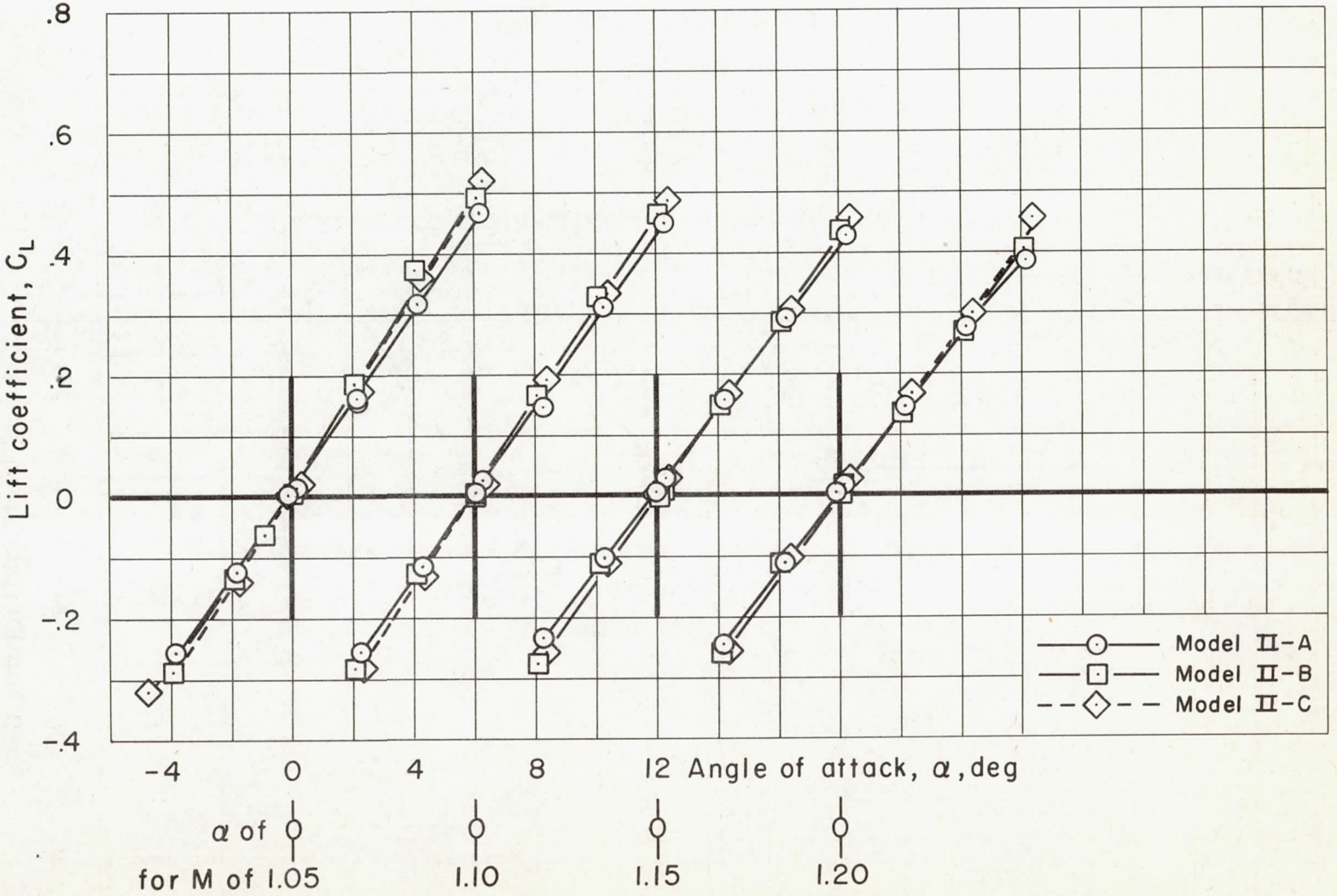

(b) Lift — Concluded.

Figure 15.- Continued.

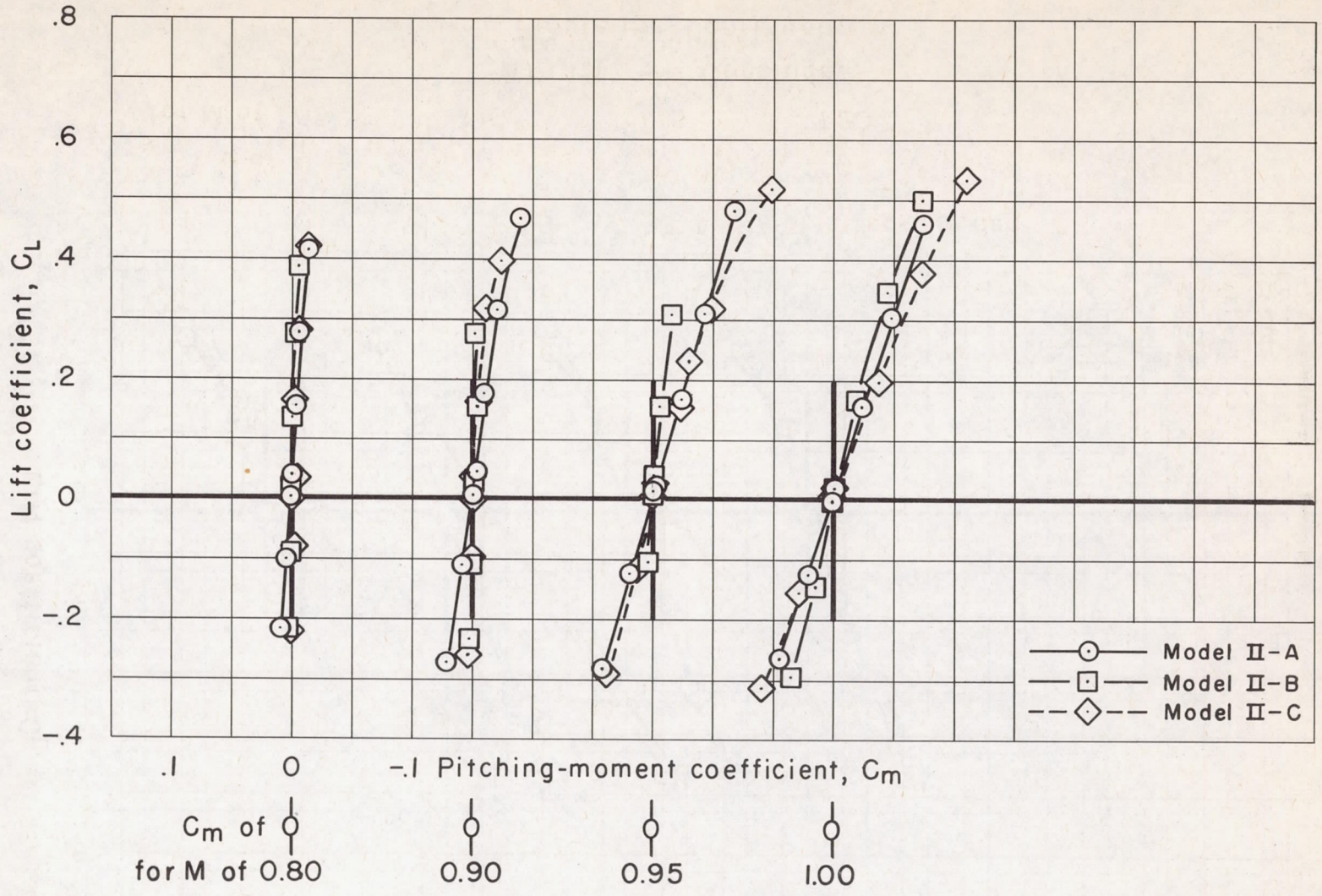

(c) Moment.

Figure 15.- Continued.

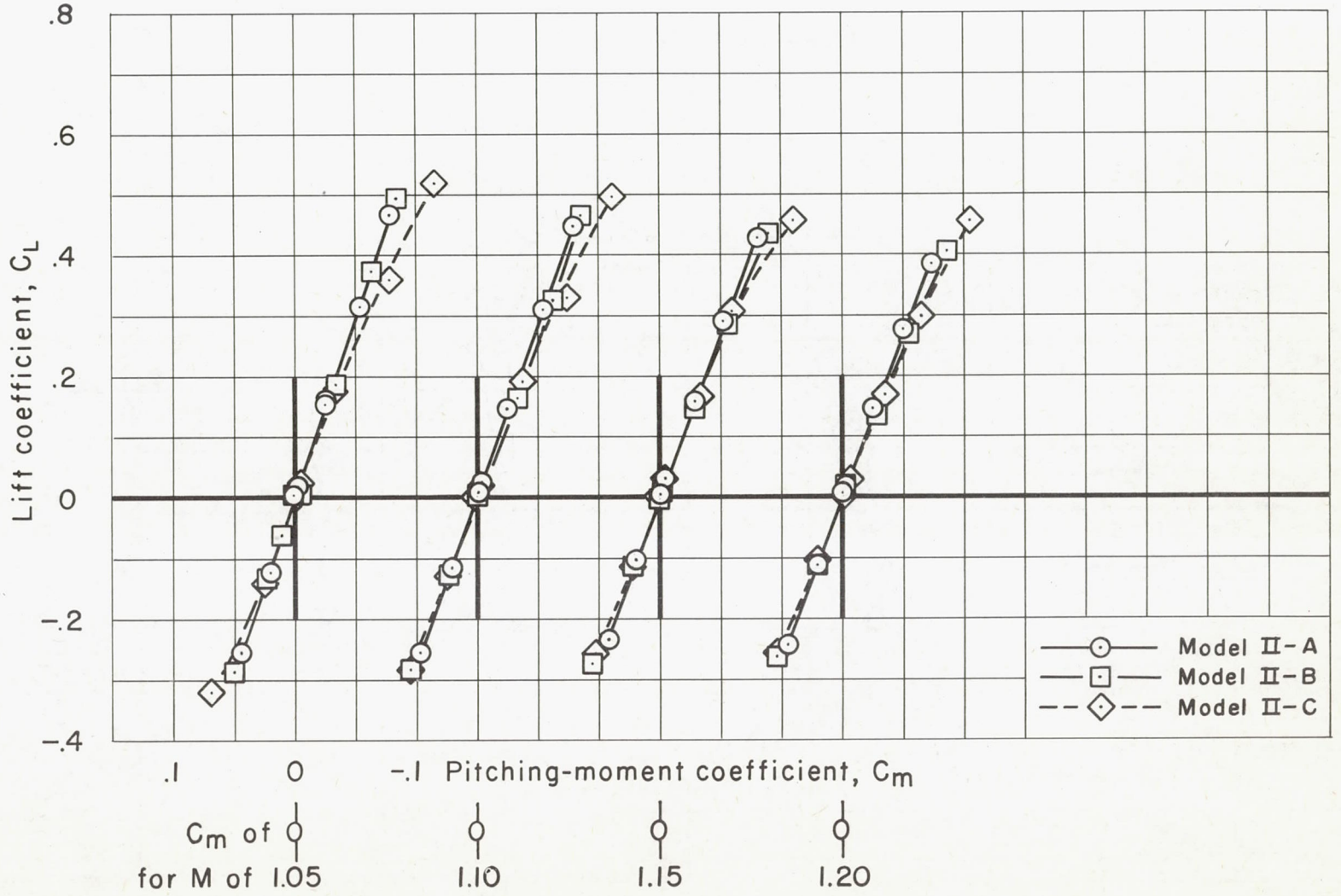

(c) Moment — Concluded.

Figure 15.- Concluded.

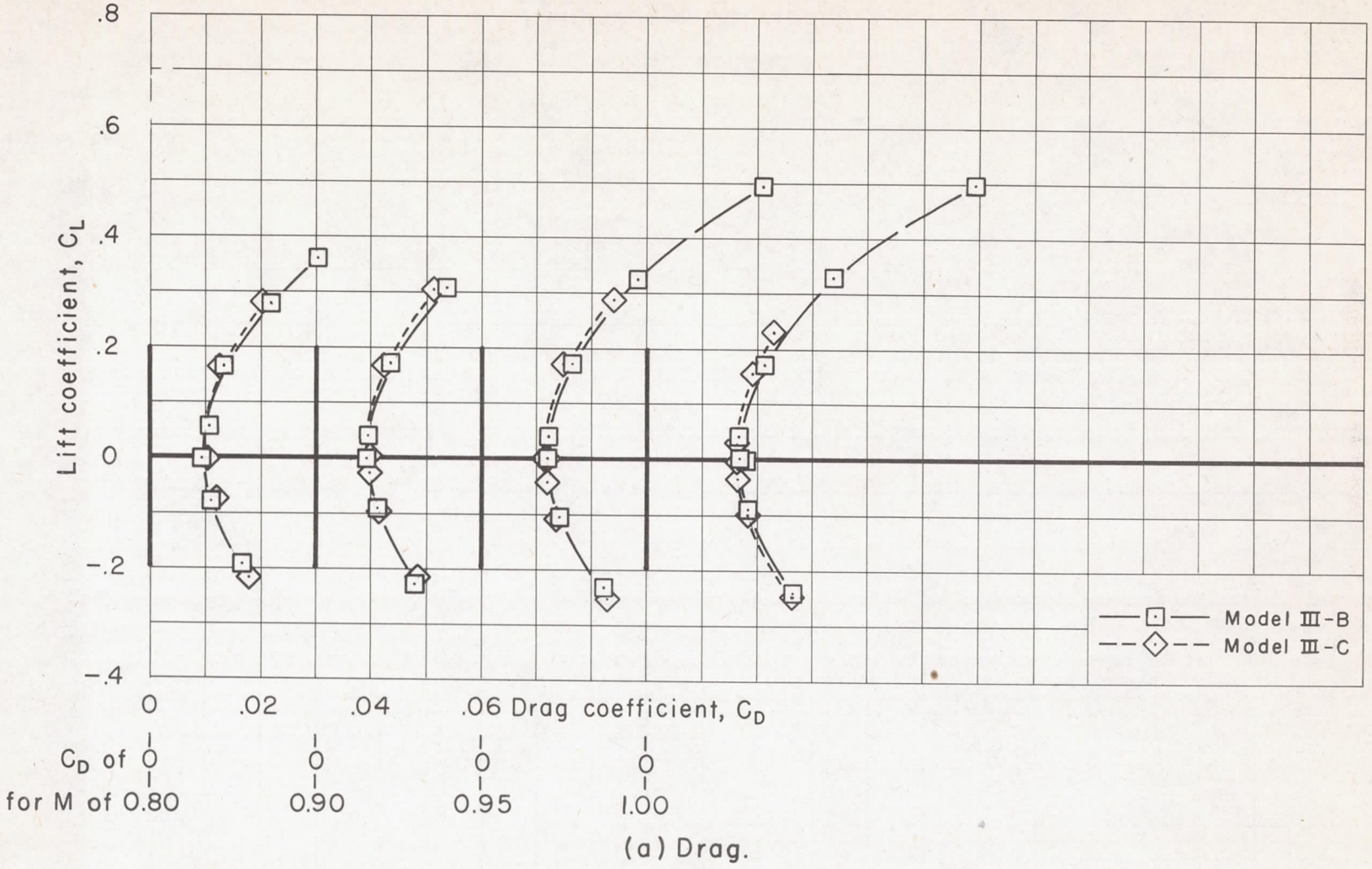

(a) Drag.

Figure 16.- Drag, lift, and pitching-moment characteristics of the models of series III.

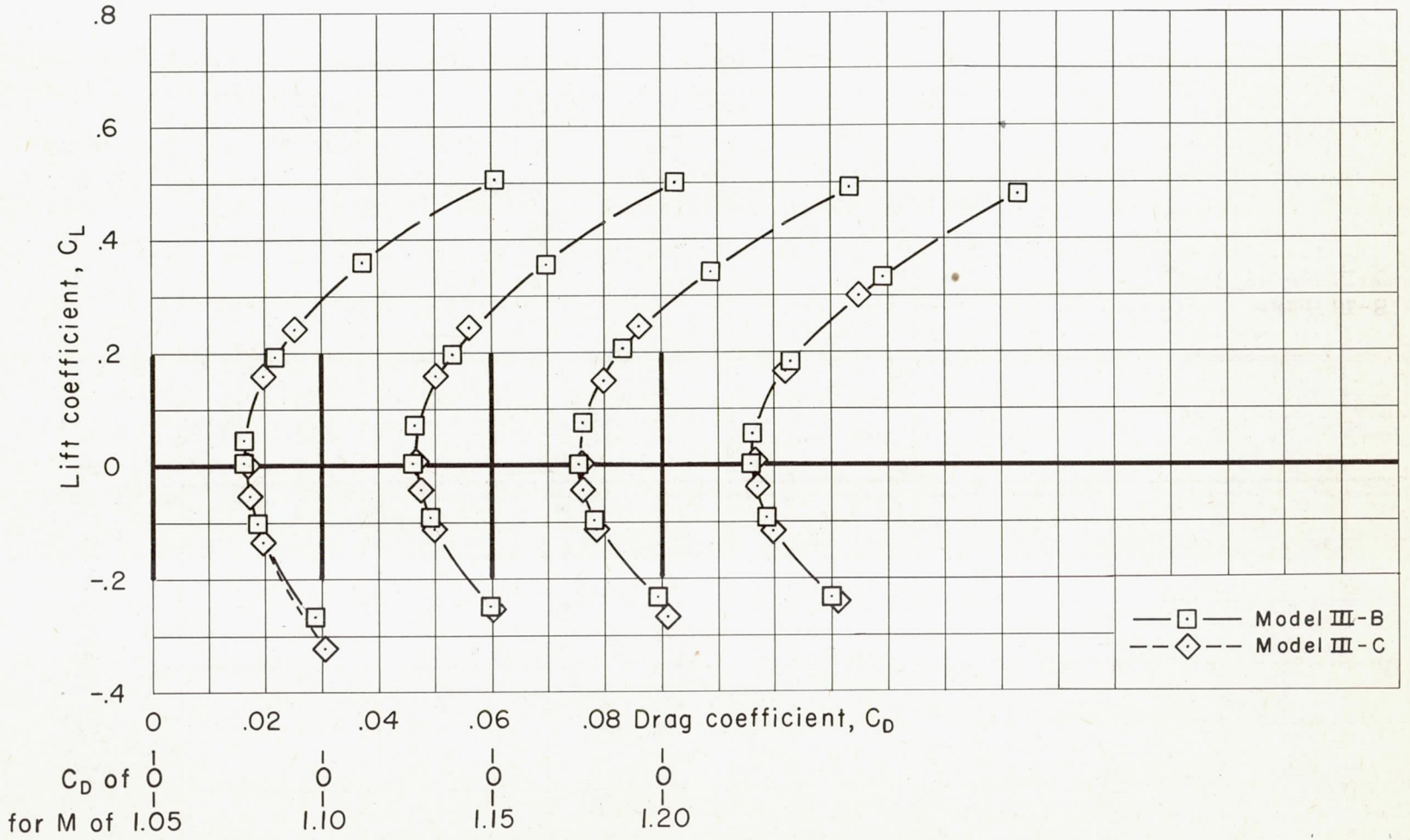

(a) Drag — Concluded.

Figure 16.- Continued.

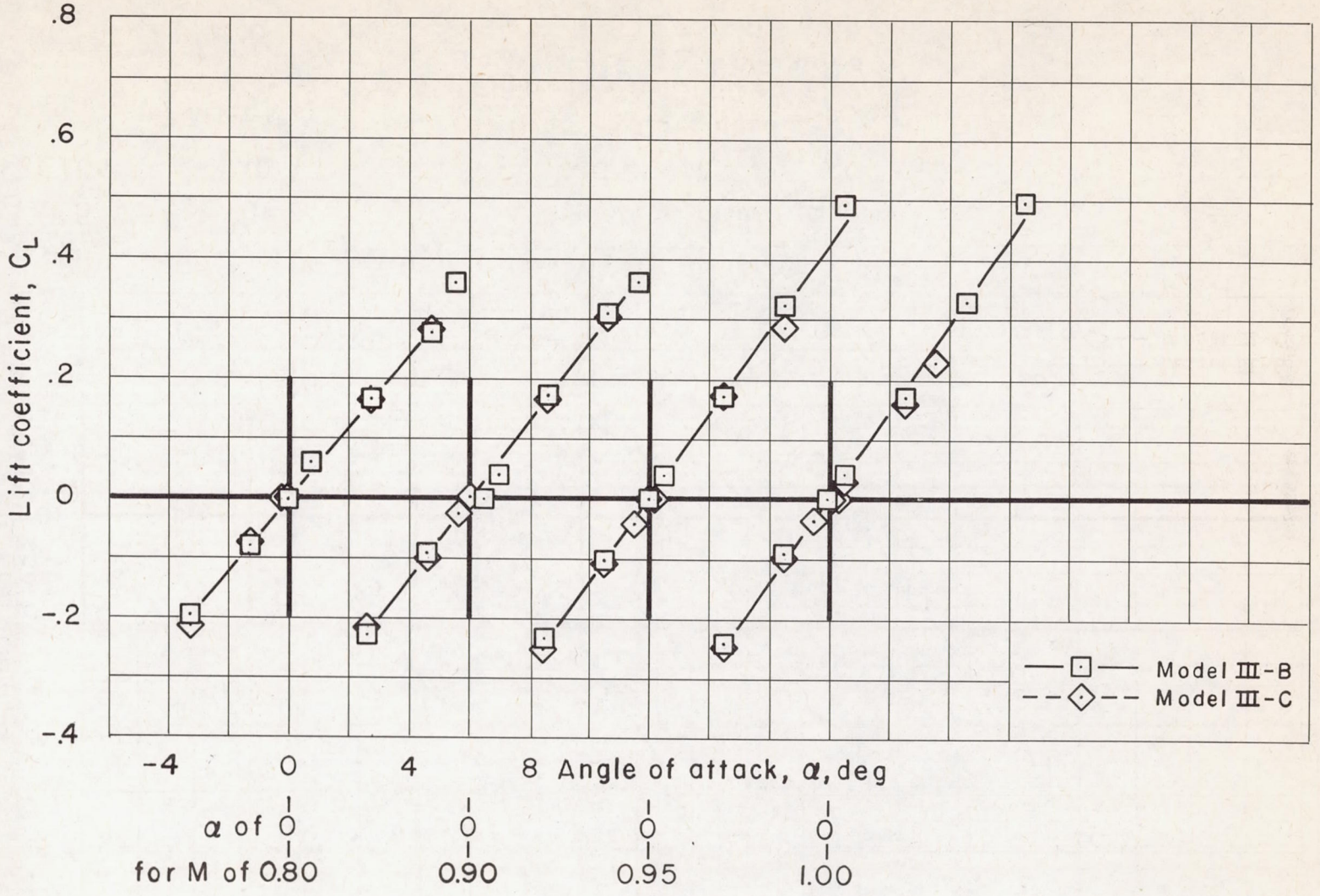

(b) Lift.

Figure 16.- Continued.

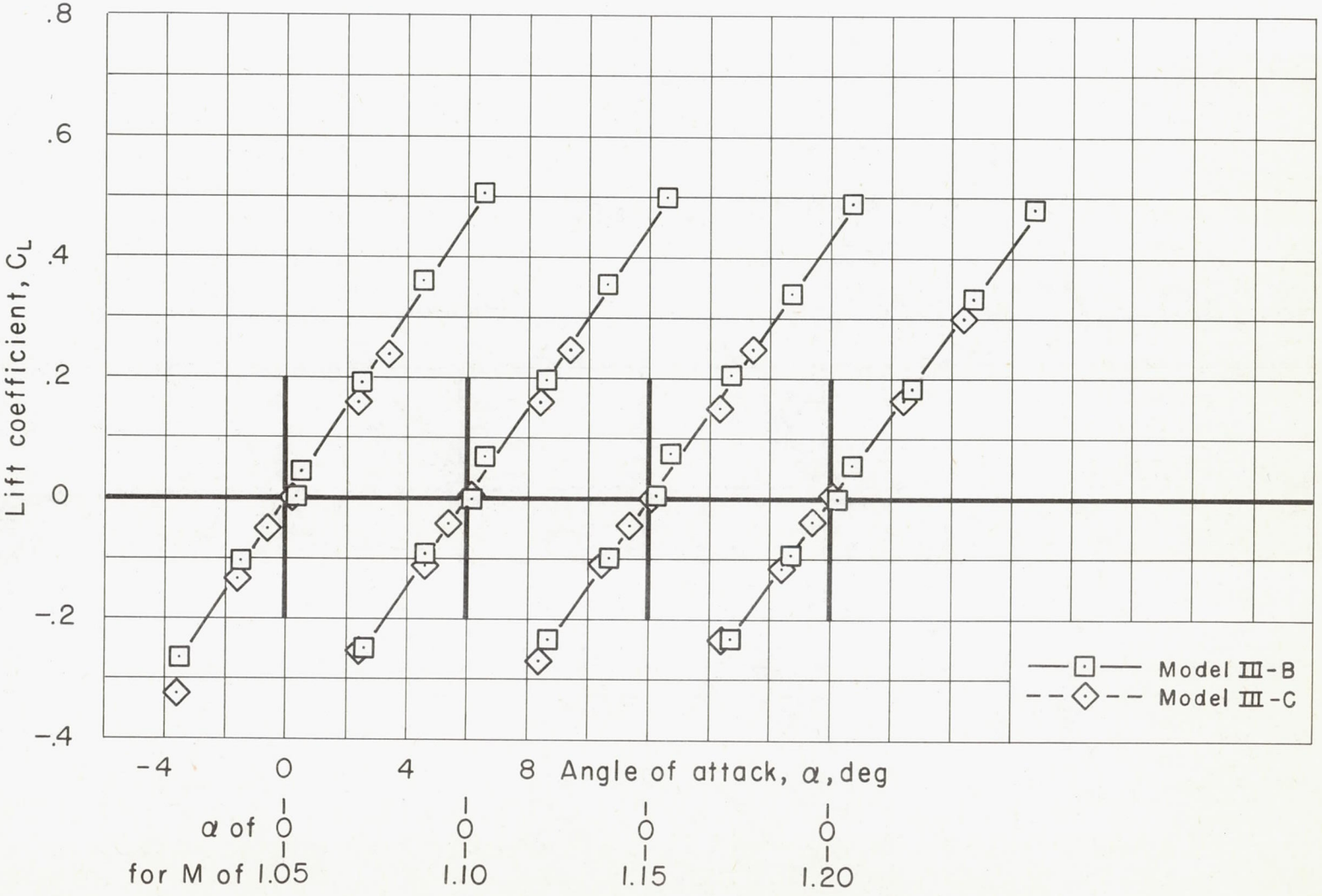

(b) Lift — Concluded.

Figure 16.- Continued.

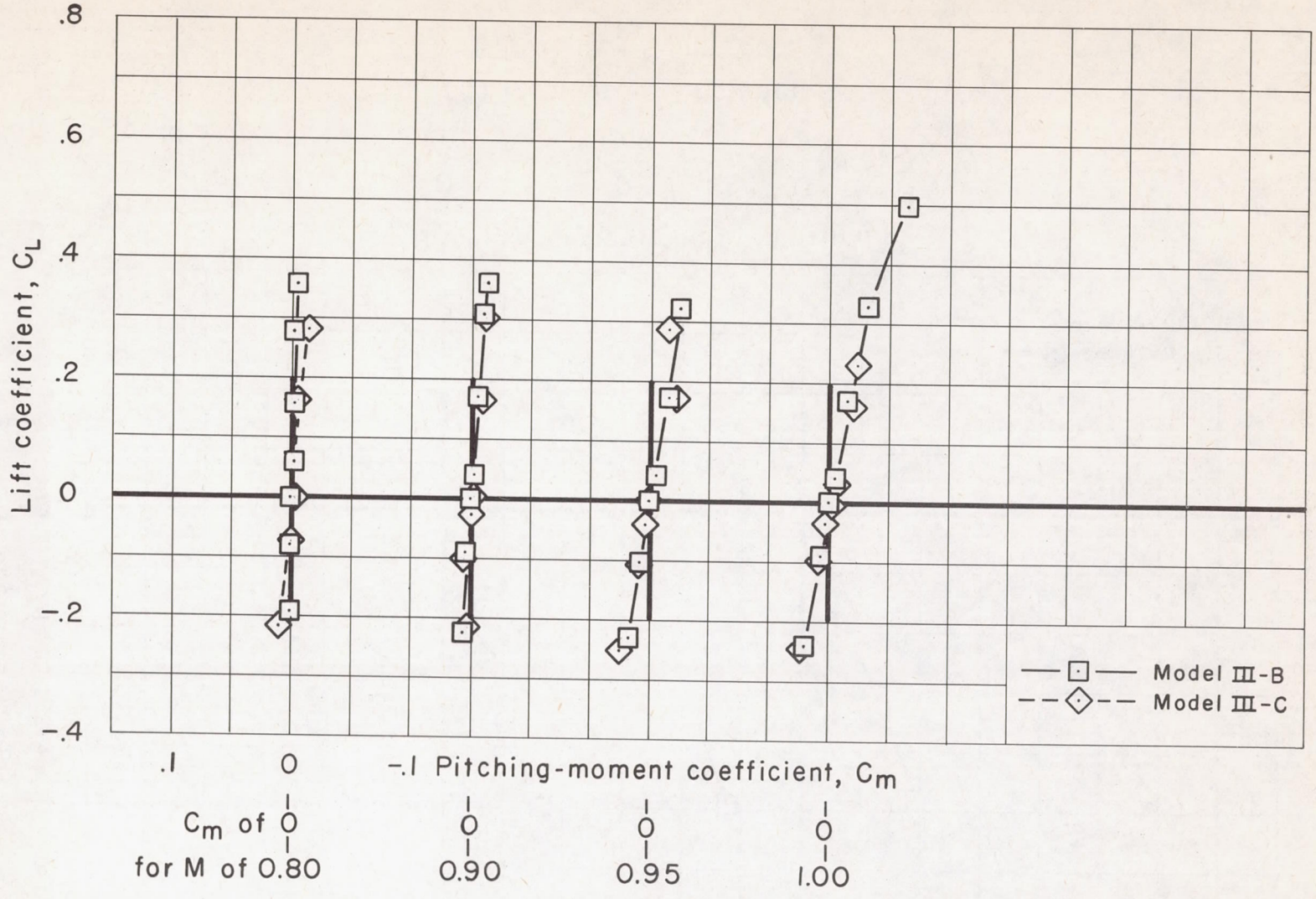

(c) Moment.

Figure 16.- Continued.

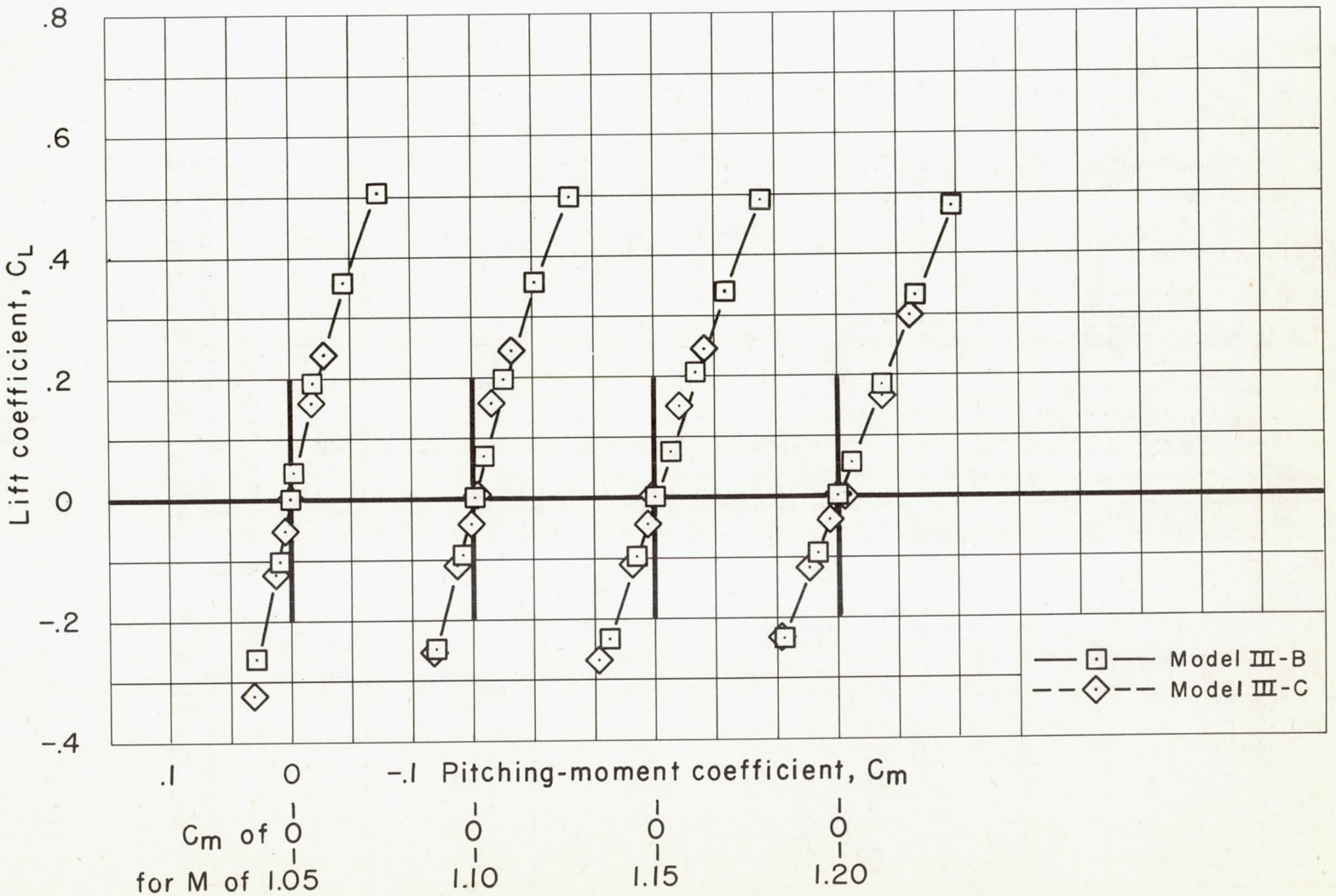

(c) Moment — Concluded.

Figure 16.- Concluded.

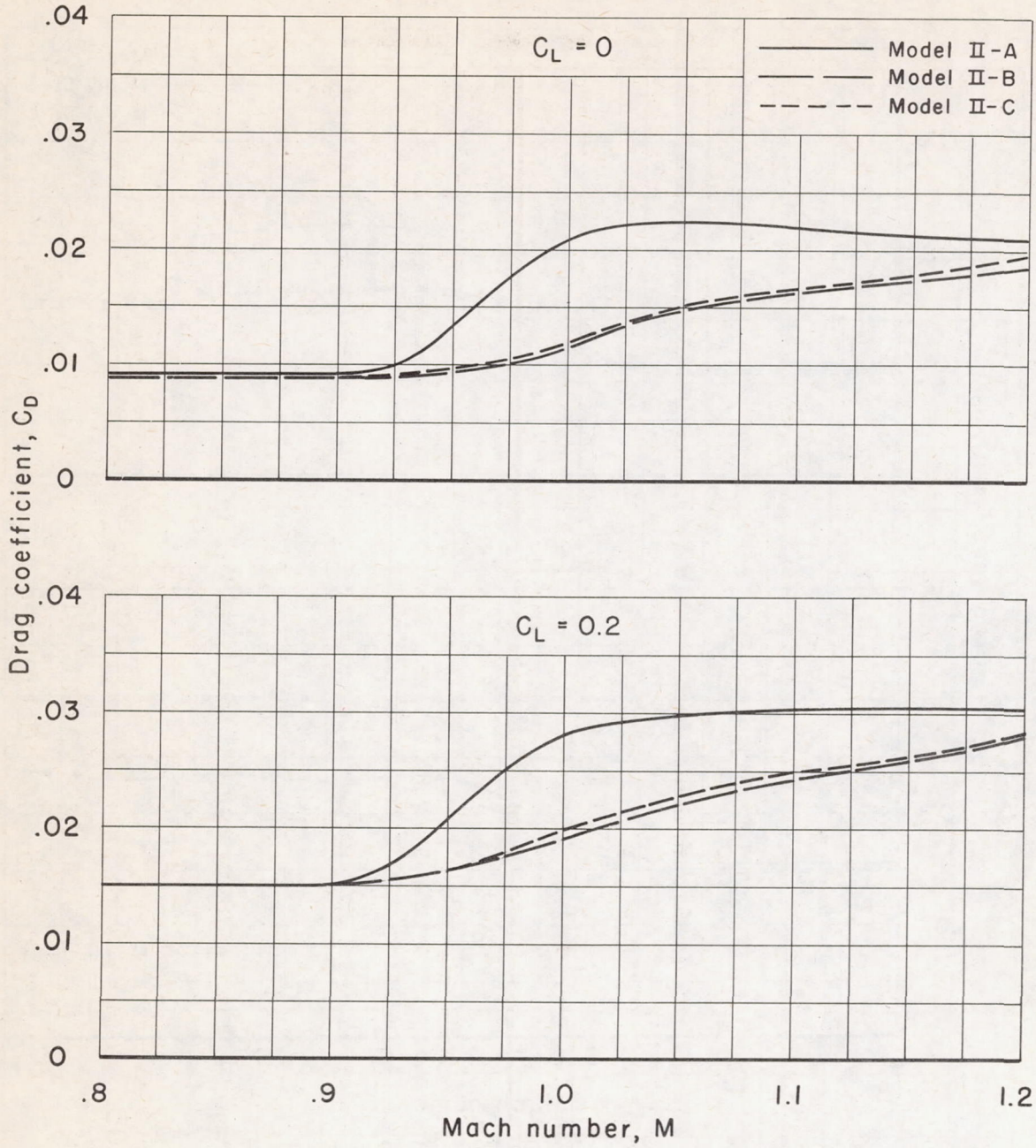

(a) Models II-A, II-B, and II-C.

Figure 17.- The variation of drag coefficient with Mach number at zero lift and C_L = 0.2 for the models of series II and series III.

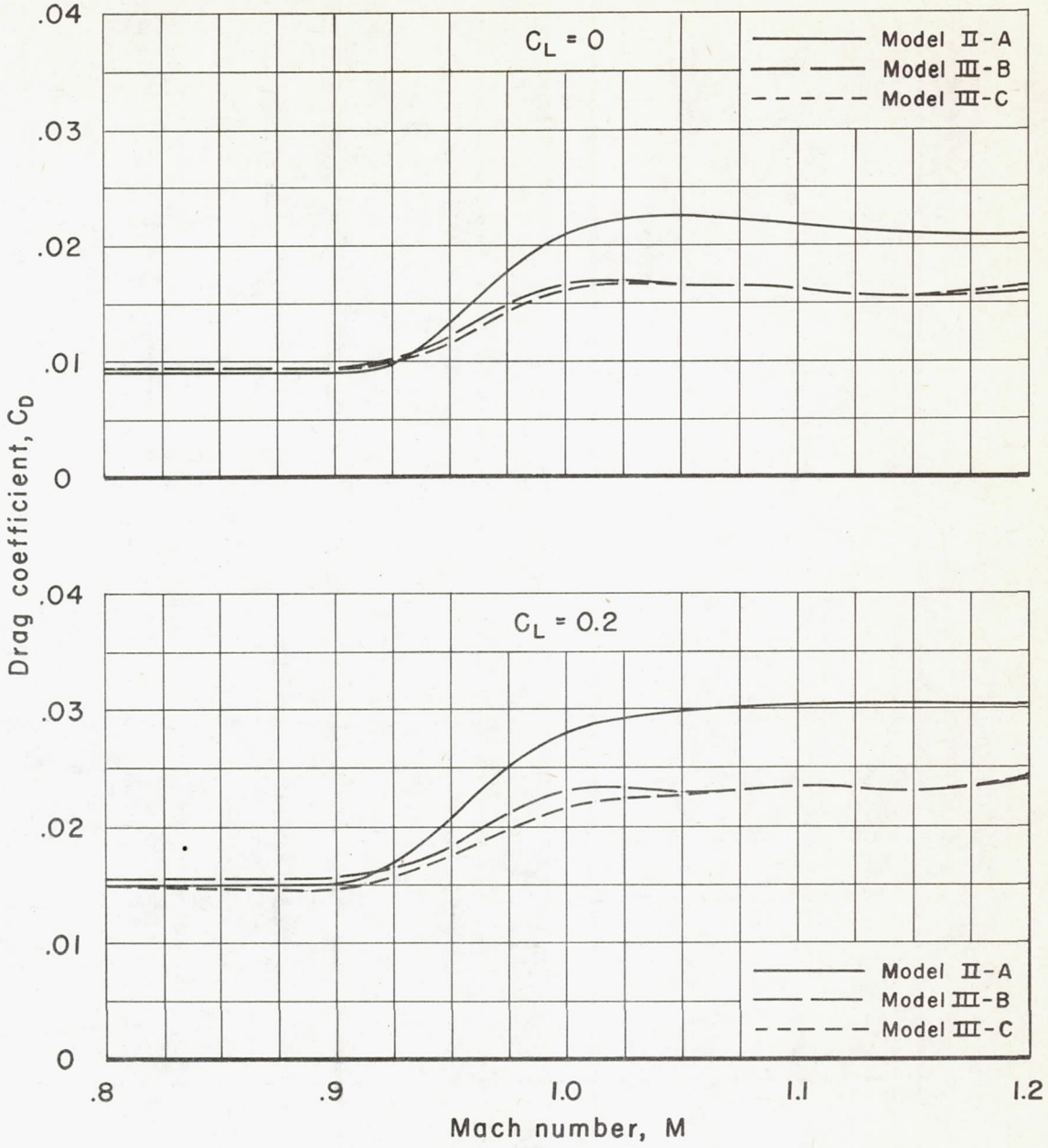

(b) Models II-A, III-B, and III-C.

Figure 17.- Concluded.

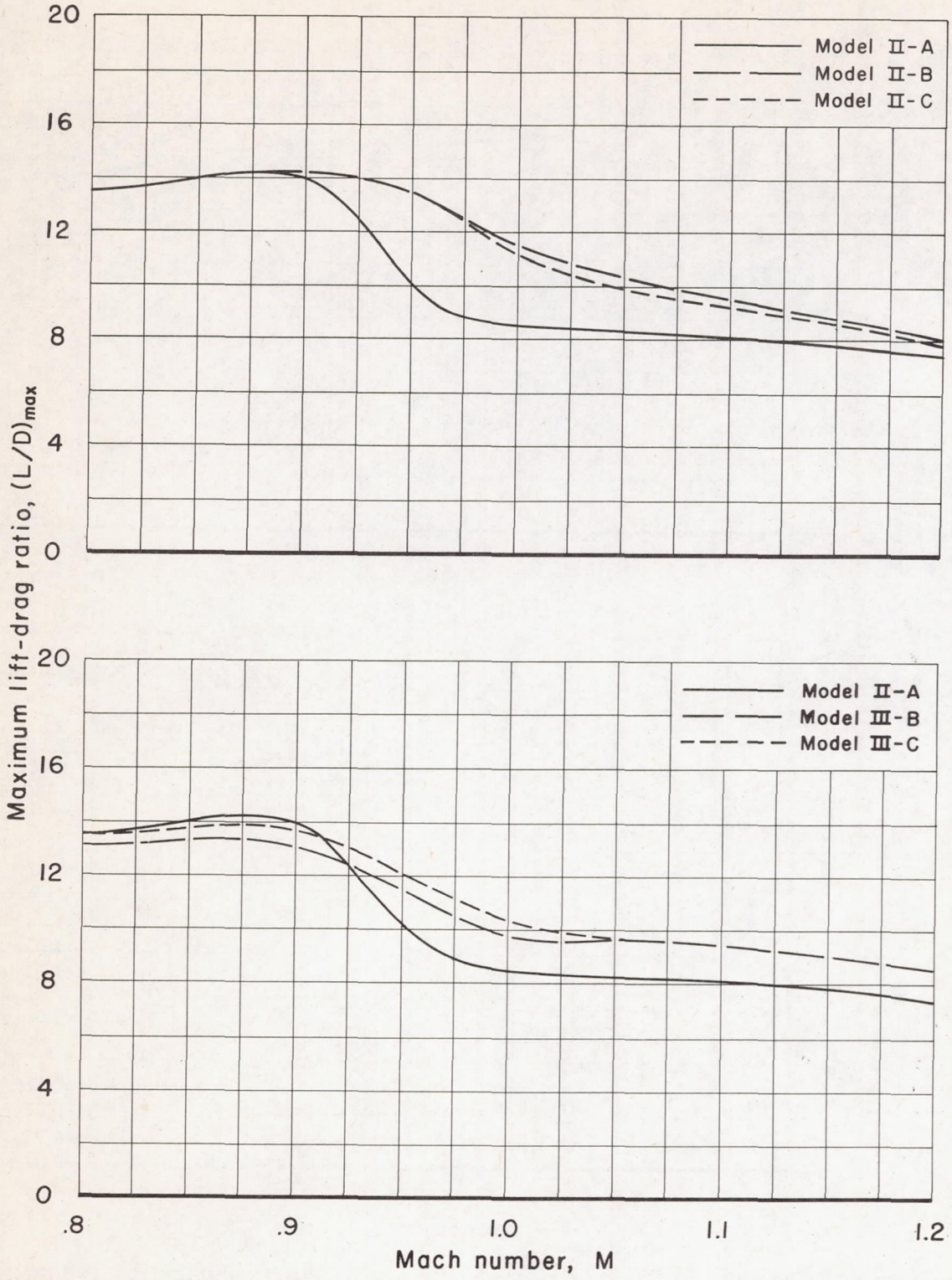

Figure 18.- The variation of maximum lift-drag ratio with Mach number for the models of series II and series III.

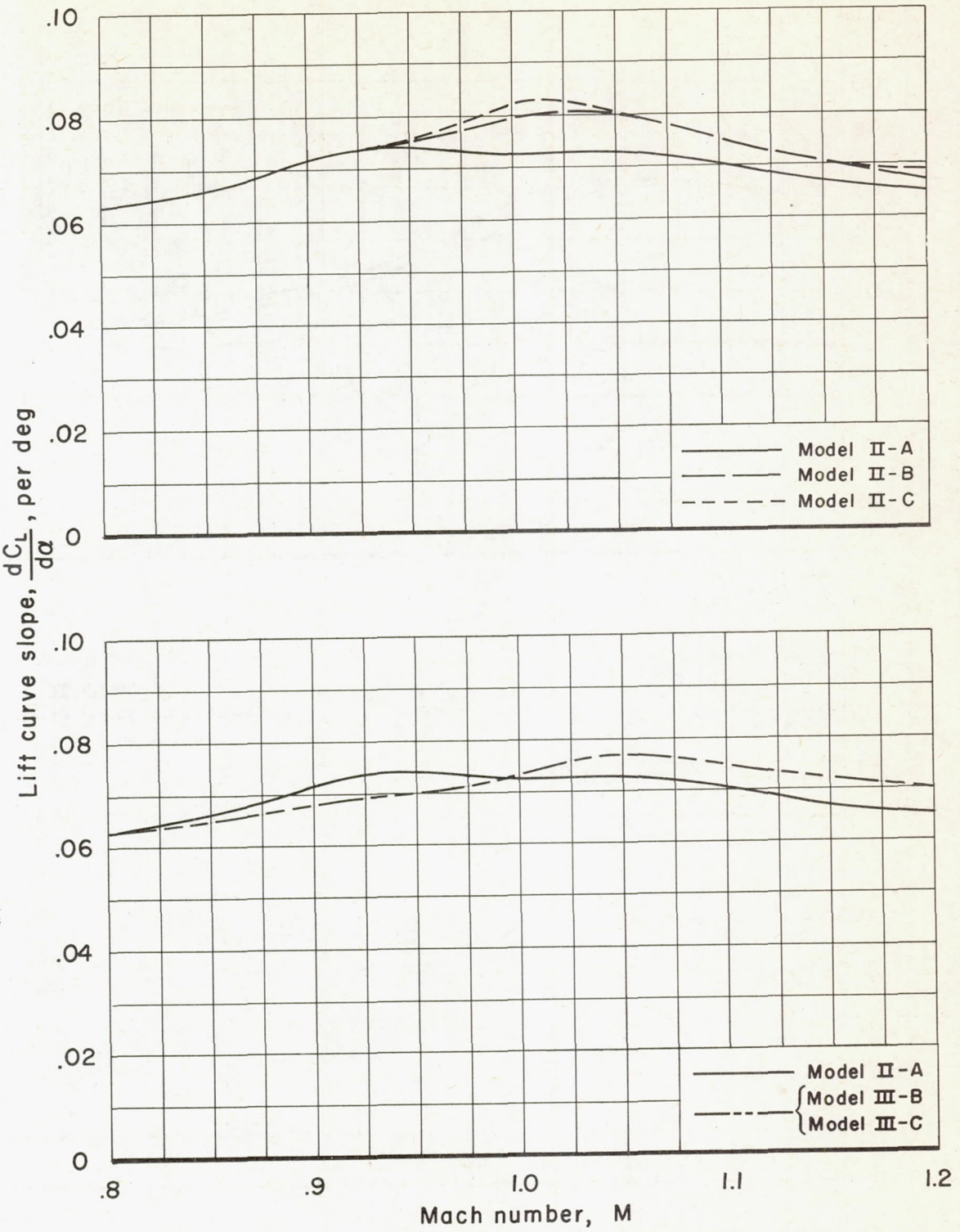

Figure 19.- The variation of lift-curve slope with Mach number for the models of series II and series III.

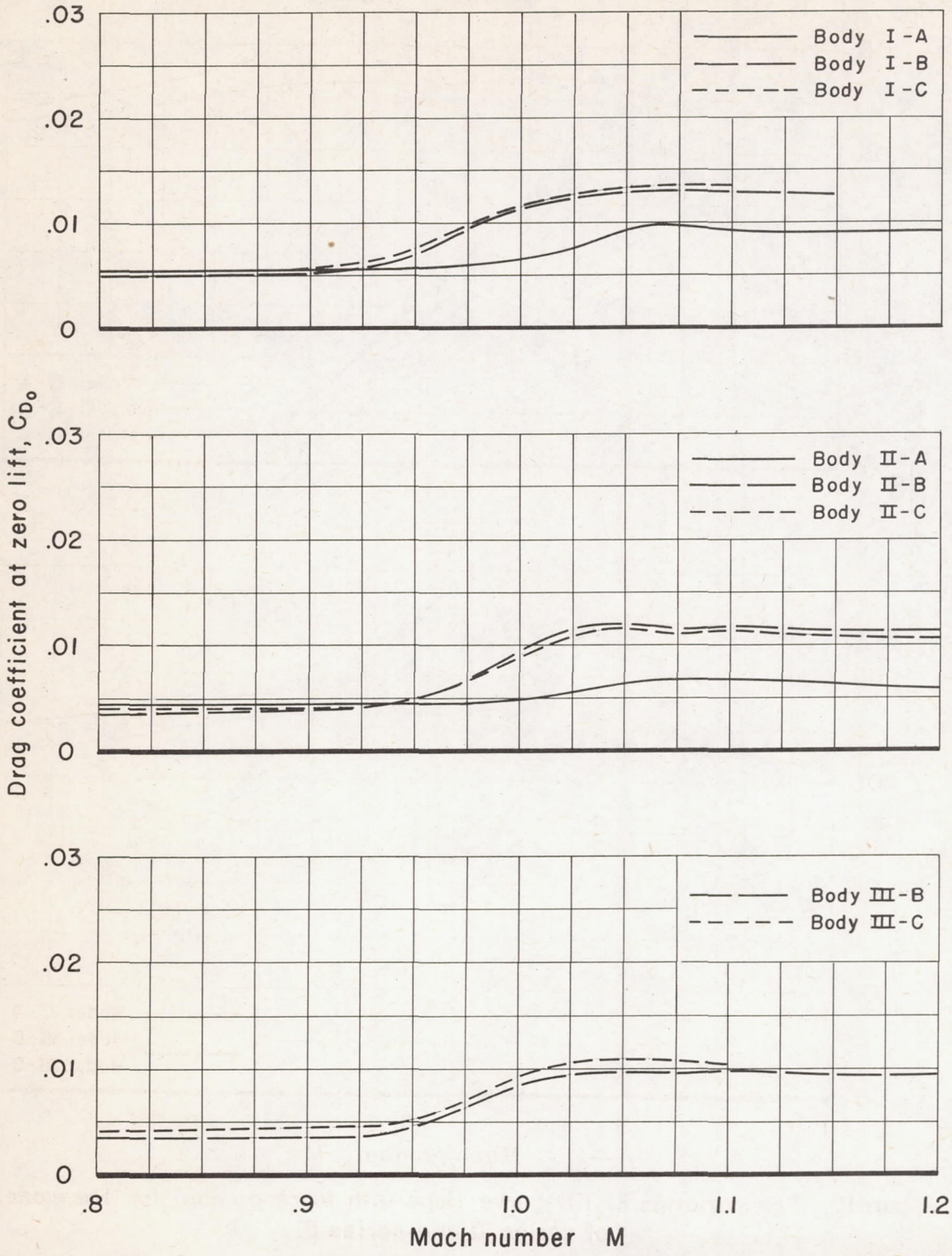

Figure 20.- The variation of zero-lift drag coefficient (based on the respective wing areas) with Mach number for the various bodies.

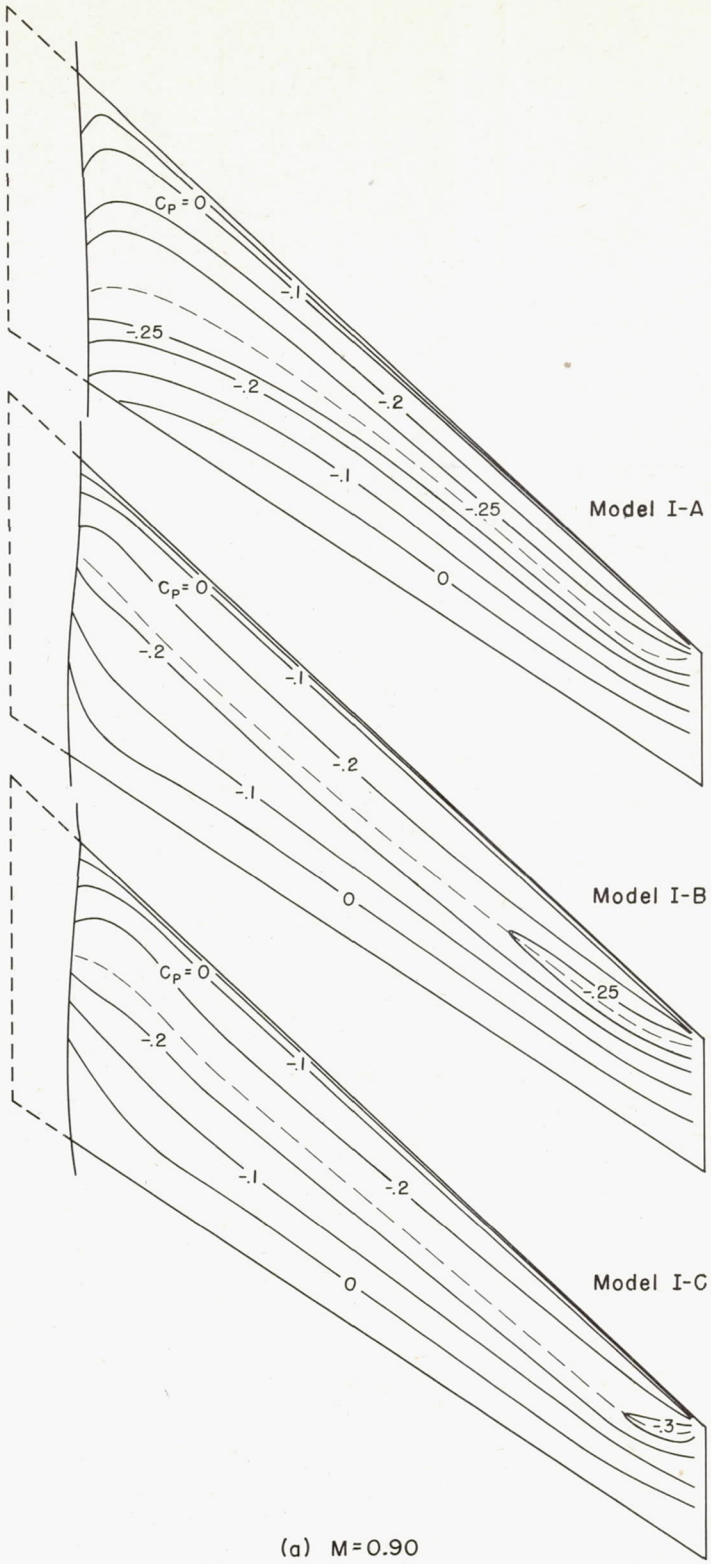

(a) M=0.90

Figure 21.- Experimental wing isobars for model series I at zero lift.

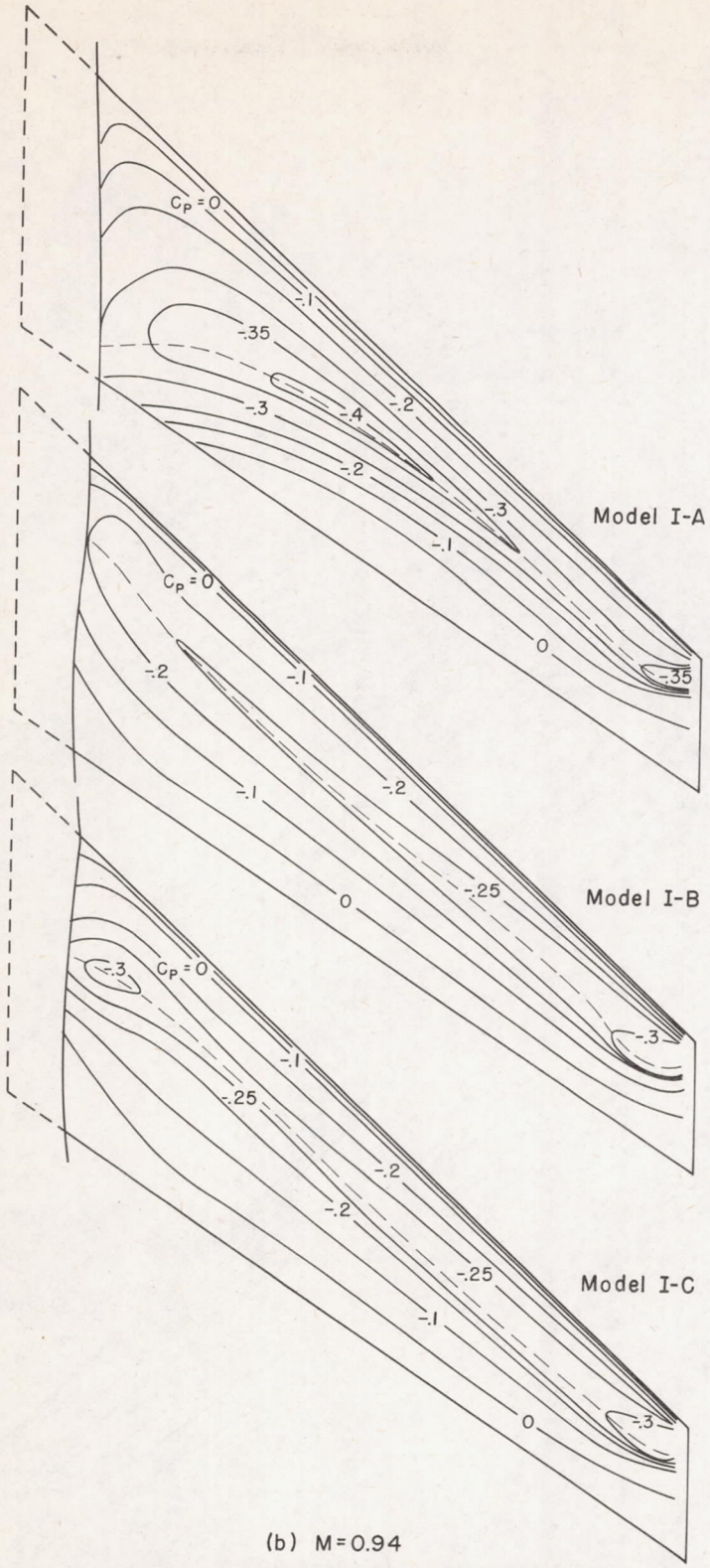

(b) M=0.94

Figure 21.- Continued.

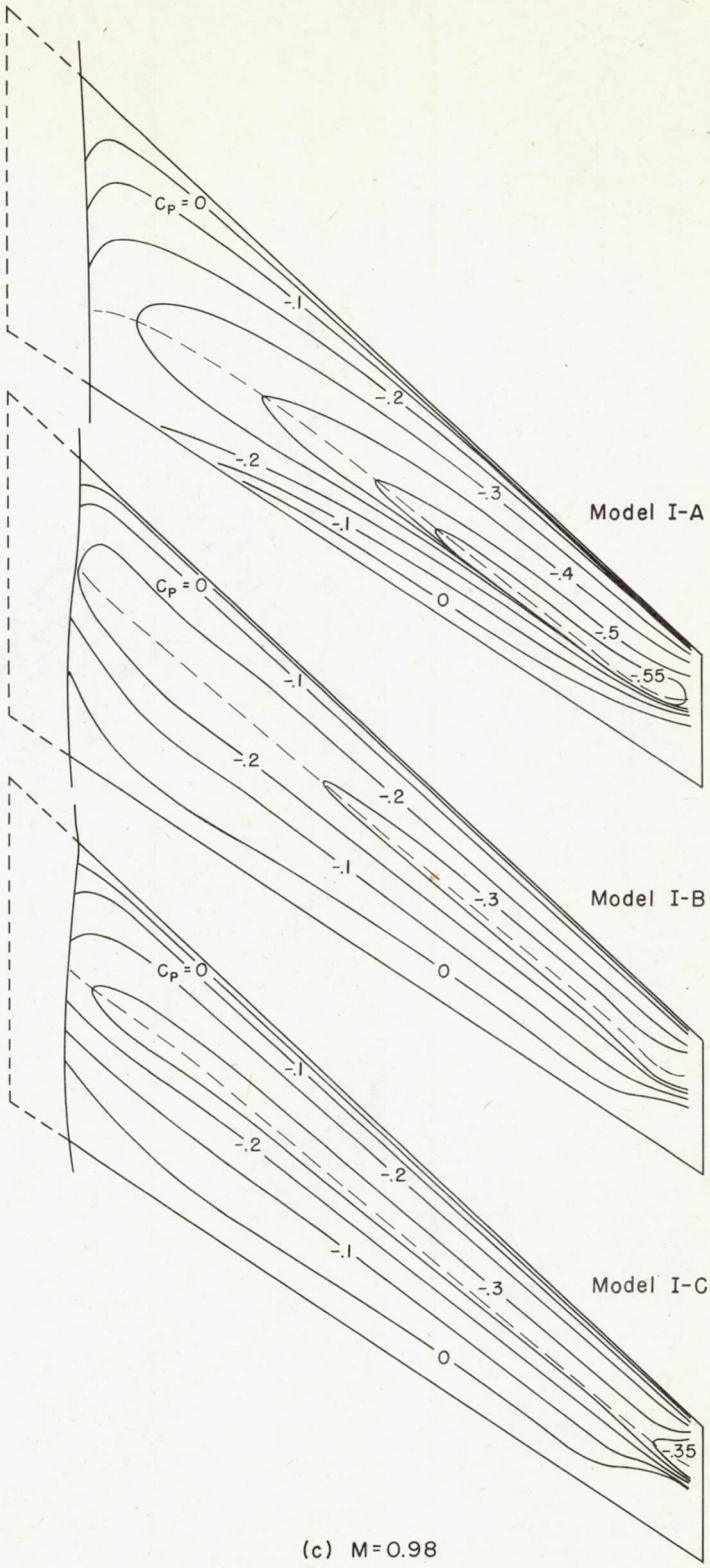

(c) M=0.98

Figure 21.- Continued.

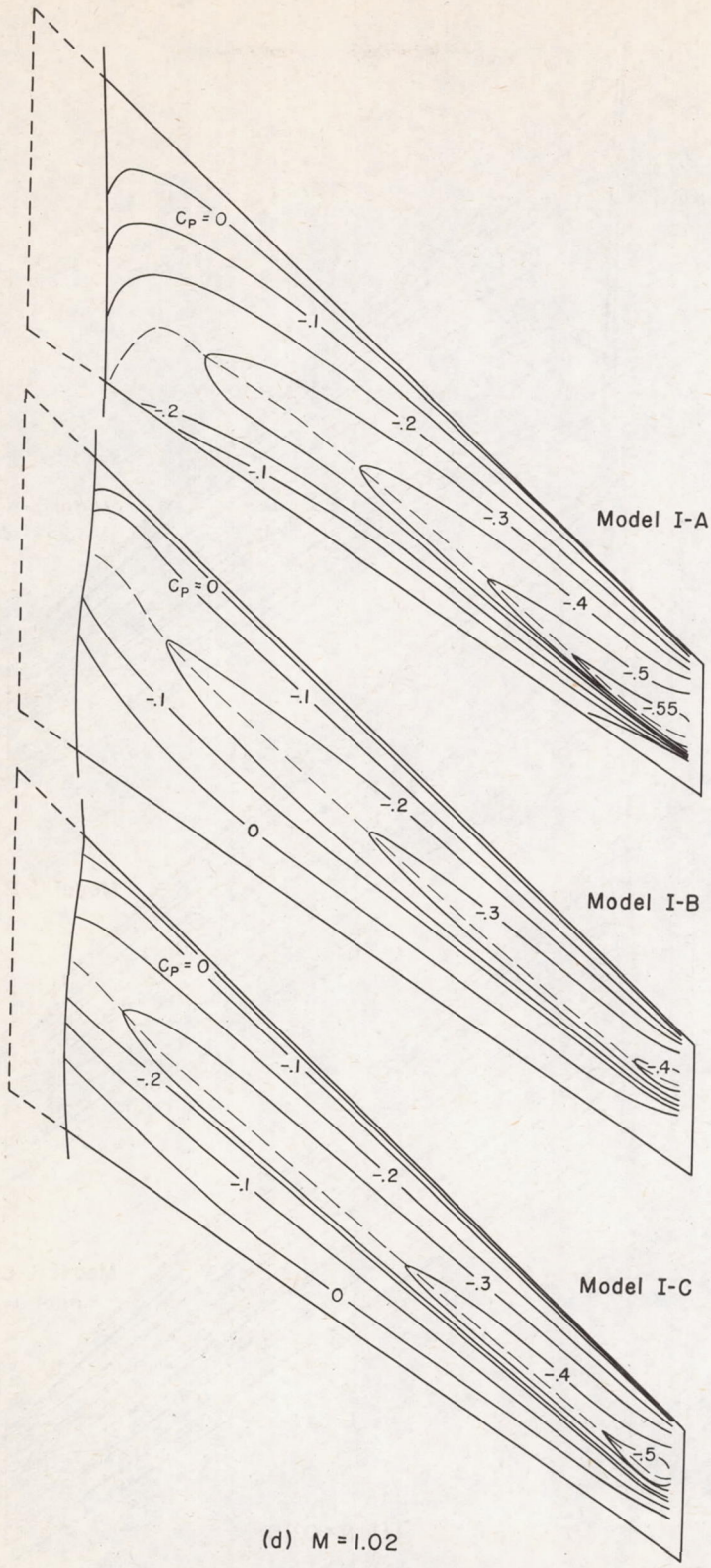

(d) M = 1.02

Figure 21.- Continued.

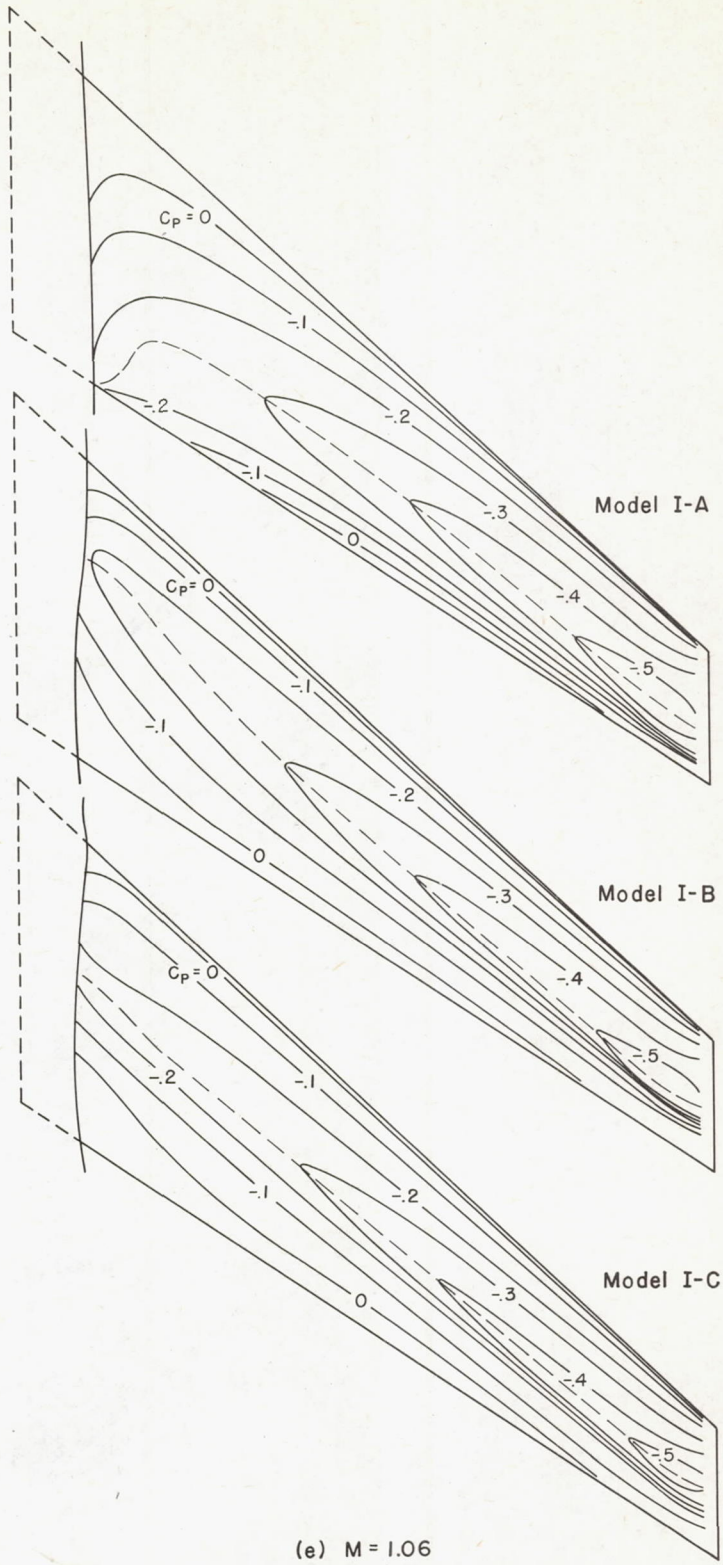

(e) M = 1.06

Figure 21.- Continued.

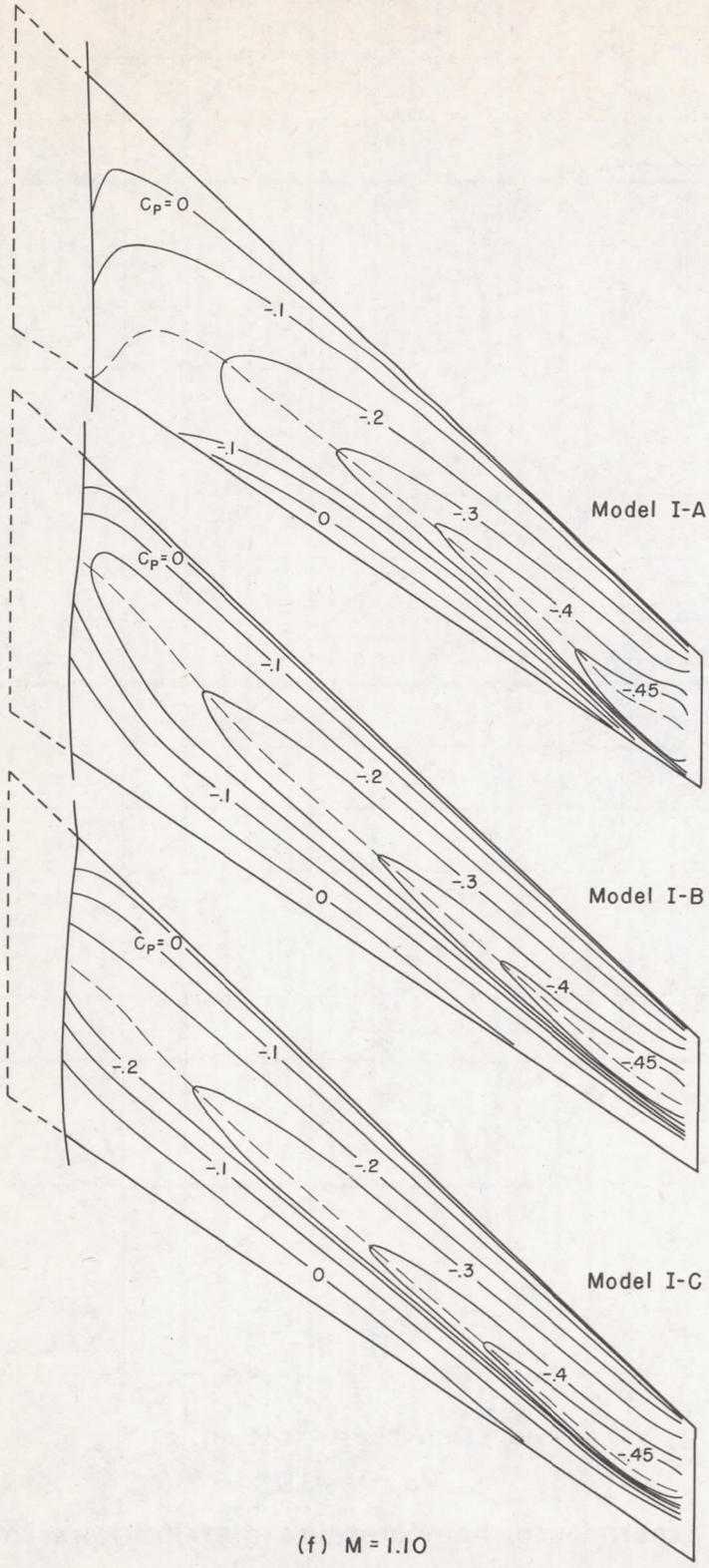

(f) M = 1.10

Figure 21.- Concluded.

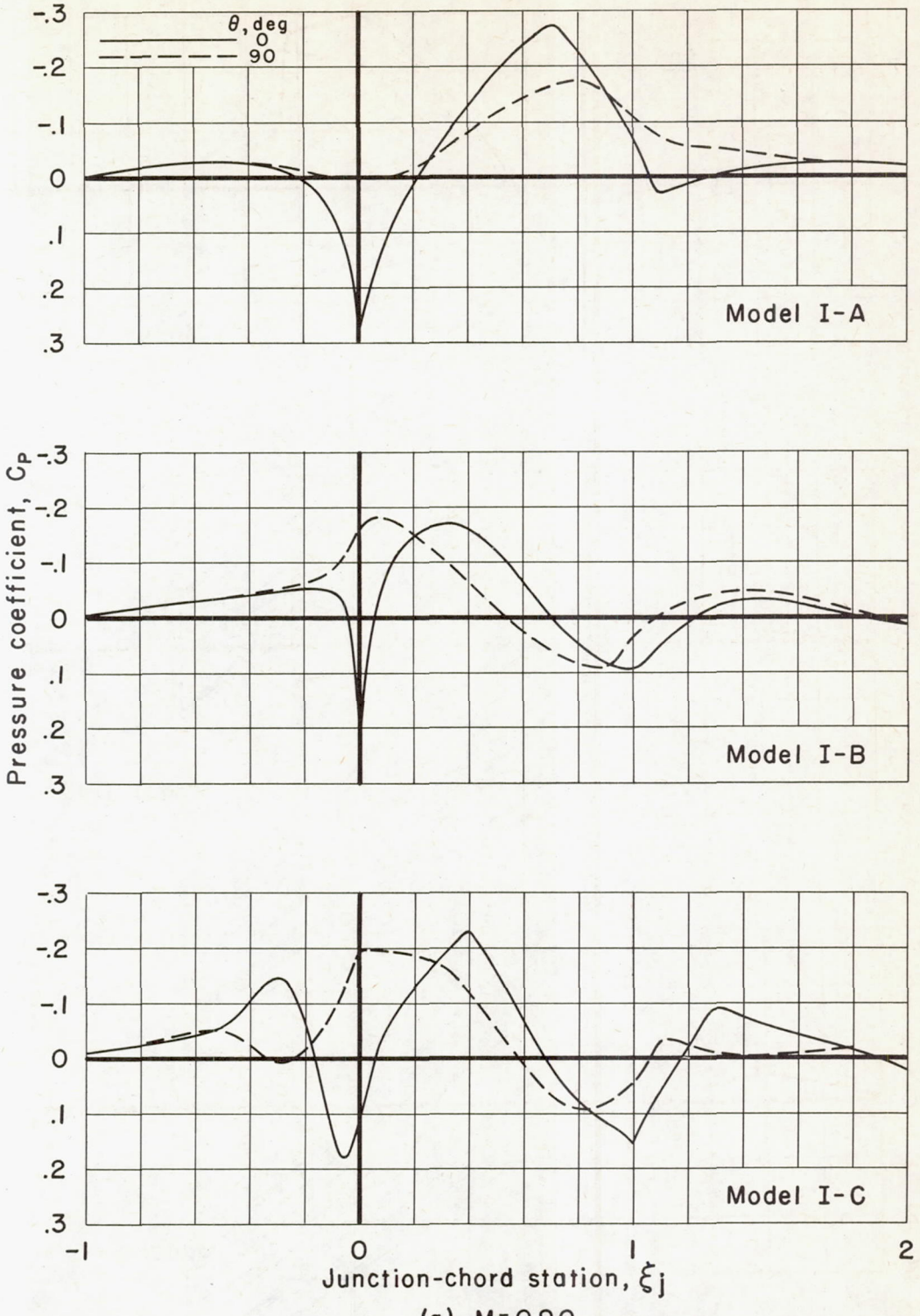

(a) M=0.90

Figure 22.- Experimental body pressure distributions for model series I at zero lift.

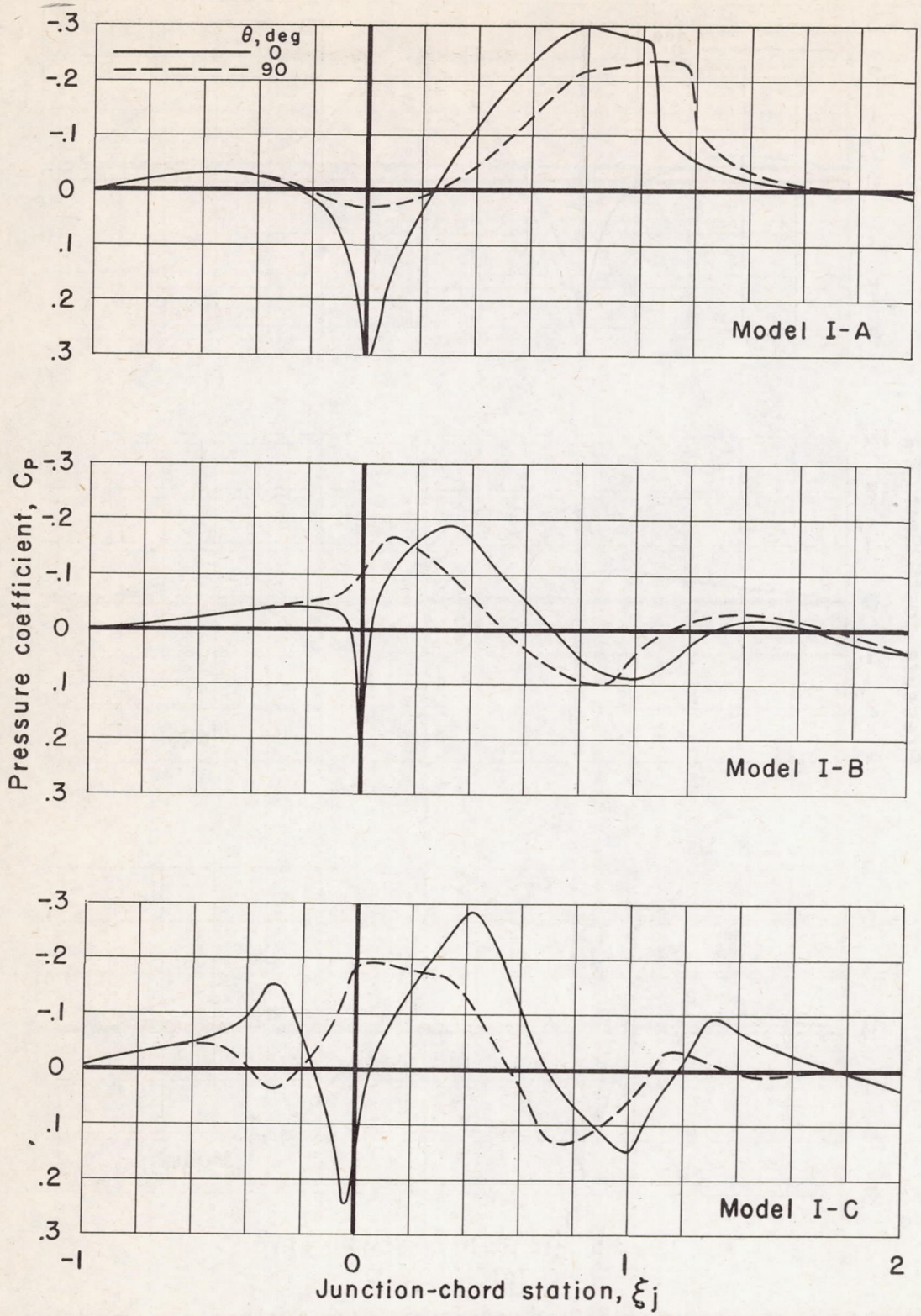

(b) M=0.94

Figure 22.- Continued.

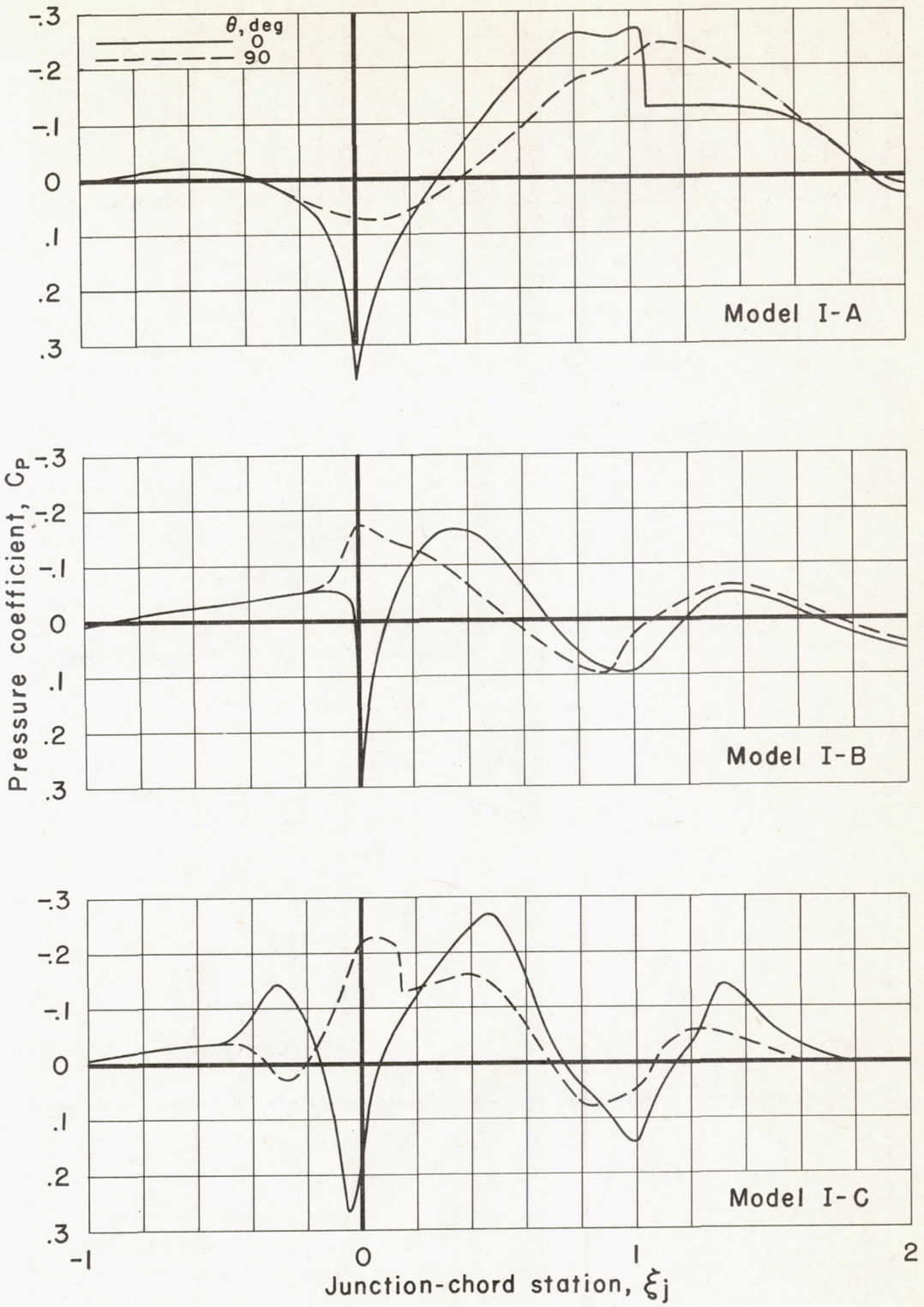

(c) M=0.98

Figure 22.- Continued.

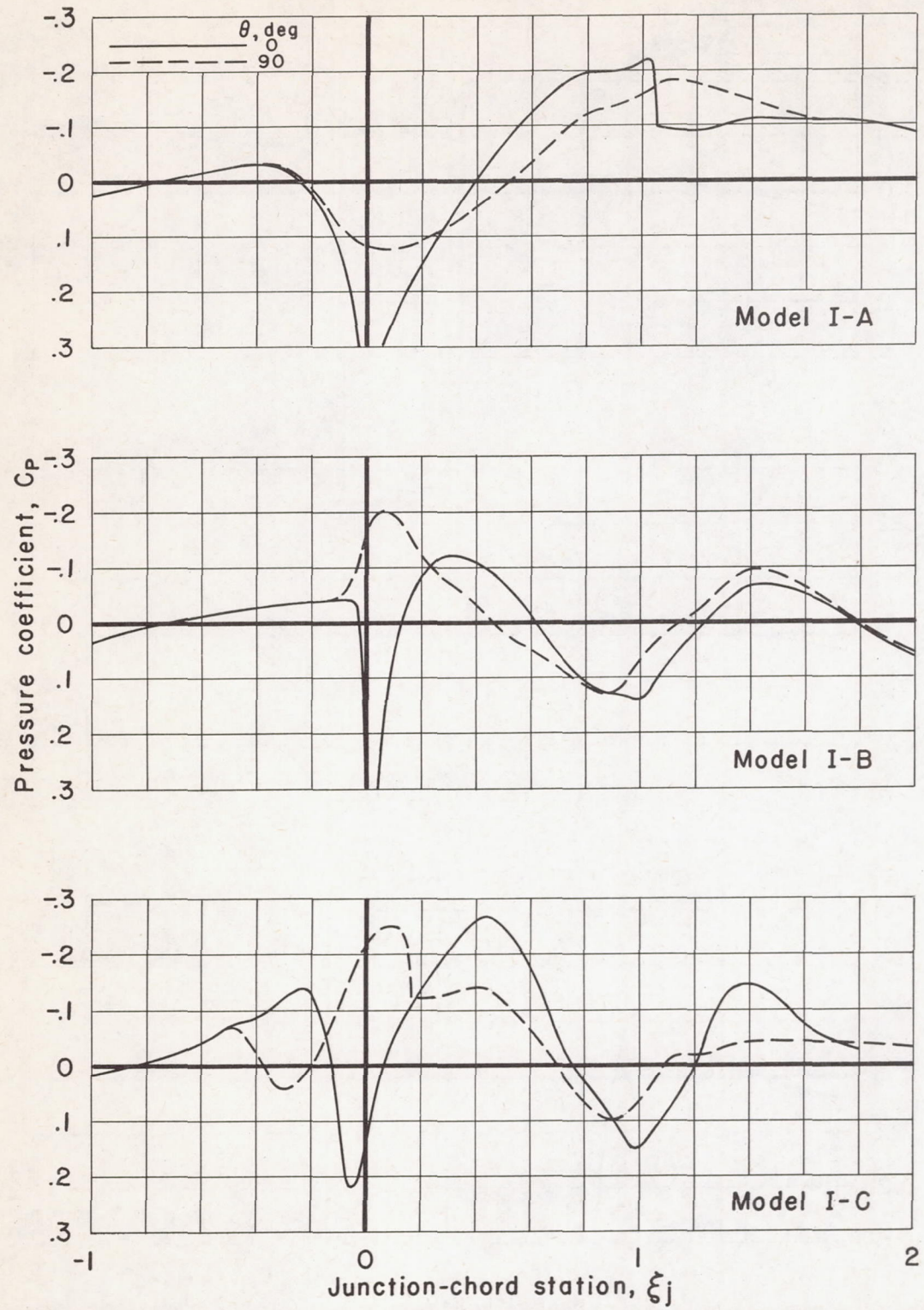

(d) M = 1.02

Figure 22.- Continued.

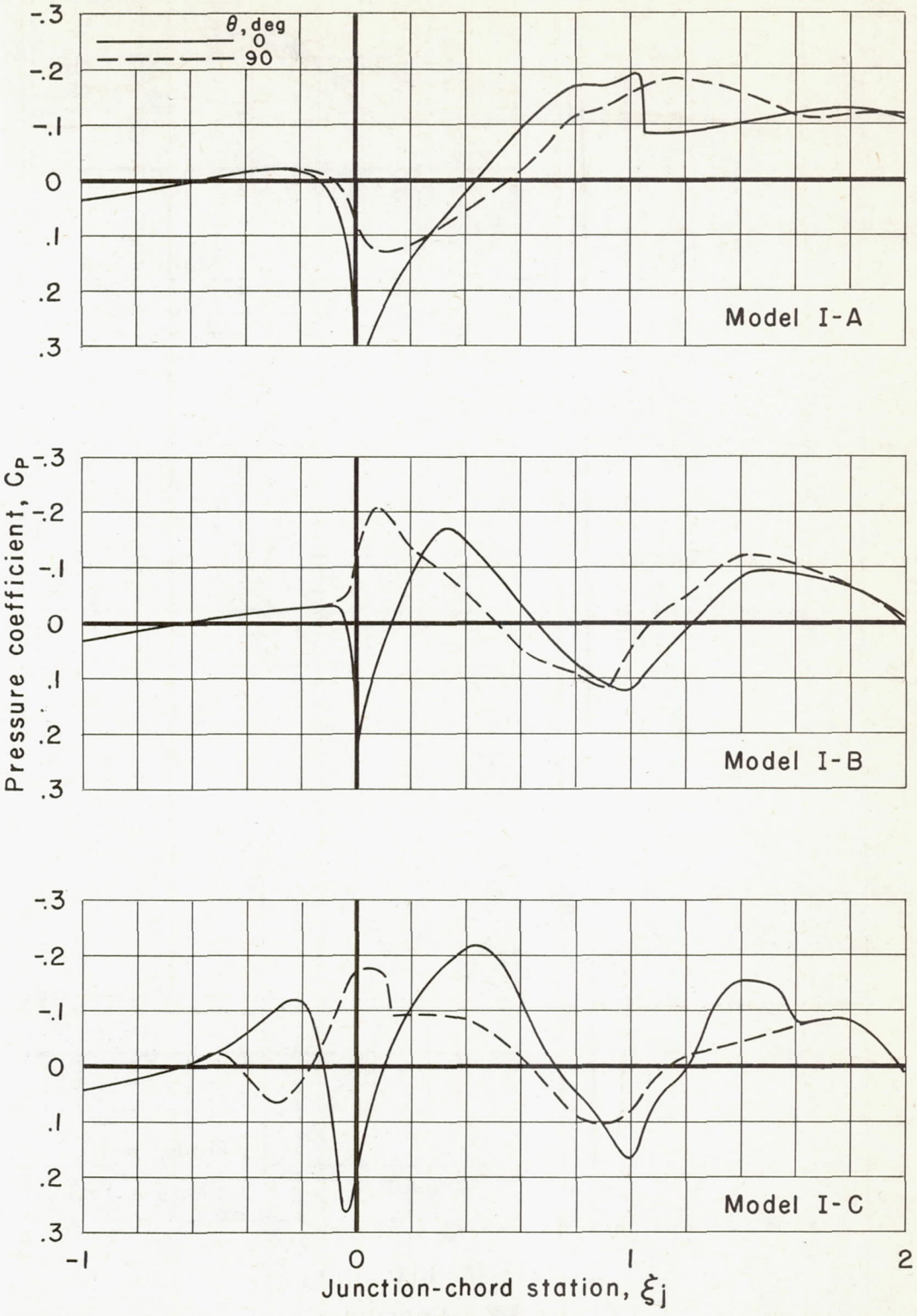

(e) M = 1.06

Figure 22.- Continued.

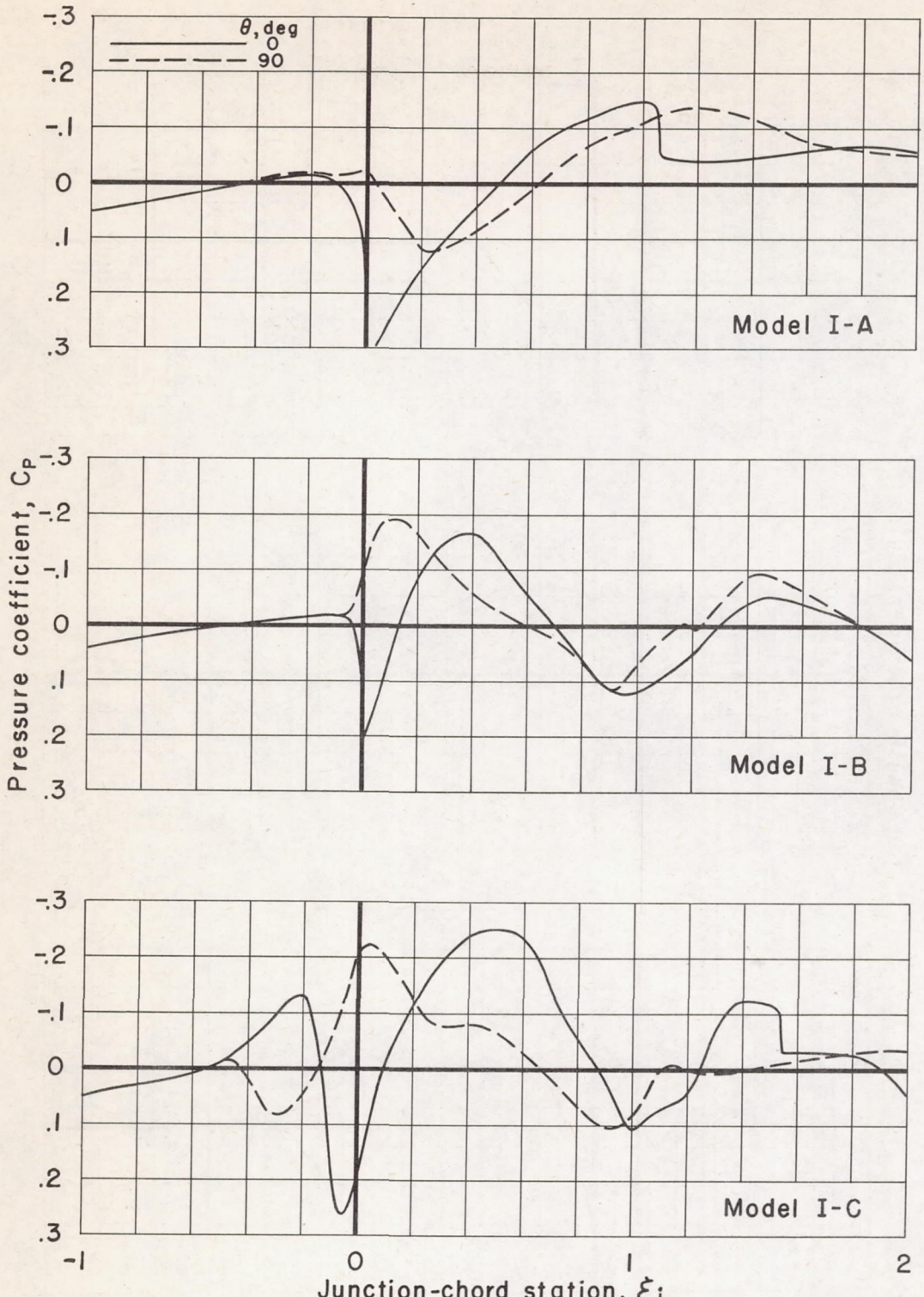

(f) M = 1.10

Figure 22.- Concluded.

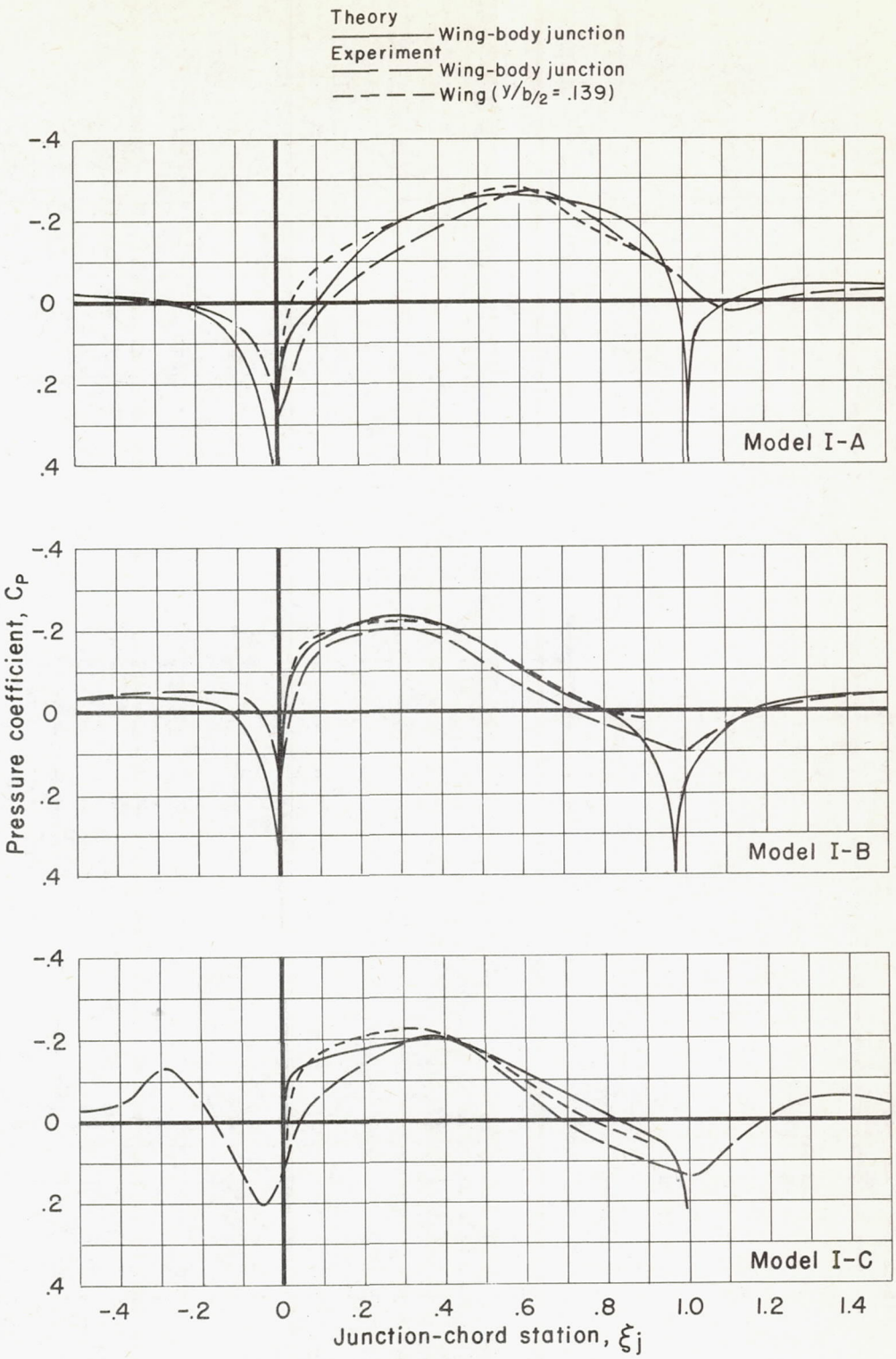

(a) M = 0.85

Figure 23.- Theoretical and experimental pressure distributions near the wing-body junctions of model series I at zero lift.

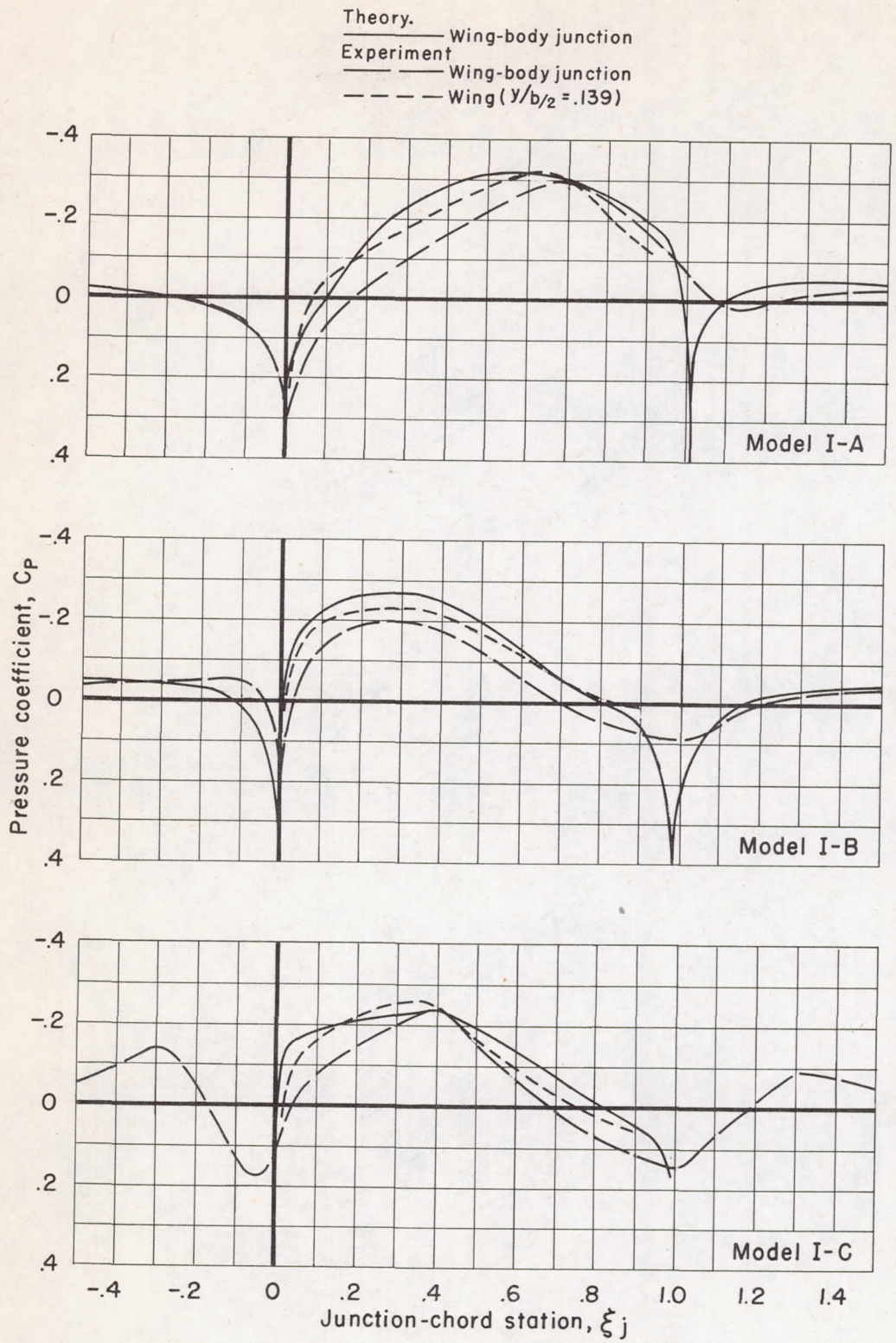

(b) M = 0.90

Figure 23.- Concluded.

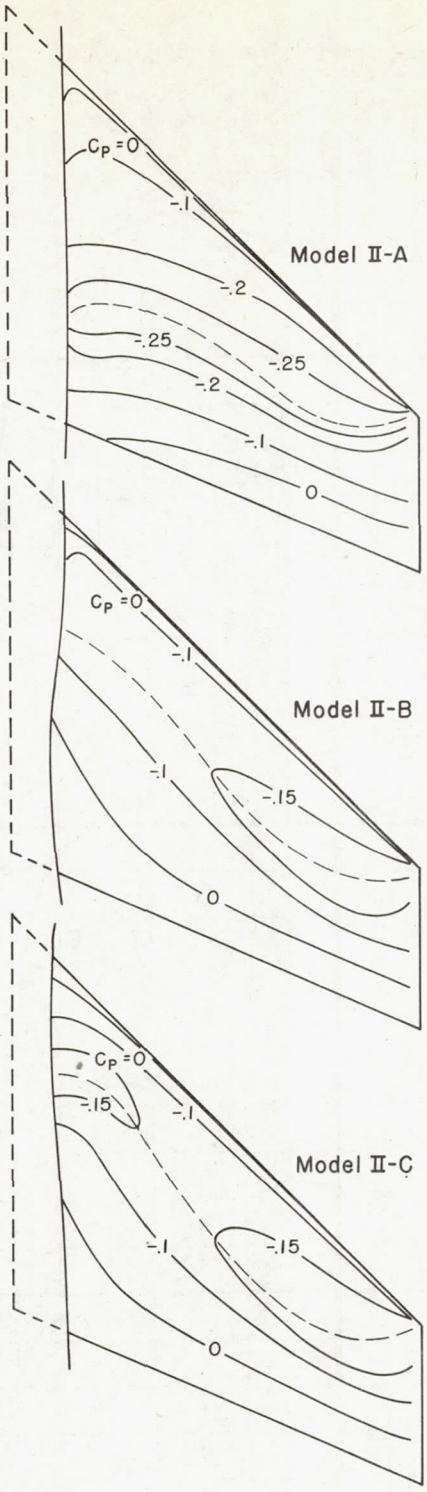

(a) M=0.90

Figure 24.- Experimental wing isobars for models II-A, II-B, and II-C at zero lift.

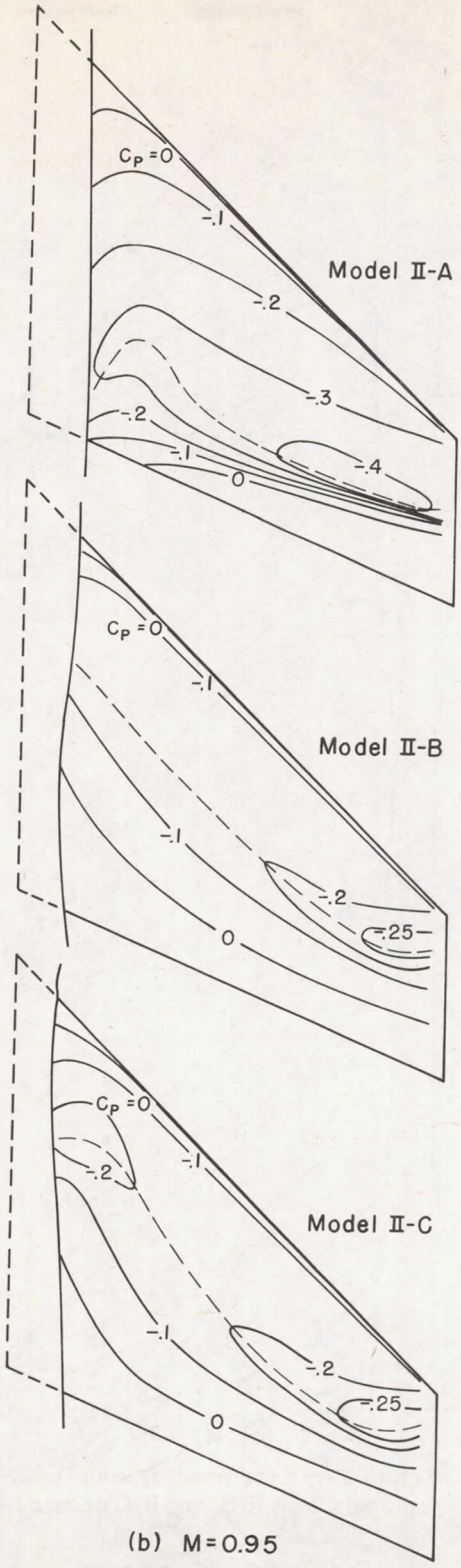

(b) M=0.95

Figure 24.- Continued.

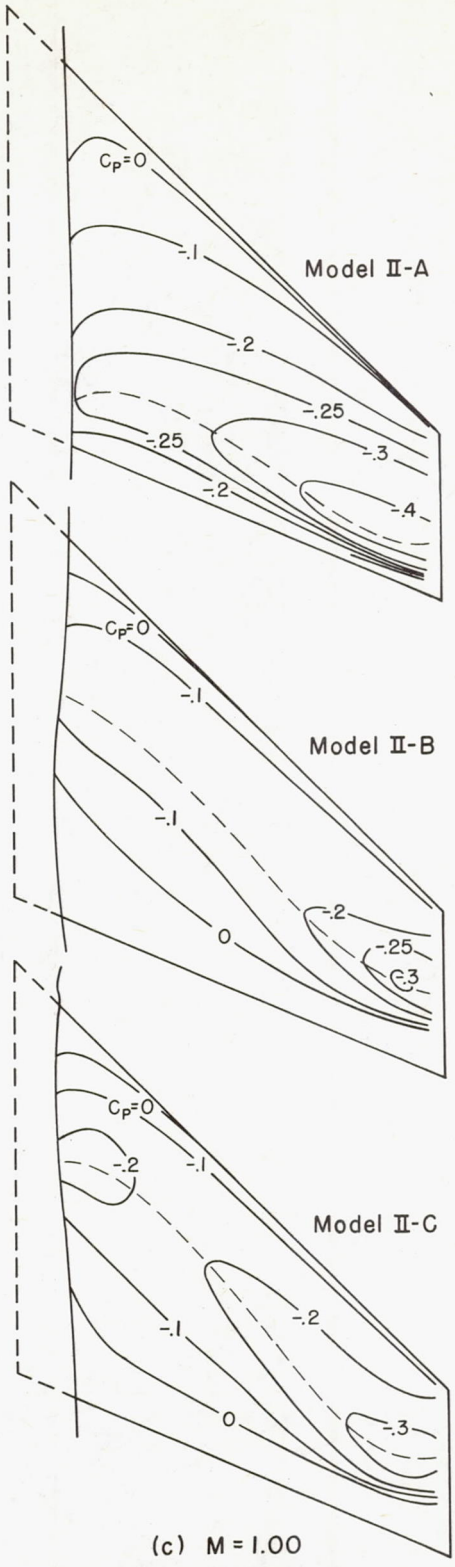

(c) M = 1.00

Figure 24.- Continued.

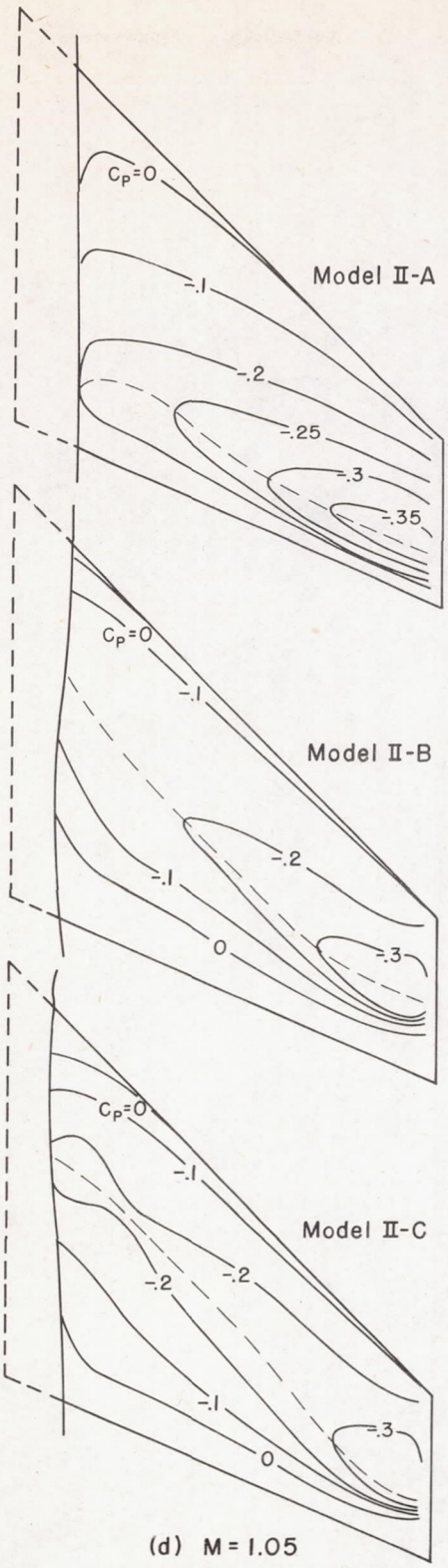

(d) M = 1.05

Figure 24.- Continued.

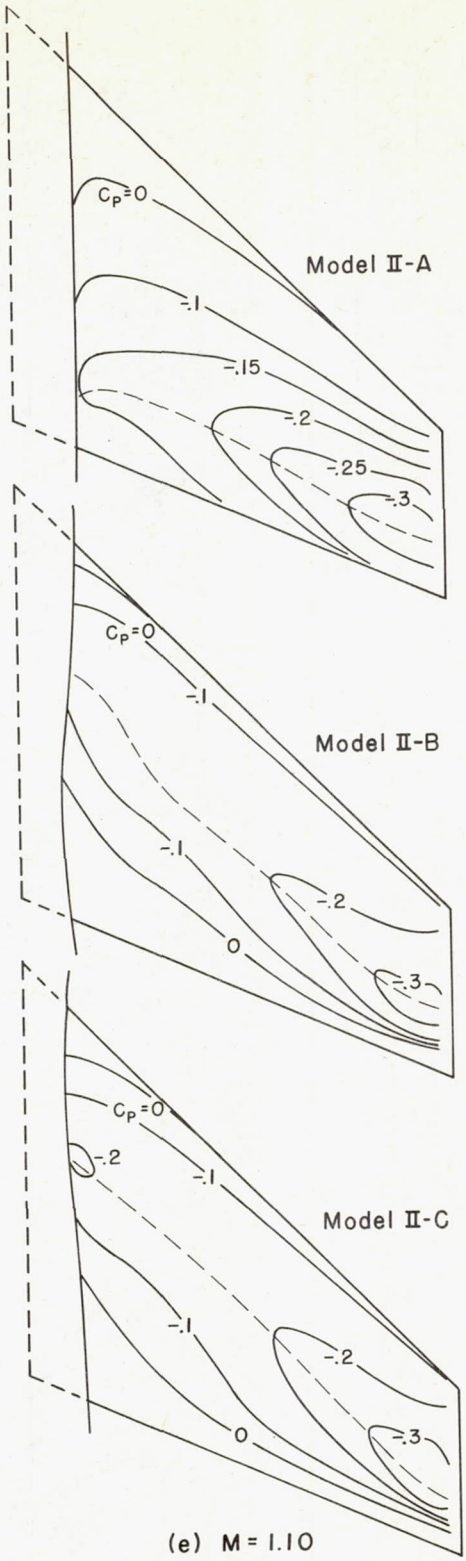

(e) M = 1.10

Figure 24.- Continued.

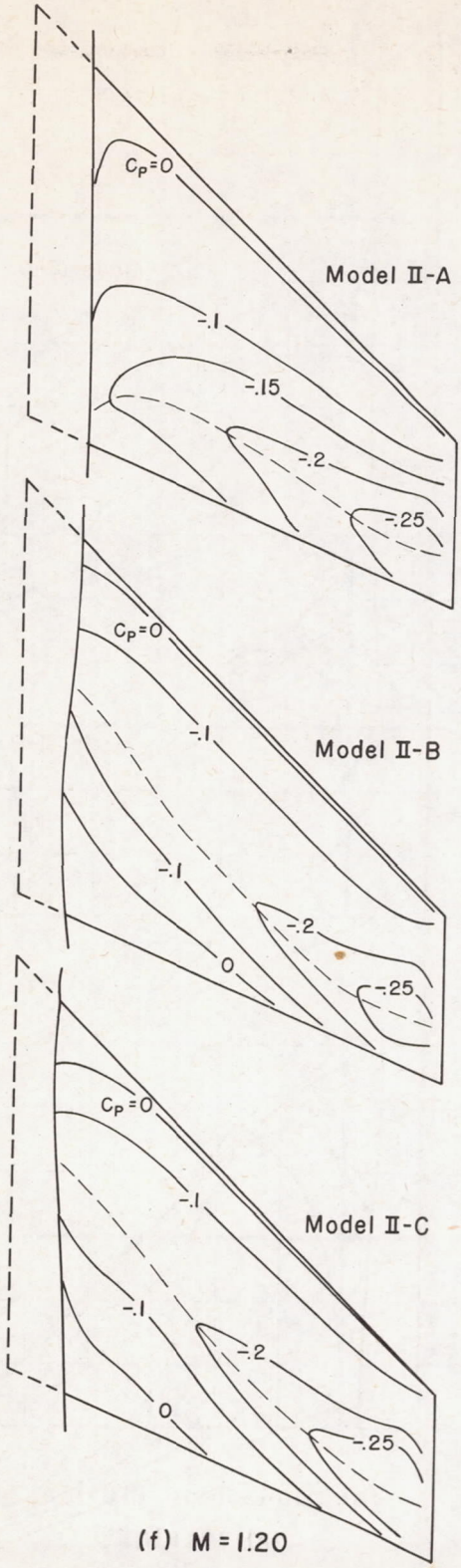

(f) M = 1.20

Figure 24.- Concluded.

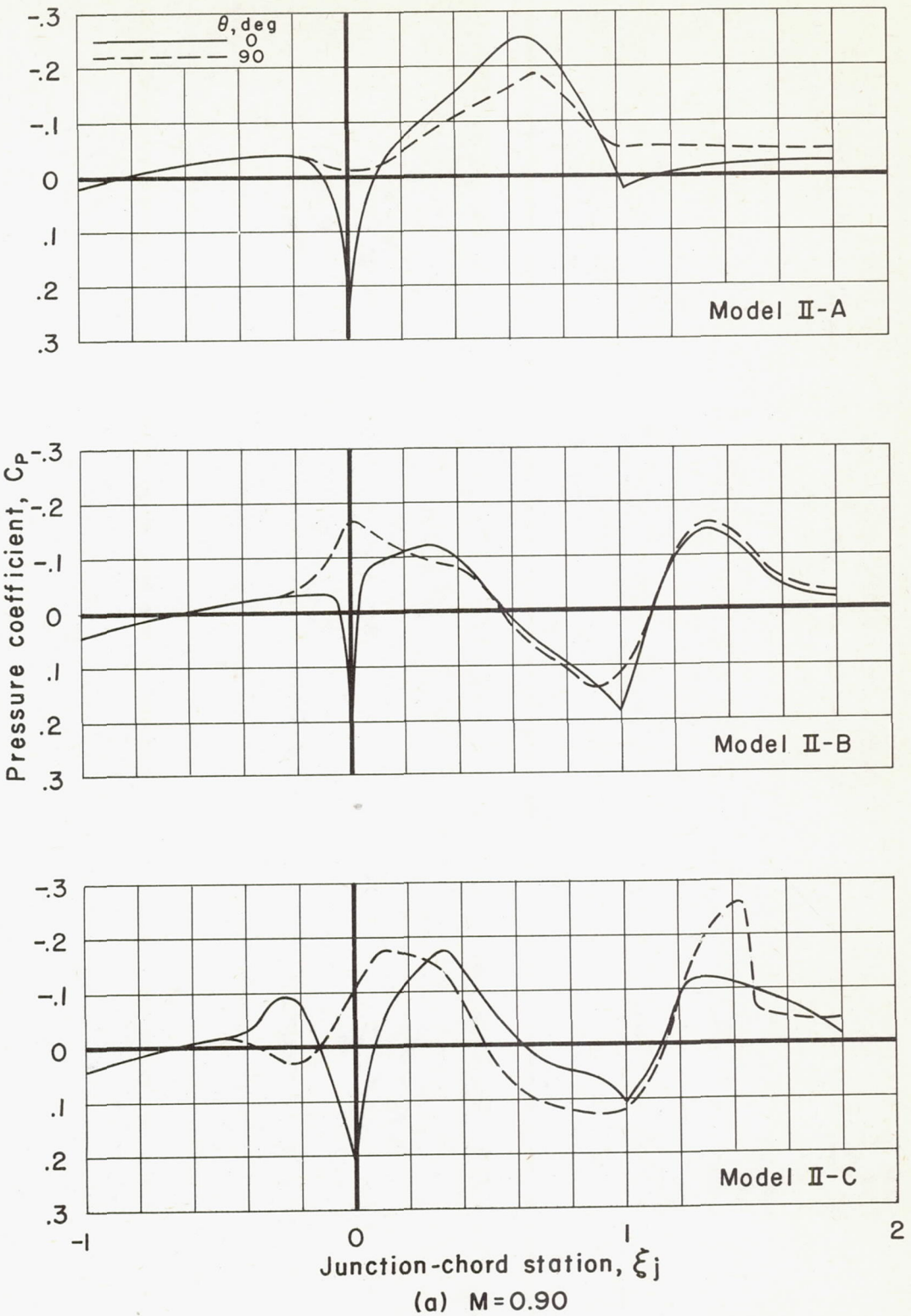

(a) M=0.90

Figure 25.- Experimental body pressure distributions for models II-A, II-B, and II-C at zero lift.

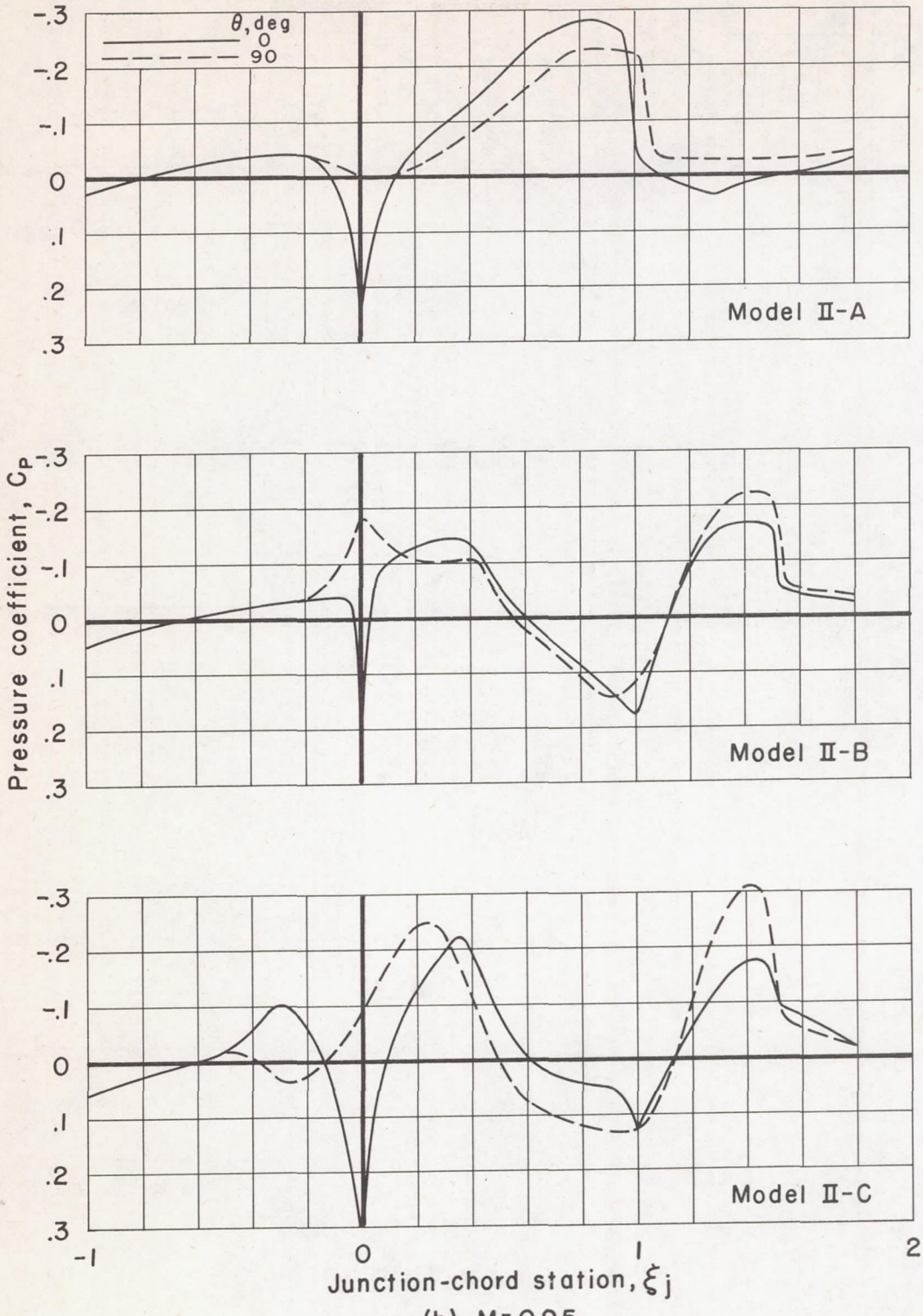

(b) M=0.95

Figure 25.- Continued.

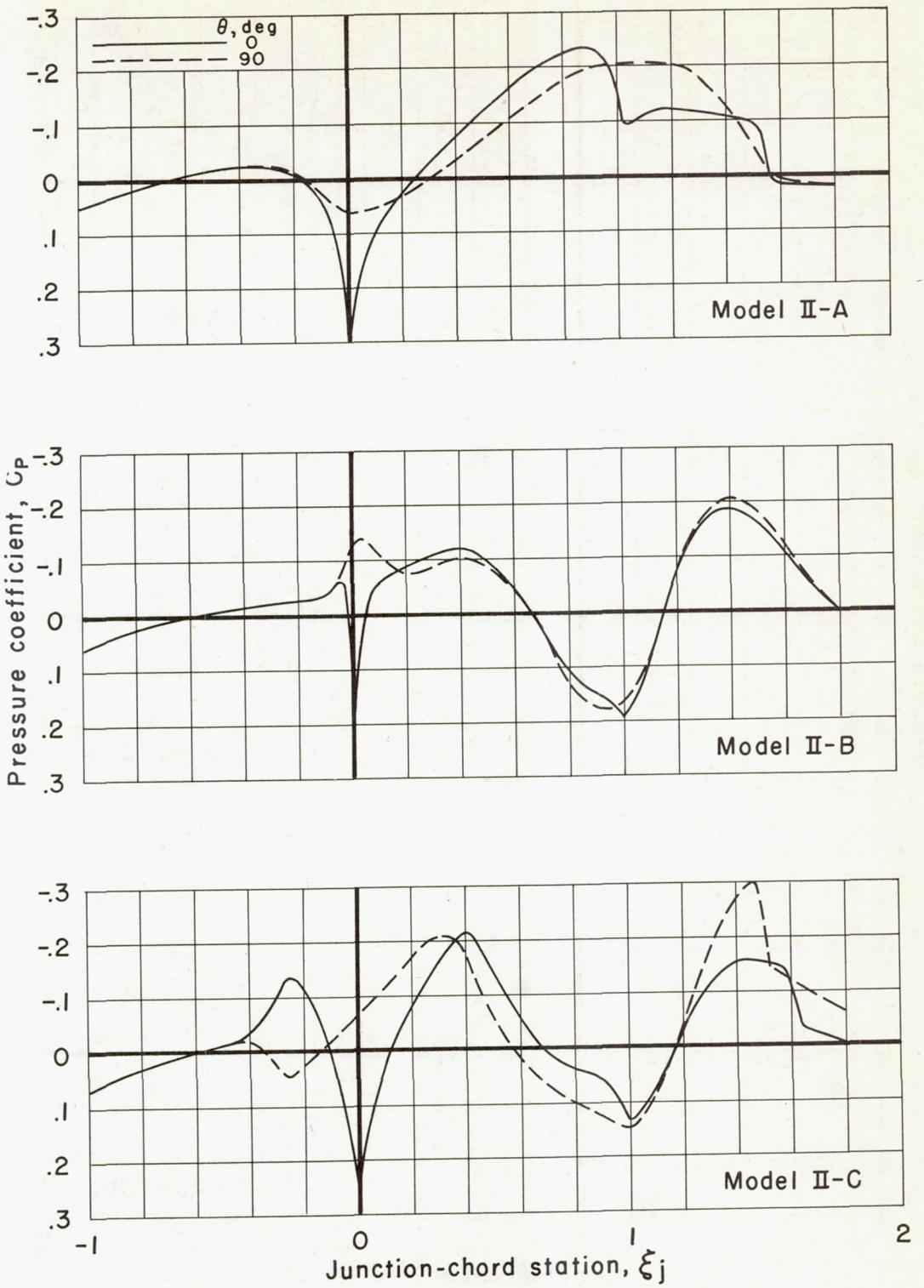

(c) M = 1.00

Figure 25.- Continued.

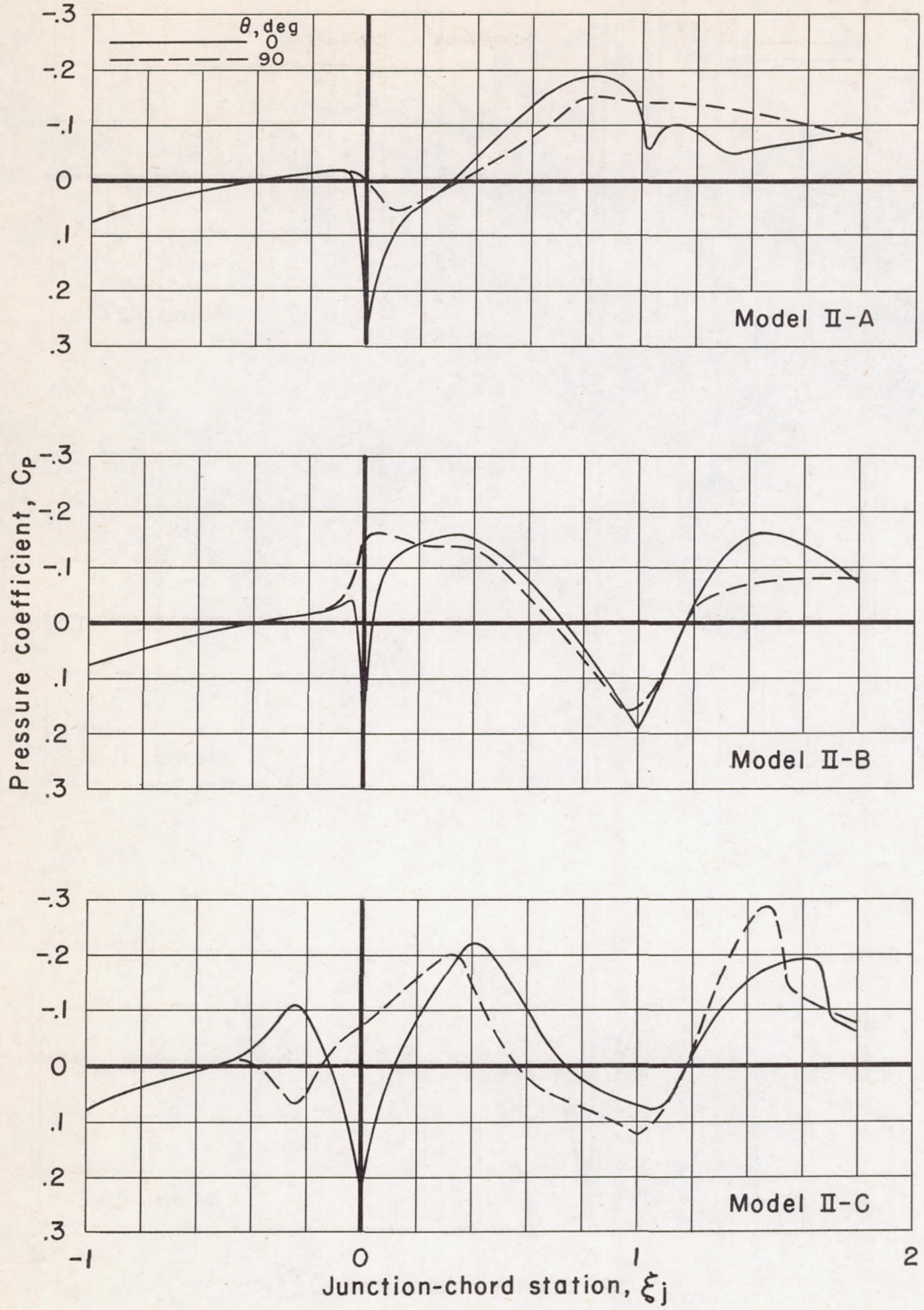

(d) M = 1.05

Figure 25.- Continued.

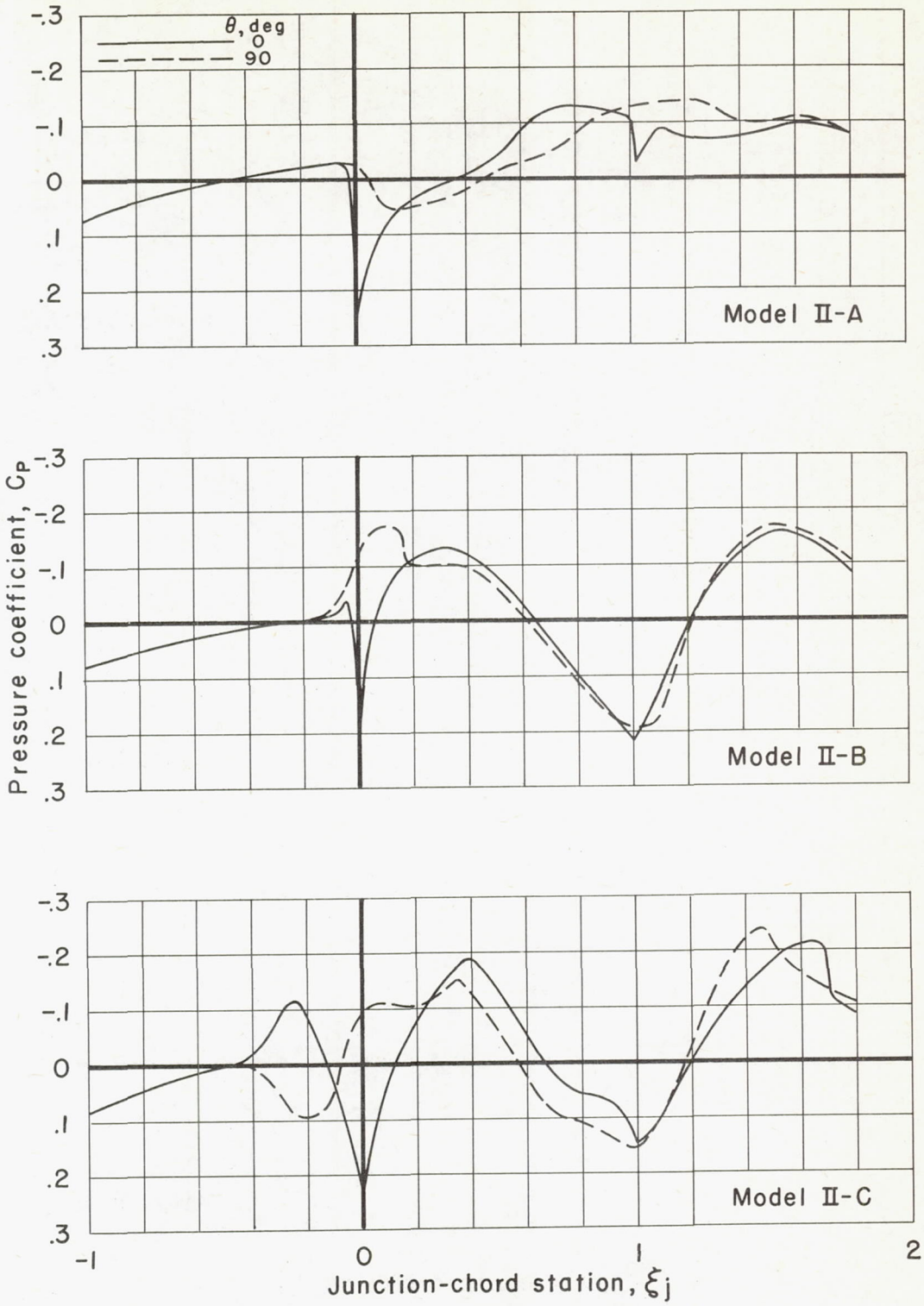

(e) M = 1.10

Figure 25.- Continued.

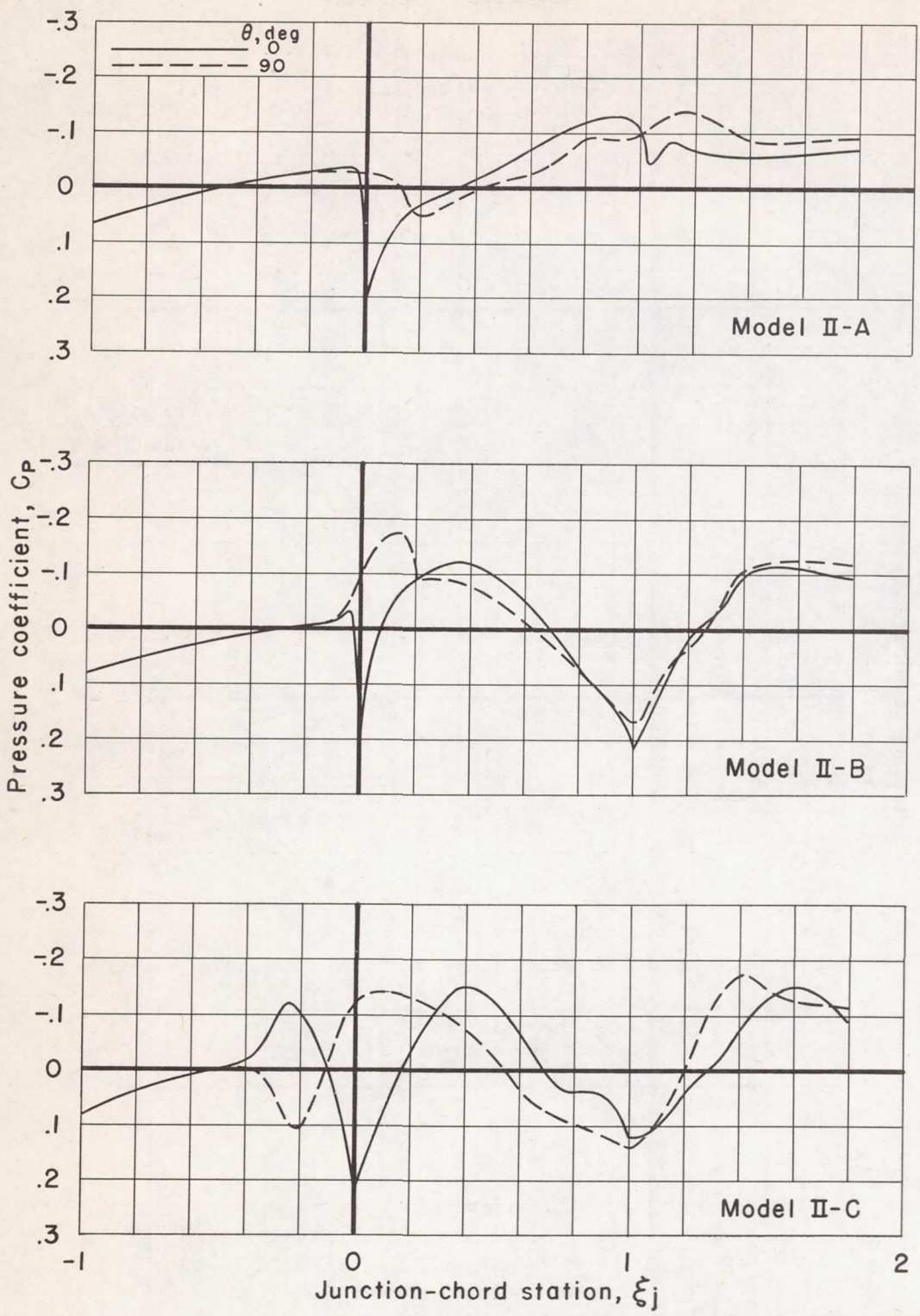

(f) M = 1.20

Figure 25.- Concluded.

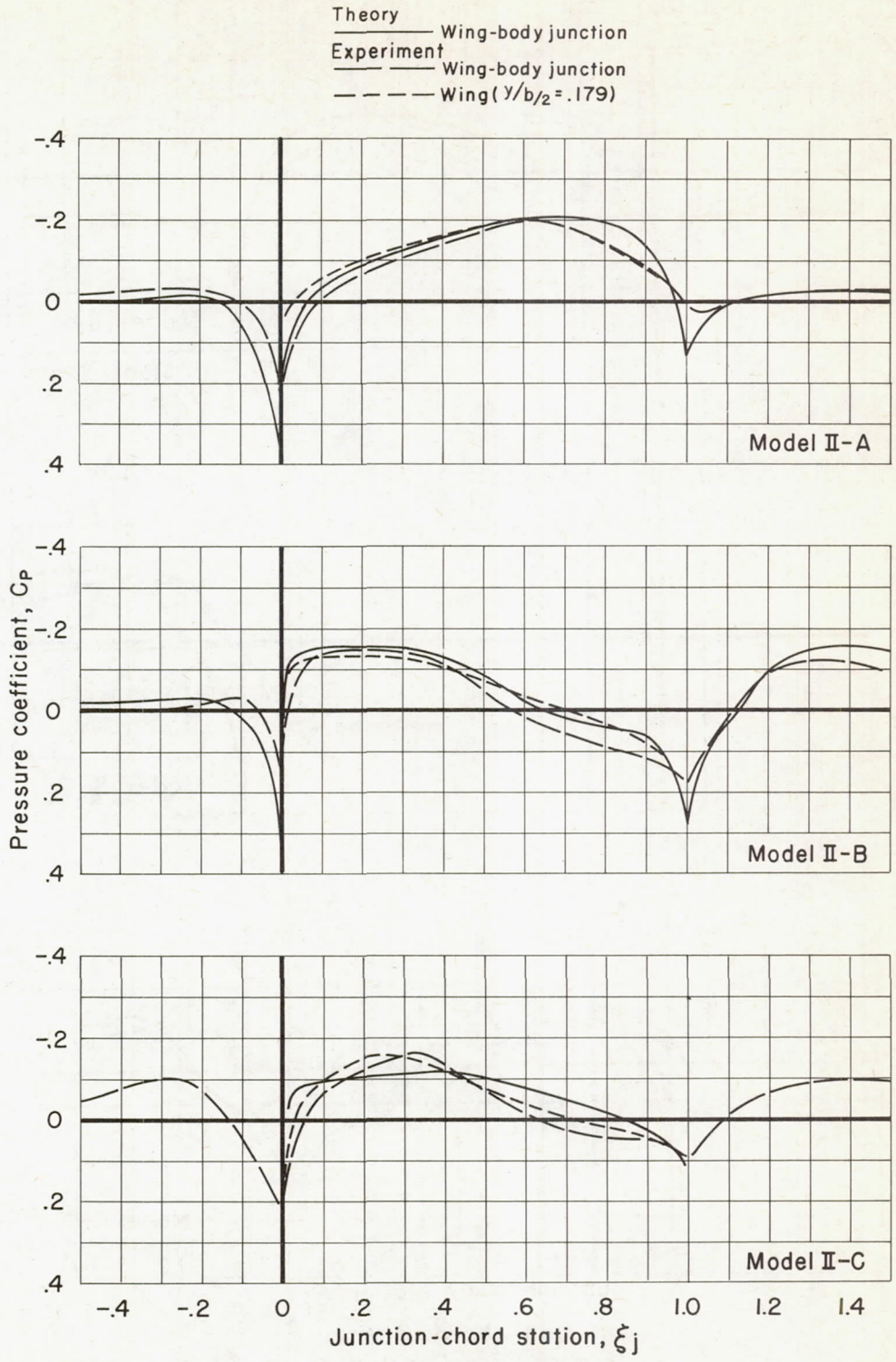

(a) M = 0.85

Figure 26.- Theoretical and experimental pressure distributions near the wing-body junctions of models II-A, II-B, and II-C at zero lift.

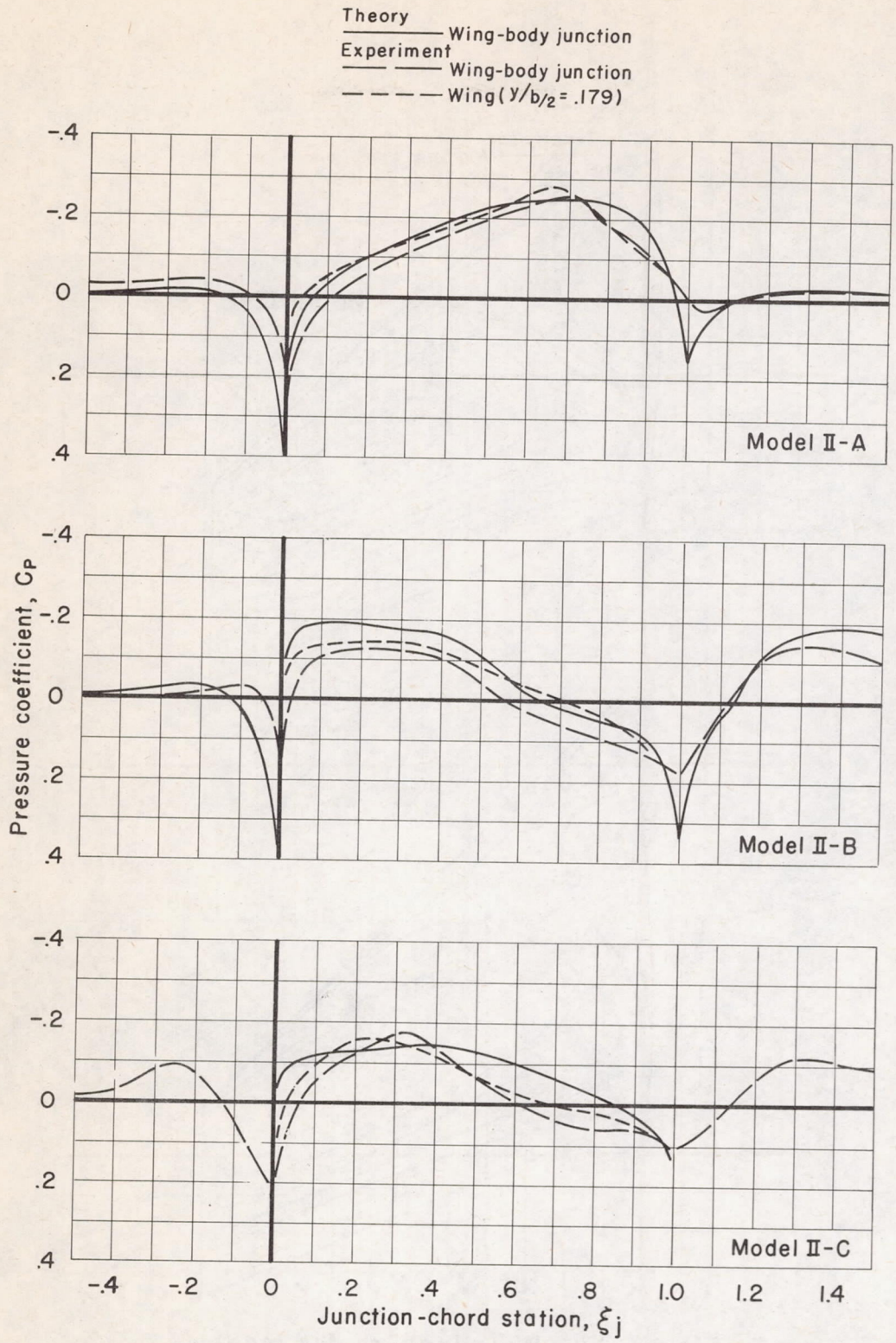

(b) M=0.90

Figure 26.- Concluded.

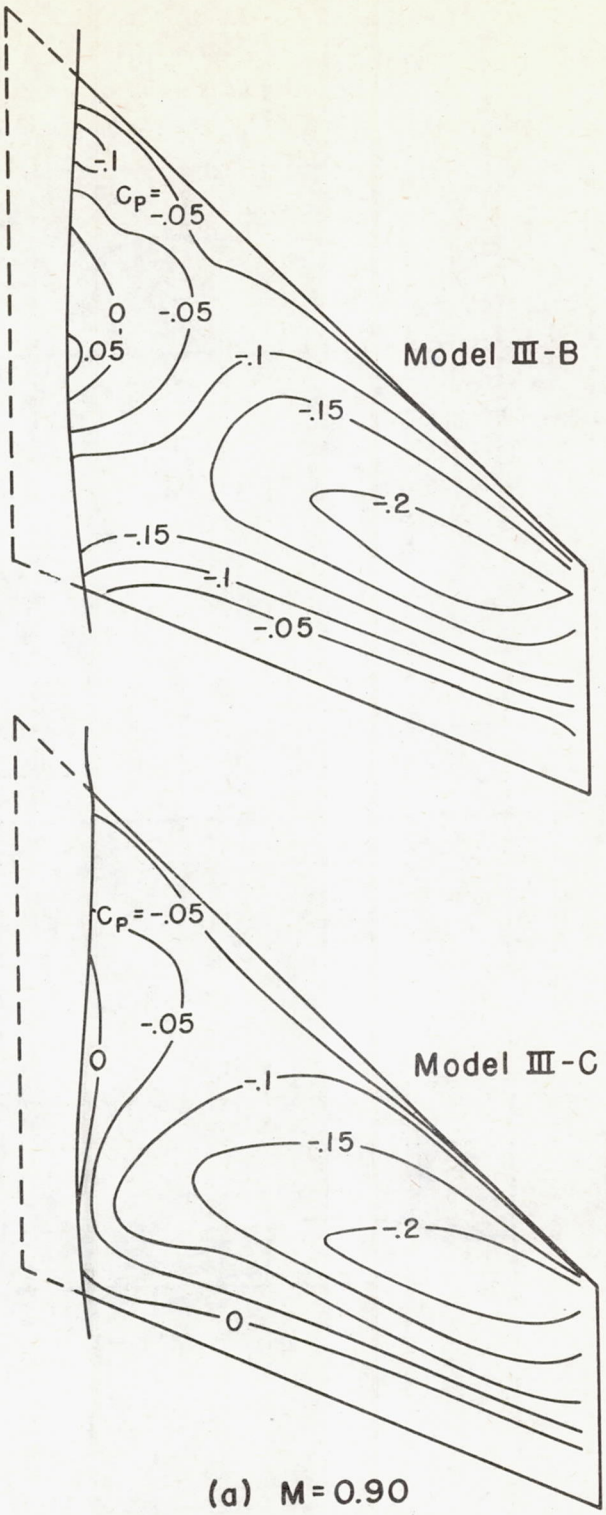

(a) M = 0.90

Figure 27.- Wing isobars for models III-B and III-C at zero lift.

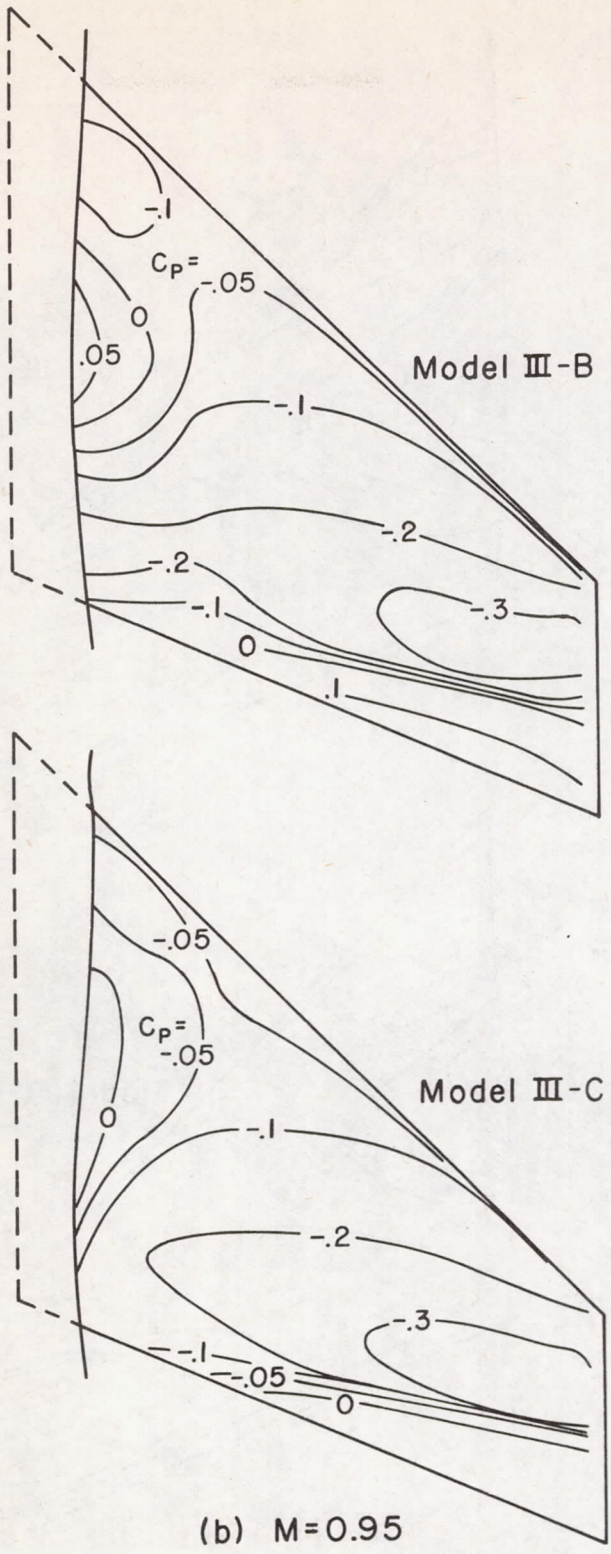

(b) M=0.95

Figure 27.- Continued.

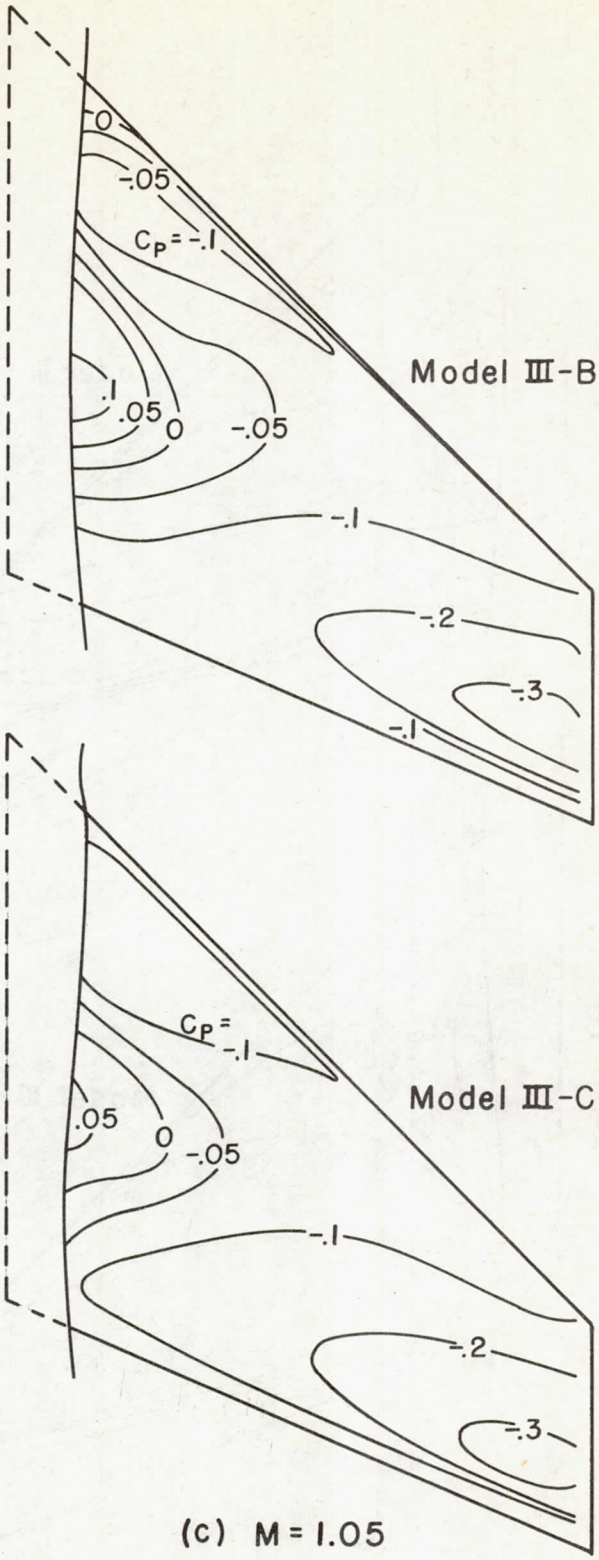

(c) M = 1.05

Figure 27.- Continued.

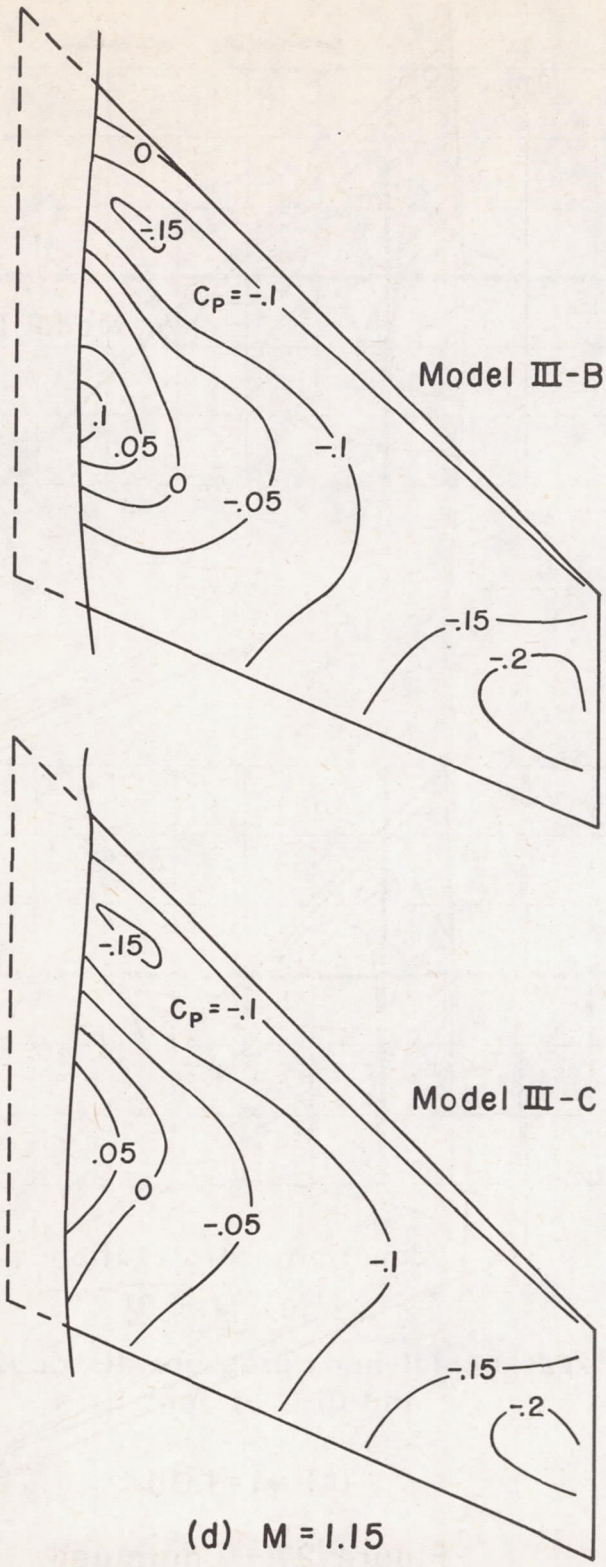

(d) M = 1.15

Figure 27.- Concluded.

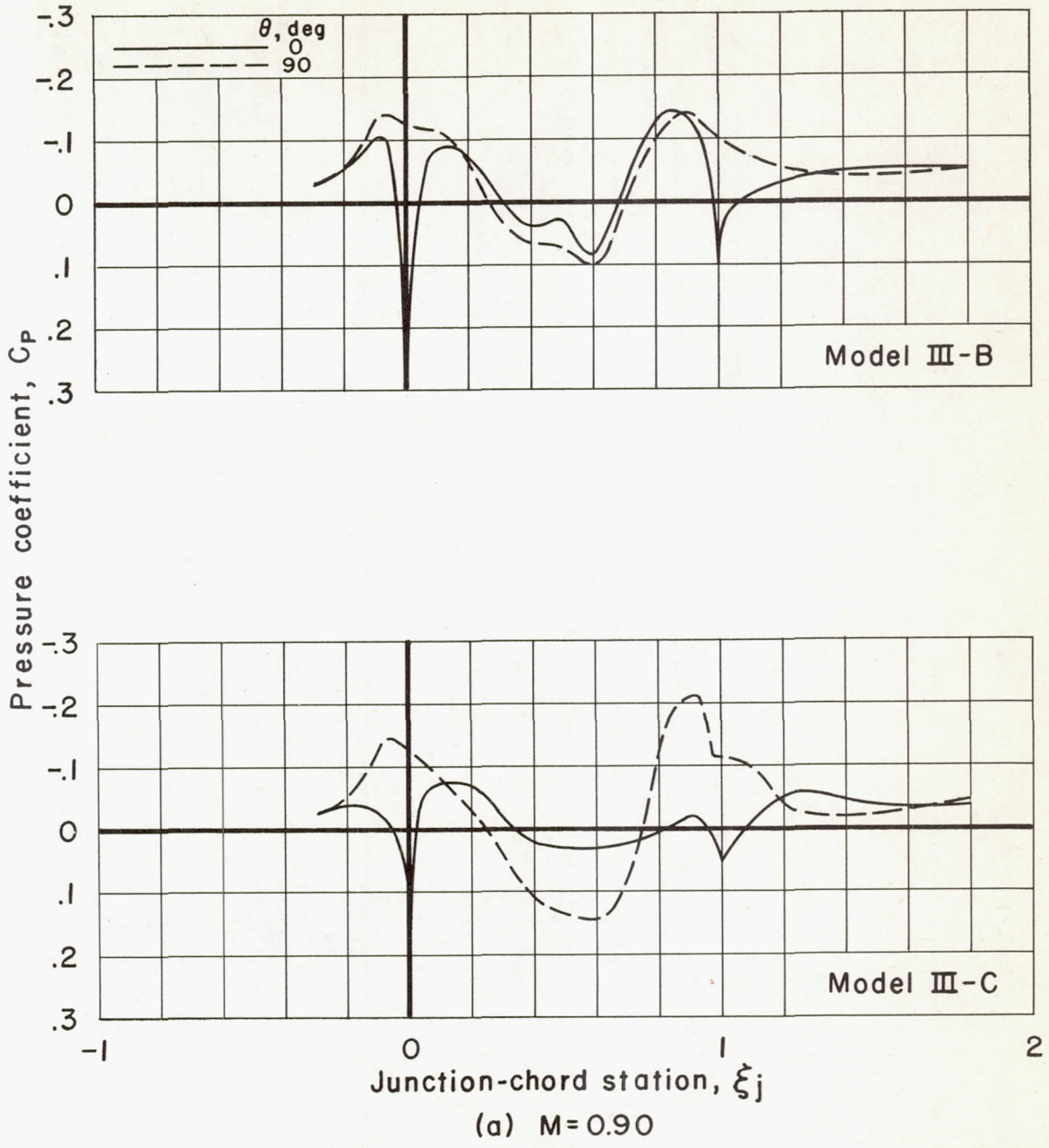

(a) M = 0.90

Figure 28.- Experimental body pressure distributions for models III-B and III-C at zero lift.

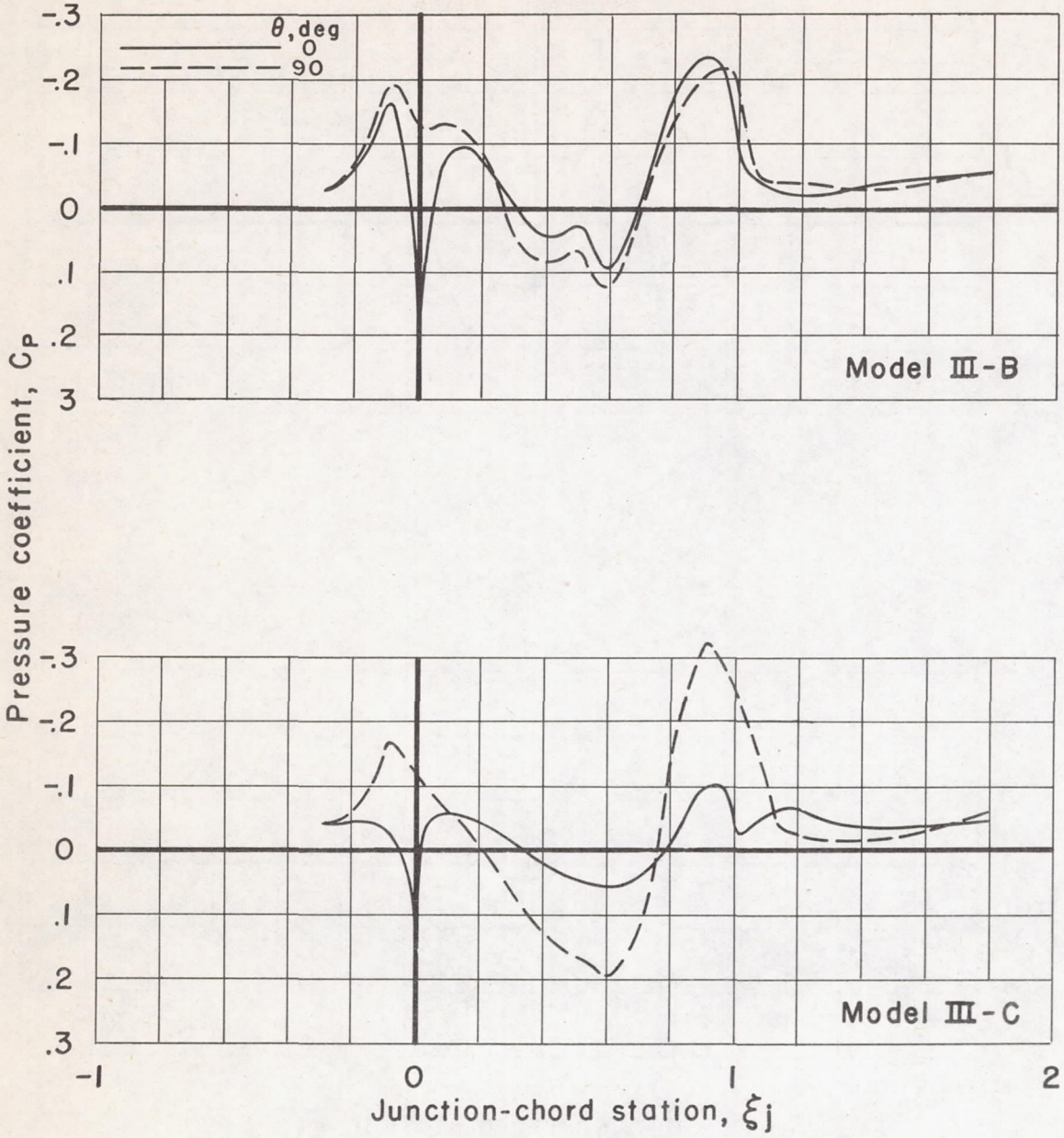

(b) M=0.95

Figure 28.- Continued.

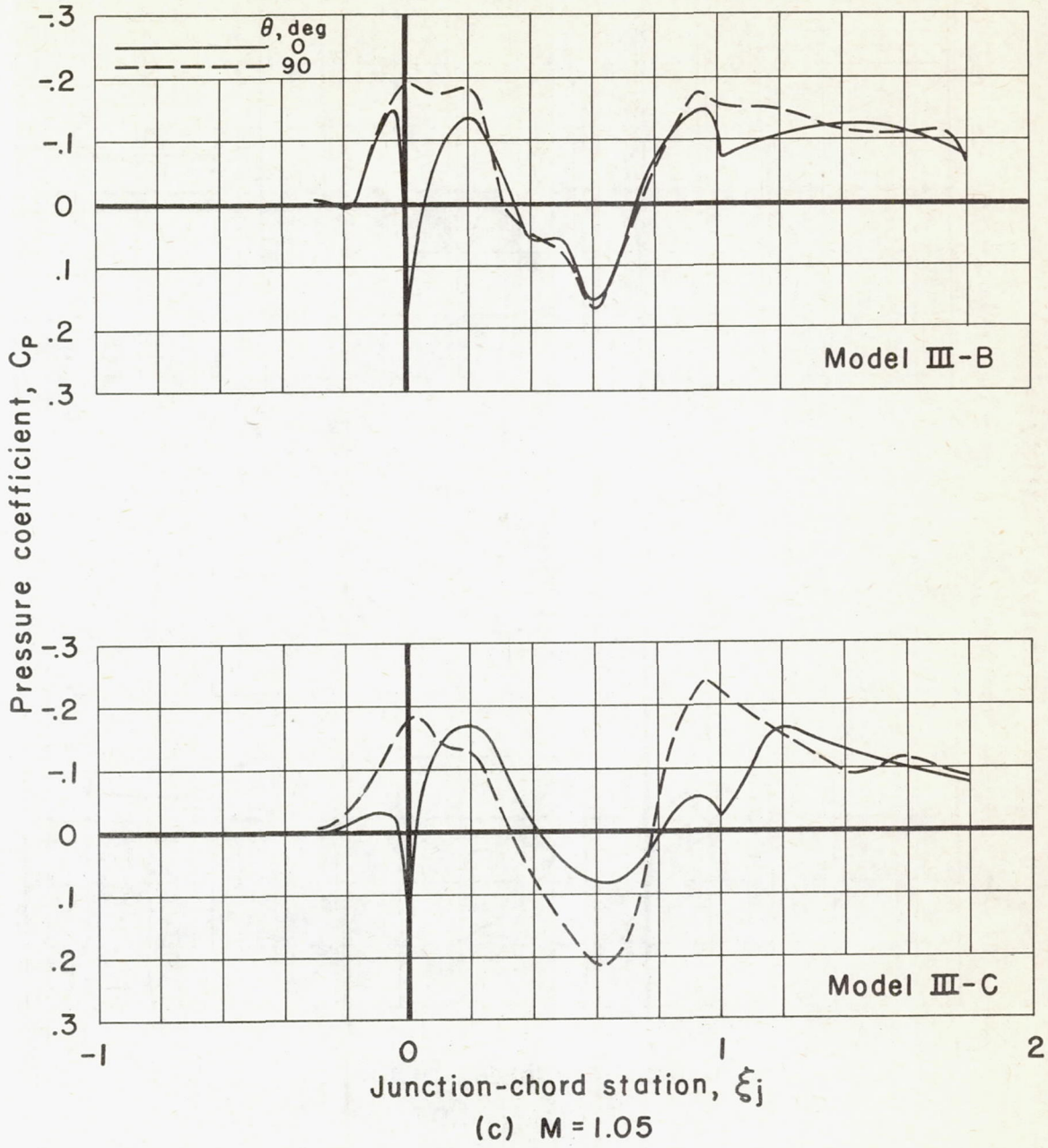

(c) M = 1.05

Figure 28.- Continued.

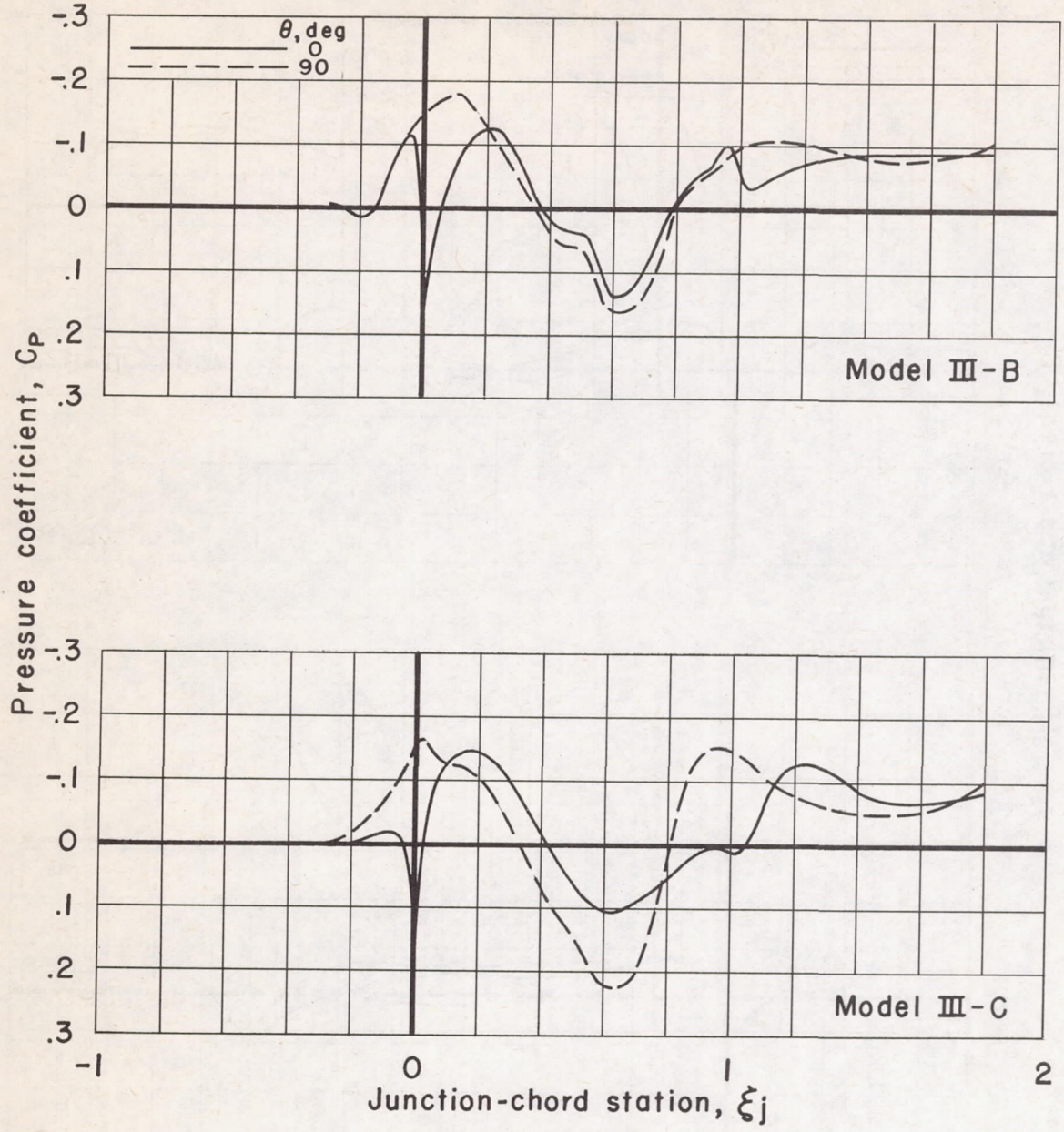

(d) M = 1.15

Figure 28.- Concluded.

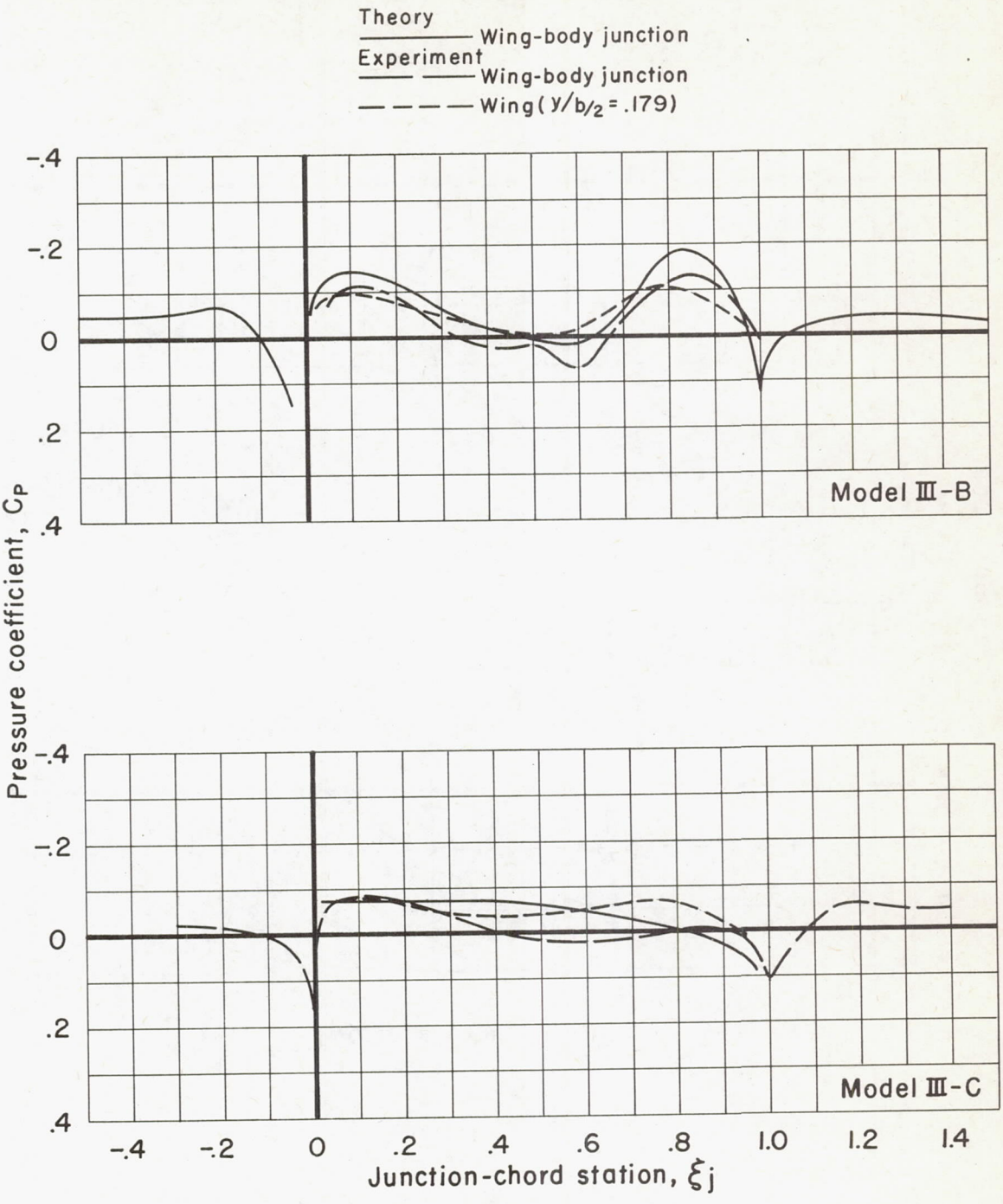

(a) M=0.85

Figure 29.- Theoretical and experimental pressure distributions near the wing-body junctions of models III-B and III-C at zero lift.

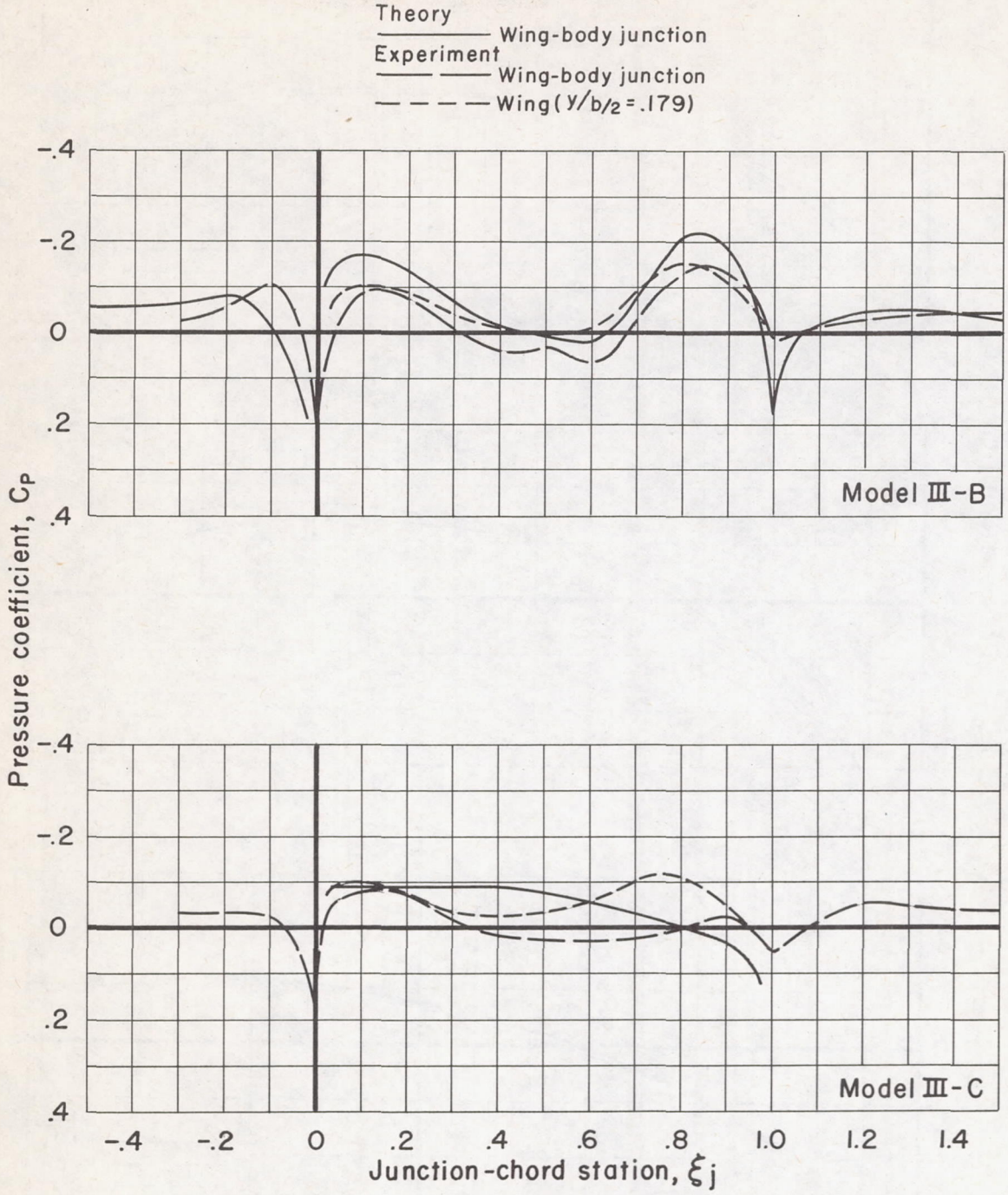

(b) M=0.90

Figure 29.- Concluded.

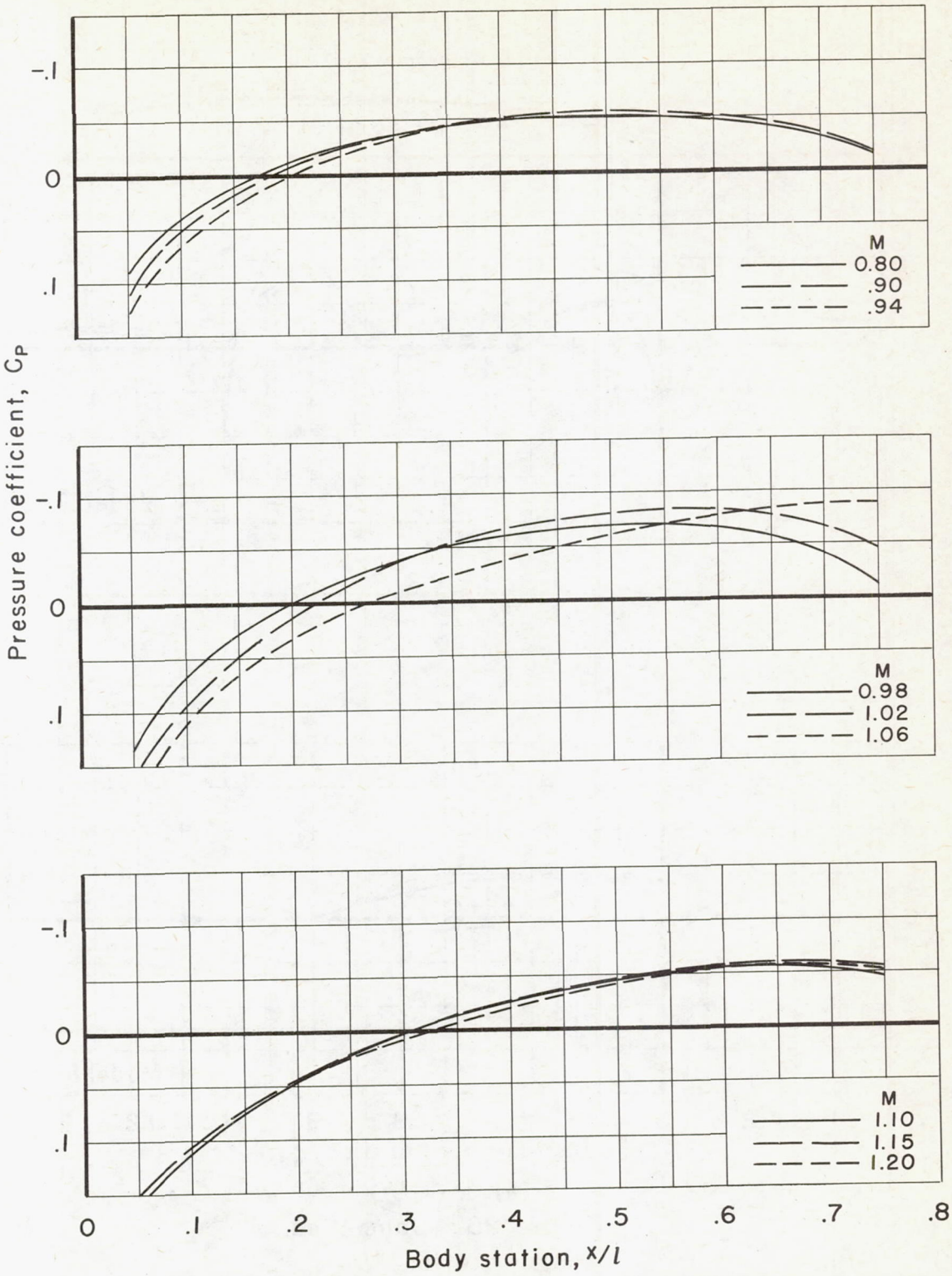

Figure 30.- Experimental pressures for body I-A (Sears-Haack body of fineness ratio 11) at zero lift.

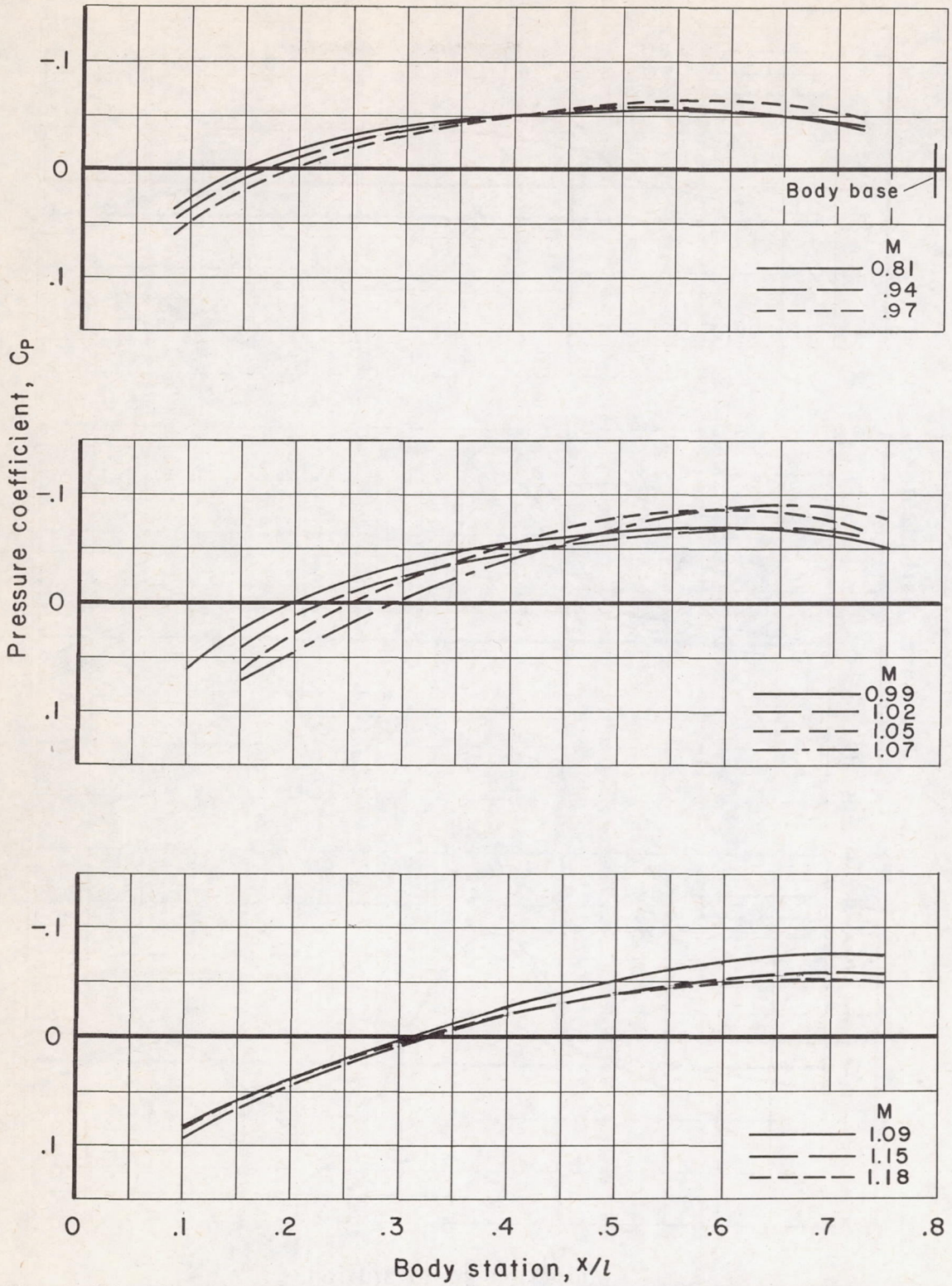

Figure 31.- Experimental pressures for body II-A (Sears-Haack body of fineness ratio 12.5) at zero lift.

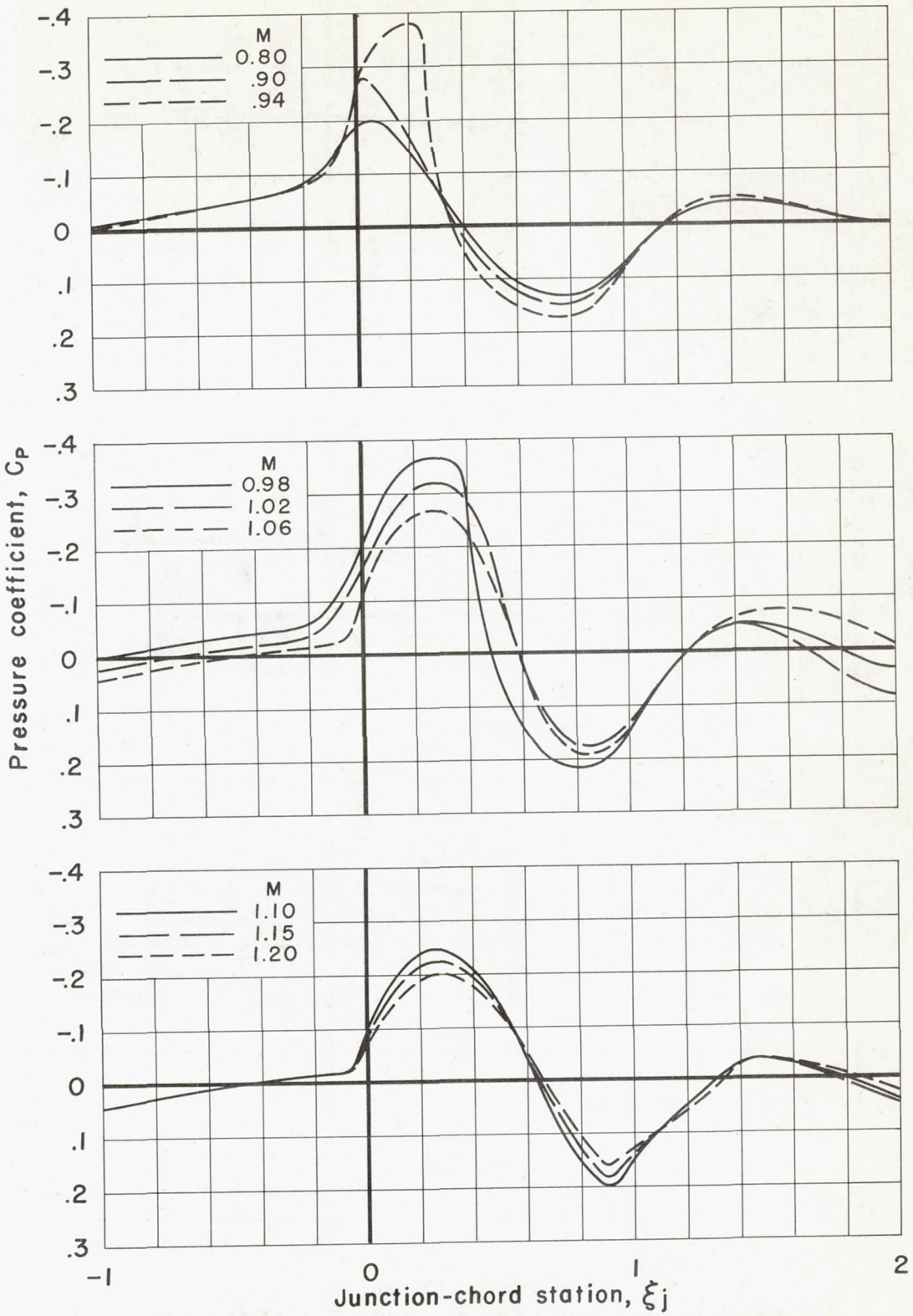

Figure 32.- Experimental pressures for body I-B at zero lift.

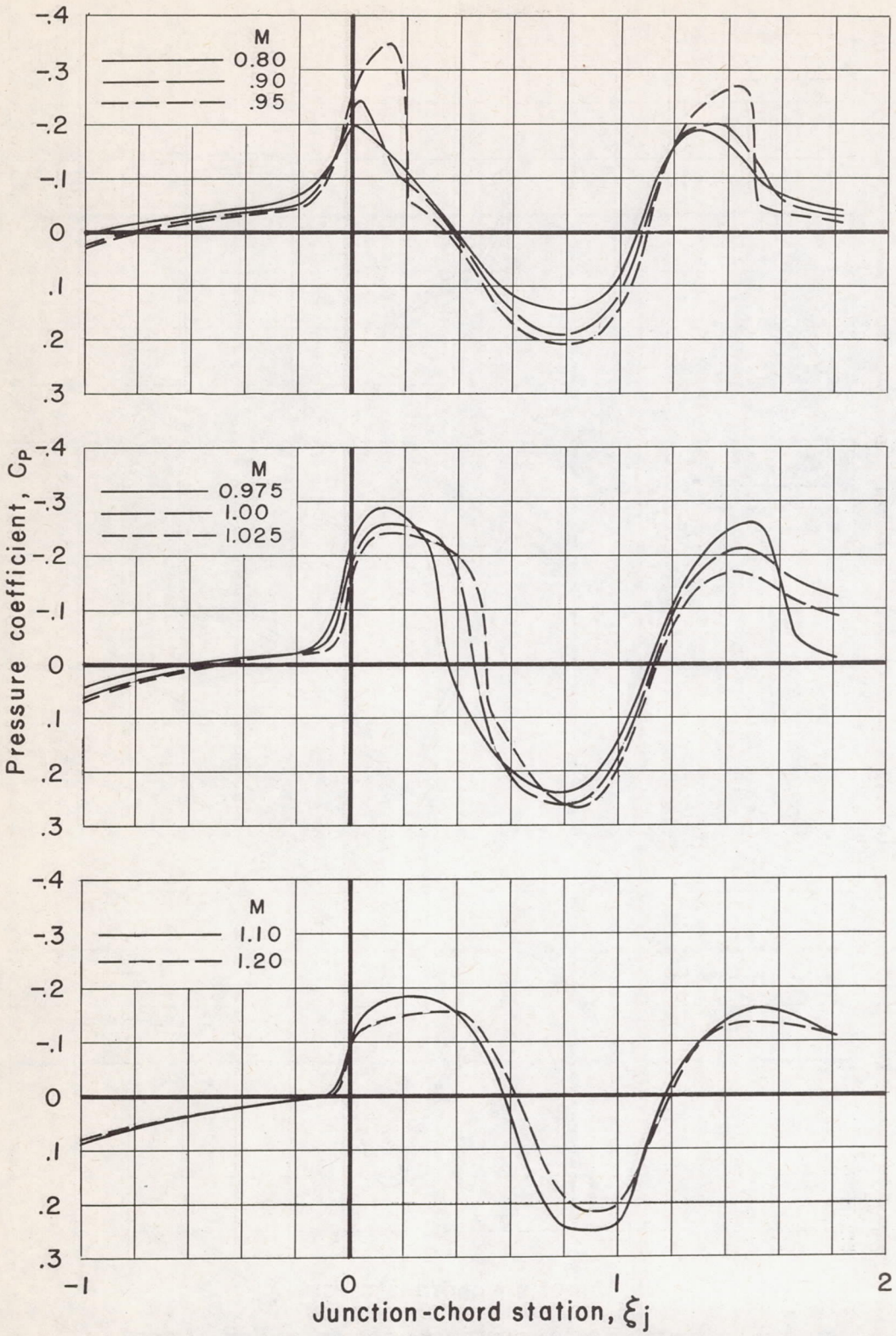

Figure 33.- Experimental pressures for body II-B at zero lift.

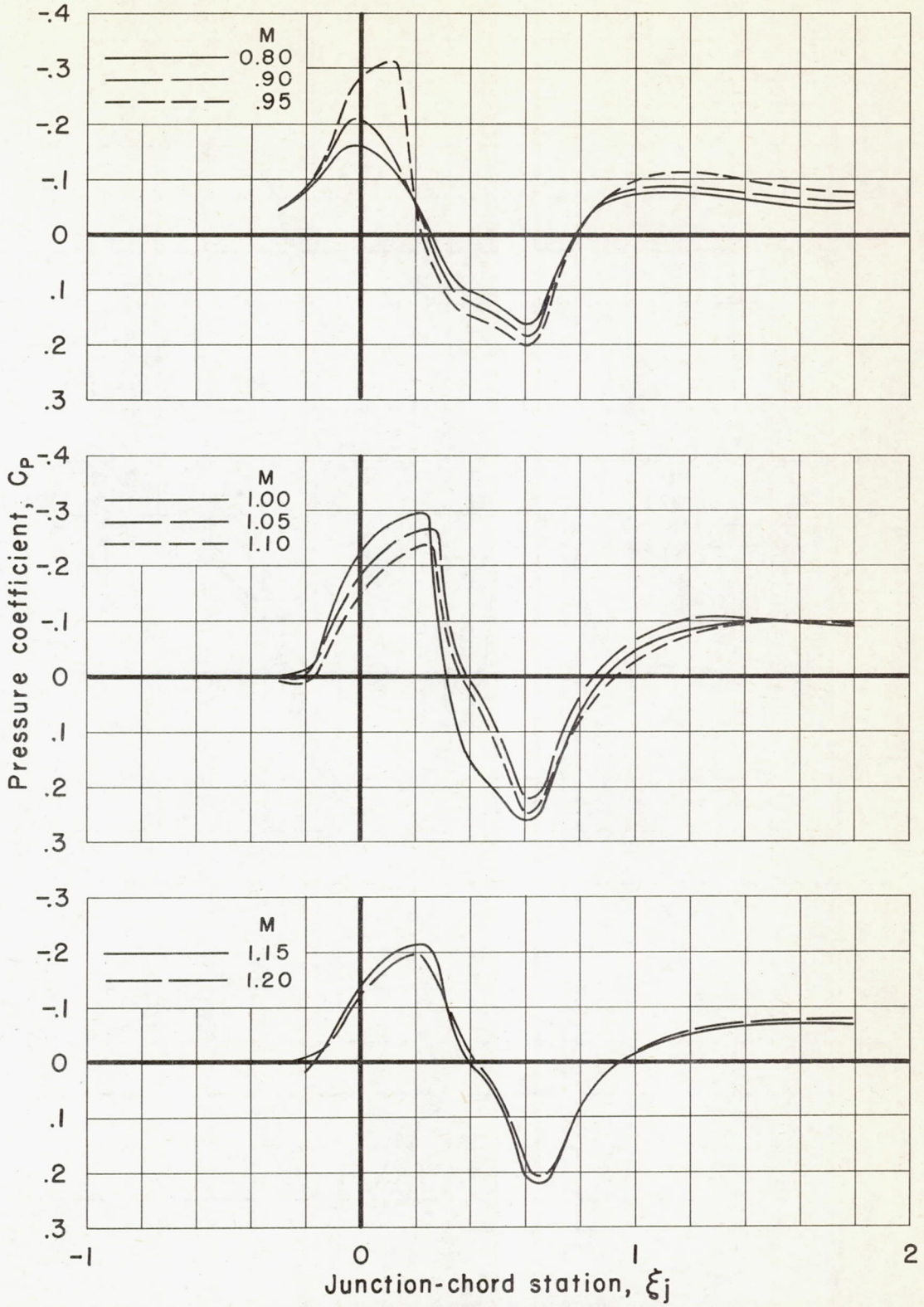

Figure 34.- Experimental pressures for body III-B at zero lift.

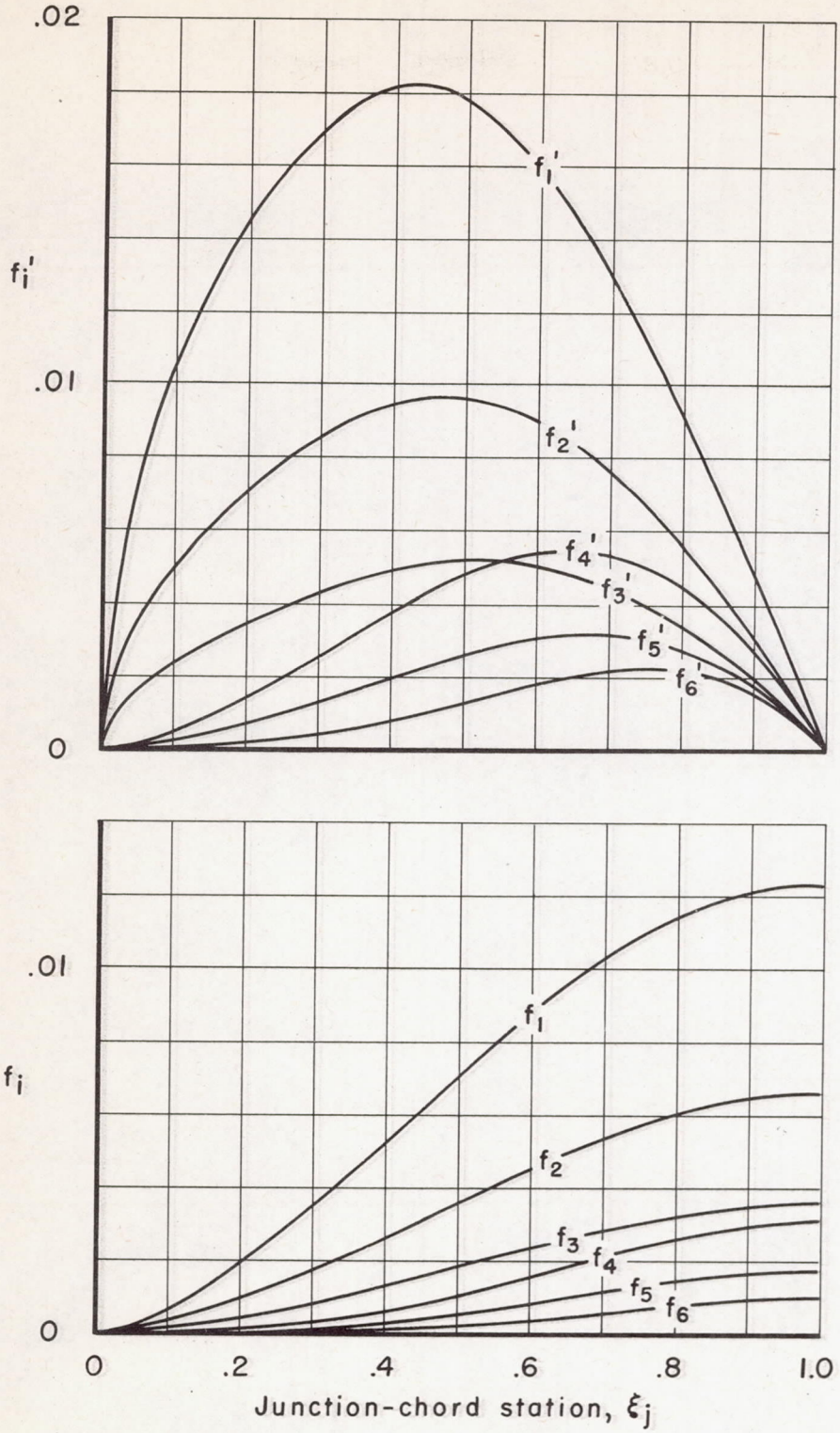

Figure 35.- The f_i' and f_i functions (eqs. A6 and A7) for the wing of model series II.